Metals and Ceramics Division

Heavy Vehicle Propulsion Materials Program
Quarterly Progress Report for
July through September 2002

D. R. Johnson
Technical Project Manager

Prepared for
U.S. Department of Energy
Assistant Secretary for Energy Efficiency and Renewable Energy
Office of FreedomCAR and Vehicle Technologies Program
EE 07 01 00 0

Prepared by the
OAK RIDGE NATIONAL LABORATORY
Oak Ridge, Tennessee 37831-6066
Managed by
UT-Battelle, LLC
for the Department of Energy
Under contract DE-AC05-00OR22725

CONTENTS

Cost Effective High Performance Materials and Processing

Advanced Cast Austenitic Stainless Steels For High Temperature Components (ORNL and Caterpillar, Inc.)

Development of NOx Sensors for Heavy Vehicle Applications (ORNL, Ford Motor Company, and Visteon Automotive Systems)

Cost-Effective Smart Materials for Diesel Engine Applications (ORNL)

Low-Cost Manufacturing Processes for Ceramic and Cermet Diesel Engine Components (SIU-C)

Low Cost –High Toughness Ceramics (ORNL)

Synthesis of Powders for Titanium Carbide/Nickel Aluminide Cermets (University of Colorado)

Advanced Manufacturing Technology

Intermetallic-Bonded Cermets (ORNL)

Low-Cost Manufacturing of Precision Diesel Engine Components (ORNL)

Cylindrical Wire Electrical Discharge Machining (EDM) and Temperature Measurement (North Carolina State University)

Testing and Characterization

NDE/C Technology for Heavy Duty Diesel Engines: Fuel Delivery and Insulating Materials (Argonne National Laboratory)

NDE Development for Ceramic Valves for Diesel Engines (Argonne National Laboratory)

Processing and Characterization of Structural and Functional Materials for Heavy Vehicle Applications (North Carolina A&T State University)

Life Prediction of Diesel Engine Components (ORNL)

Durability of Diesel Engine Component Materials (ORNL)

Laser Surface Texturing of Lubricated Ceramic Parts (ORNL)

Materials and Testing Standards

Implementing Agreement for a Programme of Research and Development on Advanced Materials for Transportation Applications (ORNL)

Standards for Reliability Testing of Heavy Vehicle Propulsion Materials (NIST)

Mechanical Property Test Development (NIST)

Advanced Cast Austenitic Stainless Steels For High Temperature Components

P.J. Maziasz and R.W. Swindeman
Oak Ridge National Laboratory
and
M.J Pollard
Caterpillar, Inc.

Objective/Scope

The objective of this new CRADA project is to commercially scale up the new modified cast austenitic stainless steels developed by Caterpillar and ORNL as cost-effective high-performance alternatives to SiMo ductile cast iron. SiMo cast iron is the standard material for most diesel engine exhaust manifold and turbocharger housing components. Cast austenitic stainless steels like CN12 can withstand prolonged exposure at temperatures of 750°C or above and are much stronger than SiMo cast iron above 550-600°C. The new modified CN12 and modified CF8C steels have better aging resistance and ductility after creep, which suggests they would have better fatigue and thermal fatigue resistance and be better able to survive the severe thermal cycling that exhaust components experience without developing cracks. This project will provide the more comprehensive properties data need by designers to qualify the alloys and design optimized components for trial component production. This new advanced diesel engine CRADA (Cooperative Research and Development Agreement) project (ORNL02-0658) began July 21,2002 and last at least three years. More detailed information on this project must be requested directly from Caterpillar, Inc.

Technical Highlights, 4th Quarter, FY2002

Background

Advanced large diesel engine must have higher fuel efficiency as well as reduced exhaust emissions, without sacrificing durability and reliability. Therefore, exhaust manifold and turbocharger housing materials must withstand temperatures ranging from 70 to 750°C or higher in a normal duty cycle that includes prolonged, steady high-temperature exposure as well as more rapid and severe thermal cycling. New technology to reduce emissions and heavier duty cycles will push temperatures in these critical components even higher. Current exhaust components are made from SiMo ductile cast iron, and higher engine temperatures would push such materials well beyond their current strength and corrosion limits. The previous CRADA produced systematic data comparing cast CN12 stainless steel and SiMo cast iron for such diesel exhaust component applications. The data demonstrated a clear tensile strength advantage of standard CN12 steel above 550-600°C, and even larger advantages in creep strength and fatigue life above 700°C. Furthermore the previous CRADA project developed new modified CN12 and modified CF8C steels with better creep strength, and significantly better aging resistance and thermal fatigue resistance than standard CN12. The purpose of this new CRADA project is to commercially scale up the new modified stainless steel heats, develop the systematic and thorough data base required by designers to qualify the new alloys and design optimized components for trial component production.

Approach

Prior work on lab-scale (15 lb induction melts with argon cover gas) heats of modified CN12 and modified CF8C and screening tests (aging, tensile, creep) at 800-850°C at ORNL provided a composition of each alloy for commercial scale up. The modified CN12 had been shown to be stronger in creep at 850oC and have more tensile ductility at room temperature after aging than the standard CN12 steel. Ongoing creep tests at 850°C and 35 MPa show that the modified CF8C (over 22,000 h) has similar or better rupture strength than standard CN12 (over 12,000 h) steel. Preliminary high-temperature fatigue testing at Caterpillar Technical Center suggested at significant advantage of the modified CN12 steel. Two commercial stainless steel foundaries were chosen, and they produced 500 lb heats of the modified CN12 and modified CF8C steels for testing and evaluation.

Technical Progress

Both commercial stainless steel casters found the compositions of the modified stainless steels well within the range of austenitic stainless steels they could produce by standard commercial practice. The compositions of the steels were within the ranges specified, and fluidity trials were performed prior to casting kiel blocks for mechanical properties specimens and trials of some simple existing component geometries. Both modified steels exhibited good melting and pouring behavior for both vendors, as good as or better than standard CN12 or CF8C steels. Kiels were delivered to Caterpillar and creep/tensile and fatigue specimens were machined from as-cast material with no heat treatment. Tensile and fatigue testing began this quarter and results will be reported next quarter. Thermal fatigue testing began at Caterpillar, and aging and microstructural analysis will be done at ORNL next quarter.

Communications/Visits/Travel

Team communications between ORNL and Caterpillar occur in detail as needed, at least once every week or two. The new 3-year CRADA began on July 21, 2002, and previous CRADA was ended.

An invention disclosure and patent application on cast austenitic stainless alloys with improved performance were completed by Caterpillar and filed with the U.S. Patent Office in December 2000. It is entitled "Heat and Corrosion Resistant Cast Stainless Steels With Improved High Temperature Strength and Ductility," by P.J. Maziasz (ORNL), T. McGreevy (U. of Bradley/CAT), M.J. Pollard (CAT), C.W. Siebenaler (CAT), and R.W. Swindeman (ORNL). Prior to the conclusion of the previous CRADA, the patent application was modified and split into two separate inventions, one on the modified CF8C steel and the other on the modified CN12 steel.

Status of Milestones

Formal milestones were imbedded in the previous CRADA and in the new CRADA, which is part of the DOE/OFCVT Heavy Vehicle Propulsion Materials Program, but a task in the ORNL FWP. However, all milestones were achieved on or significantly ahead of schedule.

Publications

There have been several detailed internal reports on this project written at the Caterpillar Technical Center.

A final ORNL report on the previous CRADA was prepared this quarter, and it is awaiting final approval from Caterpillar for unrestricted release.

Development of NOx Sensors for Heavy Vehicle Applications

Timothy R. Armstrong
Oak Ridge National Laboratory

CRADA No. ORNL 01-0627
with Ford Motor Company

Objective

The proposed project seeks to develop technologies and materials that will facilitate the development of NO_x and ammonia sensors. The development of low-cost, simple NO_x will facilitate the development of ultra-low NO_x emission engines, directly supporting the OHVT goals.

Technical Highlights

1. We have initiated construction on two electrode test stands to screen a large number of potential NO sensitive materials. The test stand is composed of a high-temperature furnace, a gas mixing panel to mix CO, CO2, NO, NO_2, SO_2 and hydrcarbons, a chemiluminescence sensor to determine NO and NO_2 concentrations, and a meter to measure the EMF generated.
2. The test stands have been delivered. We are currently awaiting delivery of the chemiluminescence NO_x sensor and the humidity sensor.
3. Dr. David West has joined our staff as a post-doctoral researcher. Dr. West joins us after completing his Ph.D. at the University of Illinois and will be the lead research developing electrode materials for NO_x sensors.

Status of Milestones

Although this project had a late kick-off, we are ahead of schedule of most of the milestones:

1. Modify current sensor test stand for operation at 800°C (delayed at request of Ford)
2. Test NGK sensor in modified test stand (delayed at request of Ford)
3. Deliver NO_x catalyst assessment and program plan to Ford (completed 6/2002)
4. Construct NO_x electrode test stand. (Two stands to be completed by November, delayed due to delivery of components 2002)
5. Deliver report on initial rest results (To be completed by November 2002)
6. Design and procure screens for simplified NO_x sensor design (to be completed October 2002)
7. Produce first simplified NOx sensors for testing (delayed until December 2002).

Communications/Visits/Travel

Conference call held with Ford in September.

Problems Encountered

None to date.

Publications

None to date.

Cost-Effective Smart Materials for Diesel Engine Applications

J. O. Kiggans, Jr., F. C. Montgomery, T. N. Tiegs, and B. M. Evans
Oak Ridge National Laboratory

Objective / Scope

There are two objectives for this project. The first is to evaluate the cost-effectiveness and maturity of various "Smart Materials Technologies," which are under consideration for diesel engine applications, such as fuel injection systems. The second is to develop "Smart Materials" to be incorporated into working actuators and sensors.

Task 1 - Multilayer Electroded Laminates

The purpose of this study is to find satisfactory methods for the preparation of PZT laminates with internal electrodes from tape cast materials. There is no new data on this task to include in the present report.

Task 2 – Compositional Alteration of PZT-4

A major task of this project is to develop cost-effective PZT compositions and processing methods that will give PZT powders that will sinter to high density at a temperature below 960 ºC. This goal is driven by the need to lower the cost of multilayer PZT actuators by reducing the cost of the interlayer electrodes. Commercial hard PZT powders require sintering at temperatures exceeding 1200 ºC and, thus, multilayer devices must use costly Pd/Ag electrodes.

In progress reports published this year we provided data which shows that small additions of bismuth oxide can lower the PZT sintering temperature sufficiently that Ag or Ag/Pd alloy (70/30) can be used as internal electrodes. Furthermore, we established that the procedure used to blend the PZT powder with the sintering aids greatly influences the sinterability of die pressed disks. We found that attrition milling PZT-840 powder containing a sintering aid consisting of 2 wt.% Bi_2O_3 and an acceptor ion oxide resulted in a powder that sintered to greater than 99 % of the theoretical density after 1 hr at 900 ºC. The sintered PZT had piezoelectric properties which were as good as the piezoelectric properties of commercial PZT sintered at ~1275 ^{o}C and, because of the acceptor ion, the electromechanical Q was significantly higher than that of either the undoped powder or commercially sintered PZT-840.

In the 2002 Heavy Vehicle Annual Operating Plan we proposed to investigate the possibility of strengthening and toughening PZT ceramics by the addition of glass forming additives. This goal is important because piezoelectric ceramics based on PZT have poor mechanical properties that could cause actuators with a PZT element to have low reliability. During FY2002 we conducted a study determining the effects of adding a small amount of silicon carbide (SiC), boron nitride (BN), Alumina (Al_2O_3) or alumina coated with 5 wt.% Pt on the physical and piezoelectric properties of PZT-840 containing the Bi_2O_3 sintering aid.

Experimental

Two batches of attrition-milled powder were prepared. The first was commercial PZT-840 containing 2 wt.% of the sintering aid and the second batch contained 3 wt.% sintering aid. Both were prepared in the same way except that in the first batch 1.5 wt.% of both polyvinylpyrrolidone (PVP) and Carbowax 8000 was added to the mixture as a binder and lubricant for compacting.

The procedure used for the first batch is typical and is described here. Into a polybottle was placed ethanol (92g), PVP (3 g), Carbowax 8000 (3 g) and 2 g of a 50/50 (v/v) mixture of Menhedan fish oil (Mistler) in ethanol. The bottle was shaken to dissolve the solid components. To this solution was added PZT-840 (196 g) as well as Bi_2O_3 and an acceptor-ion oxide. This was mixed by shaking and then poured into the grinding tank of an Szegvari attrition mill. To reduce the possibility of contamination the grinding tank was polyethylene and the agitator arms were polyurethane coated. The powders were milled for 6 hr with 3 mm spherical ZrO_2 media using a 5:1 weight ratio of media to PZT-840 powder.

After homogenizing, the slurry were separated from the media and dried at 80 ^oC. The powder cake was crushed and the powder was sieved through a No.100 U.S.A. standard testing sieve (Tyler equivalent 100 mesh).

SiC (B 20 grade, Starck), BN (HCP grade, Advanced Ceramics Corp), Al_2O_3 (Dispal 23N4-80 boehmite, Sasol Chemical Industries) were used as the second phases. The Beta SiC has an average particle size of <0.6 μm and a BET surface area of 20-23 m^2/g. The BN has a typical surface area of 15 m^2/g and is reported to have a particle size distribution that will pass a minimum of 94.5% through a 325 mesh (44 μm) screen . The Dispal is a dispersible boehmite alumina that has a dispersed particle size of 100 nm. The attrition milled PZT powders and 0.5 vol.% of the second phase powders were wet milled for 24 hr in high-density polyethylene containers with ethanol using 10 mm spherical ZrO_2 balls and a media to PZT weight ratio of 12:1. Since the base PZT powder containing 3 wt.% of the sintering aids did not contain any binder, 1.5 wt.% PVP and Carbowax 8000 were added during the wet ball milling process. The milled slurries were air dried and the powder cake was crushed and sieved similar to the attrition-milled powders.

Disks ~1.2 mm thick by 28.7 mm diameter were obtained by cold compaction of the powers in a steel die at 103 MPa. The organic binders were removed by heating in air to 625 ^oC at 1 ^oC/min. with a 1 hr hold at 325 ^oC and a 2 hr hold at 600 ^oC. Dimensional and weight measurements showed that the samples after binder removal were between 56% and 60% of the theoretical density based on the reported value of 7.6 g/cm^3 for PZT-840.

Sintering was carried out in a conventional tube furnace fitted with an alumina tube and $MoSi_2$ heating elements. The disks were sintered in closed alumina crucibles on a platinum setter with a mixture containing 10 wt.% ZrO_2 and 90 wt.% $PbZrO_3$ added to control the PbO vapor pressure above the samples. The sintering profile included a 3 hr hold at either 900 or 950 °C with a 15 °C /min heating and cooling rate. After sintering, the density was measured using the Archimedes method by immersion in ethyl alcohol.

To measure the piezoelectric properties, Ag paste (Metech 3288) was screen printed on both sides of the sintered disks and the electrodes were cured at 600 °C for 10 minutes. The disks were poled at 1.5 to 2.0 kV/mm for 10 minutes in a silicone oil bath at 120 °C. The piezoelectric properties were measured at room temperature after a 24 hr stabilization period. Capacitances were measured at 1 kHz and the resonant frequencies of the radial mode were measured using an impedance gain phase analyzer (Agilent 4194A).

The flexural strength was measured using the monotonic equibiaxial method.[1] The flexural strength was determined after measuring the piezoelectric properties so the specimens were tested with the Ag electrodes on opposing faces. Because the sample faces were not machined, a compliant rubber layer was placed between the support ring and the specimen to reduce misalignment and contract stresses. Adhesive Teflon tape was placed on the compressive face and, to reduce friction, a strip of Teflon thread tape was placed between the adhesive tape and the load ring.

Hardness was measured by indentation with a Vickers diamond indenter on samples mounted in an epoxy holder and polished on a Struers RotoPol-22 grinding system fitted with a RotoForce-4 sample holder.

The toughness was calculated from the lengths of the cracks originating at the corners of the indent using the formula proposed by Evans.[2] The error in the toughness was estimated from the variation in the crack lengths measured on several indents in each sample.

Results and Discussion

The presence of the second phase additive reduced the density of the sintered samples. Without any second phase additive the samples with 2-wt.% sintering aid reached a density slightly greater than 7.6 g/cm^3 after 3 hr at 900 °C and sintering at 950 °C did not increase the density. Increasing the sintering aid to 3-wt.% resulted in a small decrease but the density remained above the reported value of 7.6 g/cm^3. As shown in Figure 1, incorporating 0.5 vol.% of the second phase additives reduced the density significantly. The density was lowered by about the same amount for additions of BN, Al_2O_3 and Al_2O_3 coated with 5 wt.% Pt but adding SiC reduced the sintering ability to a larger extent. By increasing the amount of sintering aid from 2 to 3 wt.%, the density of the samples doped with SiC and with BN increased but there was no effect on the samples doped with Al_2O_3. SEM analysis of the samples shows that the samples with the second phase additives have trapped porosity. The immersion density data indicates that this is closed porosity for the samples sintered to greater than ≈7.2 g/cm^3 (93 % T.D), but is open porosity for lower density samples.

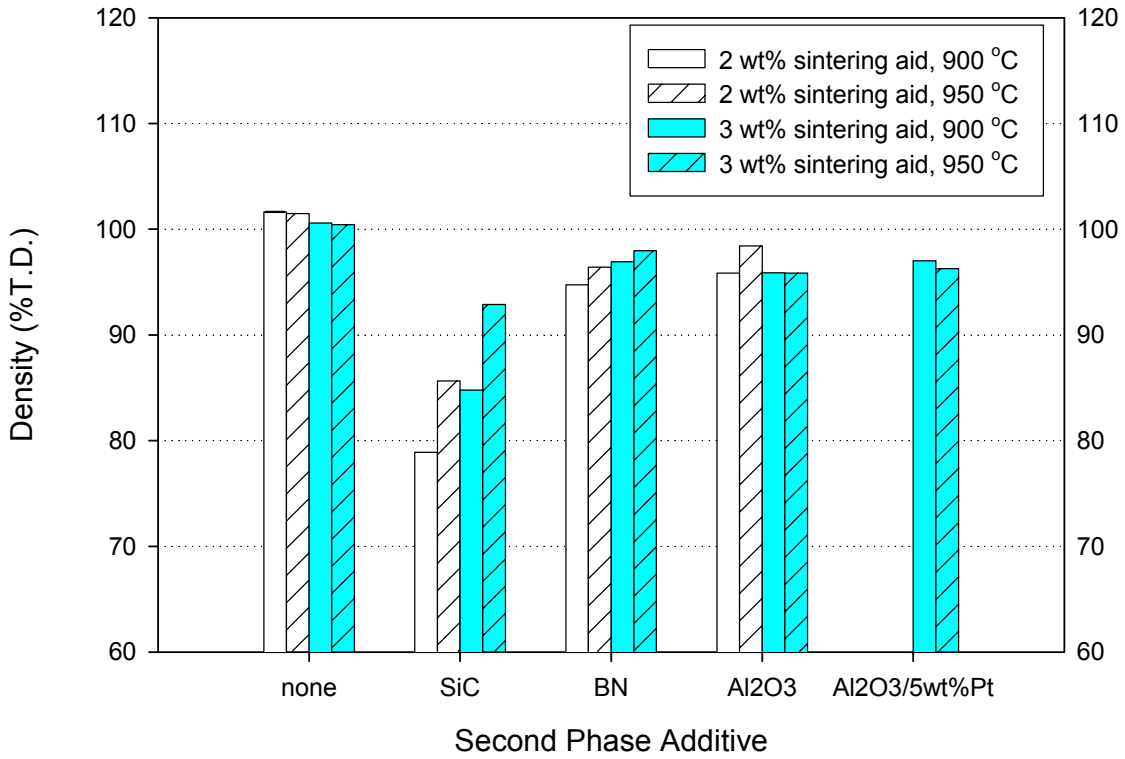

Figure 1. Density of PZT-840 Doped with Bi_2O_3 Sintering Aid and Second Phase additives Sintered at 900 and 950 °C.

The flexural strength of the samples was measured using the equibiaxial method. We conducted a cursory test to determine if the presence of the Ag electrodes would have a significant effect on the strength, and if the samples needed to be machined before testing. The results are shown in Table 1. There is no statistically significant difference between the flexural strength of

Table 1. Density of PZT-840 Doped with Bi2O3 Sintering Aid and Second Phase additives Sintered at 900 and 950 °C.

Specimen	Sintering Conditions		Surface Conditions	Flexural Strength (MPa)
	Temp (°C)	Time (hr)		
245-C	900	3	Ground & polished	67
245-B	900	3	As sintered	65
250-C	852	3	Ground & polished	72
250-B	852	3	As sintered	60
Commercial Product			No electrodes	92 ± 6.7
Commercial Product			Poled, Ag electrodes	111 ± 25.3

commercial disks that are poled and have Ag electrodes on the parallel faces and unpoled disks without electrodes. There also isn't any difference between the flexural strength of samples that had the surface layer removed and samples that were tested in the as-sintered condition.

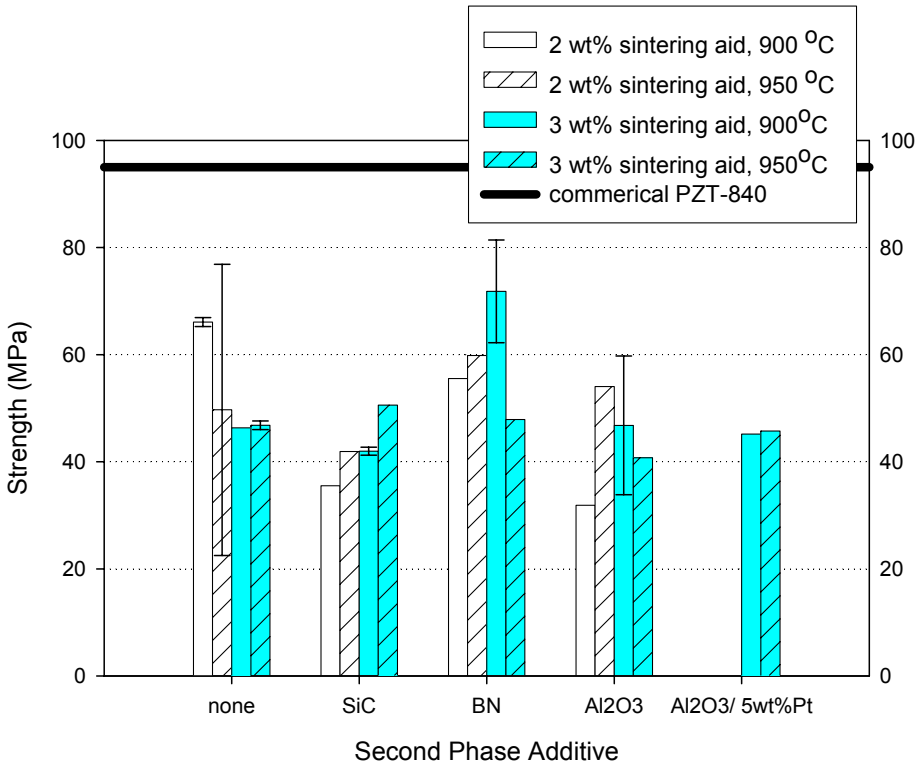

Figure 2. Flexural Strength of PZT-840 Doped with Bi_2O_3 Sintering Aid and Second Phase Additives sintered at 900 and 950 °C.

Figure 2 compares the flexural strength of sintered PZT-840 containing 2 and 3 wt.% of the sintering aid with that of commercially supplied PZT-840 disks and with that of samples containing the second phase additive. The specimens were sintered at 900 and 950 °C for 3 hr. In this figure, bars with the standard deviation error indicated are duplicate measurements and those without error are only single determinations. When compared to the commercial PZT-840, the flexural strength is reduced by about 30% when 2 wt.% of the sintering aid is added and by 50 % when the amount of sintering aid is increased to 3 wt.%. Because of the small number of samples tested, it is difficult to generalize. But, it does appear that samples sintered with BN as the second phase additive are somewhat stronger than those prepared with the same vol.% SiC or Al_2O_3. It is apparent that none of these second phase additives increase the strength of the samples containing the Bi_2O_3 sintering aid up to the value for commercial PZT. This is in contrast to other attempts on PZT strengthening. Tajima[3] found that 0.5 vol.% of nanophase alumina increased the strength of $Pb(Zr_{0.52}Ti_{0.48})O_3$ from 60 MPa to 115 MPa. Li[4] found that the addition of 0.3 wt.% of an alumina whisker containing $9Al_2O_3{\cdot}2B_2O_3$ increased the strength from 68 MPa to about 100 MPa. The average failure stresses are increased approximately 35% by the addition of 0.5 wt.% SiC whiskers compared to those of pure Pb(Zr,Ti)O3 ceramics[5]

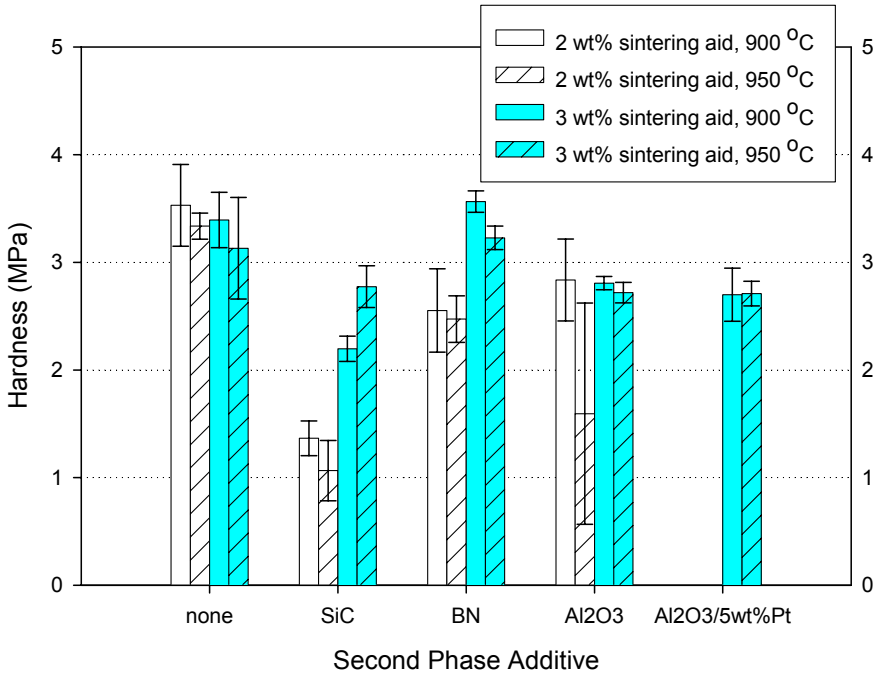

Figure 3. Vickers Hardness of PZT-840 Doped with Bi_2O_3 Sintering Aid and Second Phase Additives sintered at 900 and 950 °C.

The Vickers hardness was measured using both a 5 kg and a 10 kg load. Shown in Figure 3 is the hardness for the samples with the second phase additives. Since there was no difference in hardness between the 5 kg and the 10 kg indent, the average value for all the indents on each specimen is plotted along with the standard deviation. Each of the second phase additives reduces the hardness, particularly for the samples containing 2 wt.% of the sintering aid. Tajima, found that the hardness of his composites improved by addition of at least 0.1 vol.% second phase. His composite containing 0.5 vol.% Al_2O_3 had a hardness value of 3.9, which is higher than that of our samples. The lower values for the hardness in our samples probably reflect the increased internal porosity and lower density.

PZT ceramics have low fracture toughness that varies slightly with the type of PZT and with the specific preparation and sintering condition. Tajima reports a K_{IC} value of 1.5 MPa-m$^{-0.5}$ for his base PZT and that the addition of an Al_2O_3 second phase reduces this value to 1.3 to 1.4. Yang[6] reports a value of 1.1 and shows that the addition of bismuth titanate can increase K_{IC} to greater than 2.0. Hwang[7] has studied the addition of Pt nanoparticles and reports that K_{IC} increases from 1.4 for his undoped PZT to 1.8 for the composite containing 1 vol.% Pt. Our PZT-840 doped with the sintering aids has a K_{IC} of 1.2 to 1.4. Adding Al_2O_3 does not affect K_{IC}, but adding SiC or BN increases K_{IC} but by only about 20% in most of the samples tested (Figure 4).

One difficulty with attempting to strengthen and toughen PZT ceramics by the addition of metal particles or metal oxides is the harmful influence of the secondary phase on the piezoelectric properties of the composite. This arises because PbO is a good flux and can dissolve many oxides therein changing the PZT composition. In fact, we have exploited this behavior to increase the sintering rate by using Bi_2O_3 that is incorporated into A-sites in the PZT lattice and

an acceptor ion oxide that is incorporated in a B-site. We selected our second phase additives based on literature which showed that these phases have been used to strengthen other ceramic composites, and that they may not react as readily with PbO at the low sintering temperatures required for densification of our compositions.

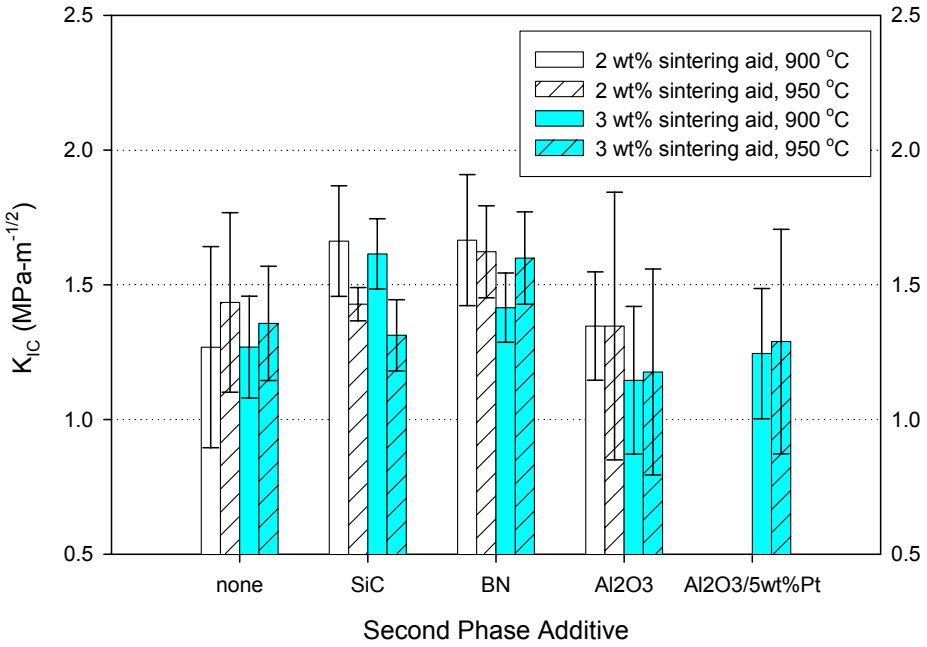

Figure 4. Fracture Toughness of PZT-840 Doped with Bi_2O_3 Sintering Aid and Second Phase Additives sintered at 900 and 950 °C.

Shown in Figure 5, Figure 6 and Figure 7 are the piezoelectric properties d_{33}, radial coupling coefficient (k_r), and mechanical Q (Q_m), respectively, for the PZT-840 with sintering aid and with the second phase additives. PZT-840 containing 2 wt.% of the Bi_2O_3 mixture sintered at 900 to 950 °C has the same d_{33} and k_r as commercially sintered PZT-840, but exhibits a much larger Q_m. The larger Q is a result of the acceptor ion incorporated into the sintering aid. Increasing the amount of the Bi_2O_3 mixture to 3 wt.% reduces both d_{33} and k_r but increases Q_m. The second phase additives SiC and BN reduces the piezoelectric properties particularly when sintered at 900 °C. Increasing the sintering temperature with these additives results in better properties. Since the number of piezoelectric layers required to produce a specific displacement is inversely related to the d_{33}, our goal is to keep the d_{33} around 0.3×10^{-9} m/V. It is apparent from Figure 5 that sintering the SiC and BN doped material at 900 °C will not satisfy this goal. The addition of Al_2O_3 as the second phase does not reduce d_{33} when sintered at either 900 or 950 °C. Tajima found that 0.5 vol.% Al_2O_3 reduces the coupling coefficient for his PZT composition from 0.41 to 0.12. Although adding Al2O3 to our material reduces the coupling constant, the effect is not as large as found by Tajima.

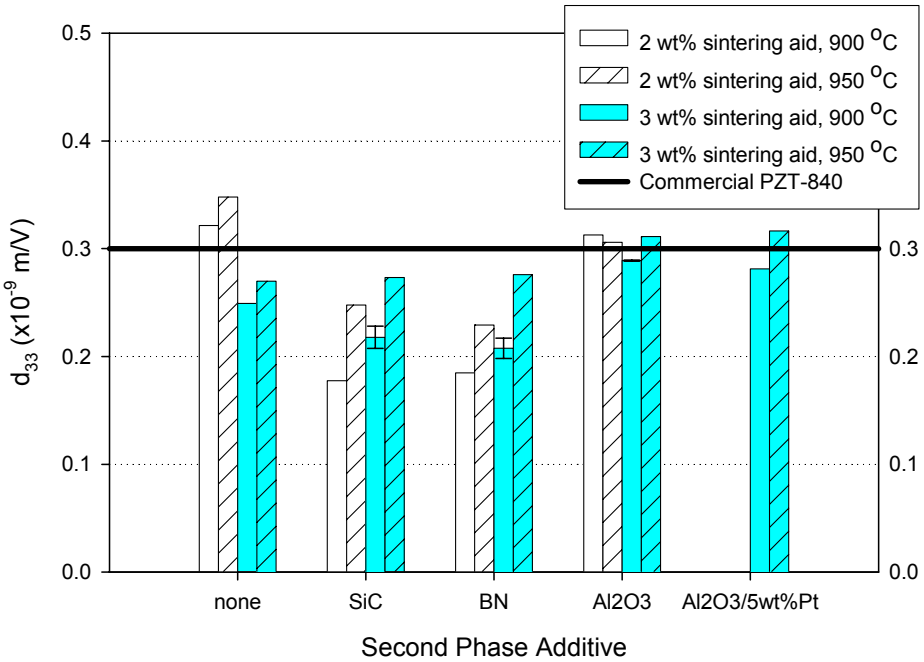

Figure 5. Piezoelectric Constant d_{33} of PZT-840 Doped with Bi_2O_3 Sintering Aid and Second Phase Additives Sintered at 900 and 950 °C.

In order to try to understand these results, we examined the fracture surfaces and the microstructure of the sintered bodies with SEM. Images of the typical fracture surfaces are given in Figure 8. The fracture for the base PZT and for PZT doped with SiC or with Al_2O_3 is completely intergranular occurring along grain boundaries. However, as shown in Figure 8c, the fracture of the BN doped PZT results in cleavage of the larger grains as well as cleavage along grain boundaries. The strength of the BN doped PZT was higher than that of the other compositions due to this small amount of intragranular fracture in this material.

The morphology of the fracture surface for the SiC doped PZT sintered at 900 °C for 2 hr is shown in Figure 8b. The grains are not well defined and the edges are rounded unlike the grain edges in the other samples. EDAX analysis of the fracture surface shows that the surface is covered with a phase that is rich in Si. When the SiC doped PZT is sintered at 950 °C, the grains in the fracture surface are more distinct but the amount of Si rich phase on the surface is similar.

A detailed EDAX examination of the fracture surfaces and of polished surfaces did not detect any of elements that would indicate any second phases. EDAX showed that the composition of the grains and of the grain boundaries is not homogeneous since the ratio of the Pb to that of both O and Ti varied within the samples. SEM observations also did not provide any visual evidence for second phase inclusions.

The effect of the second phase additives on the grain size (Figure 9) of the PZT is complicated. The base PZT has a grain size of about 1.5 μm that does not depend on the temperature or

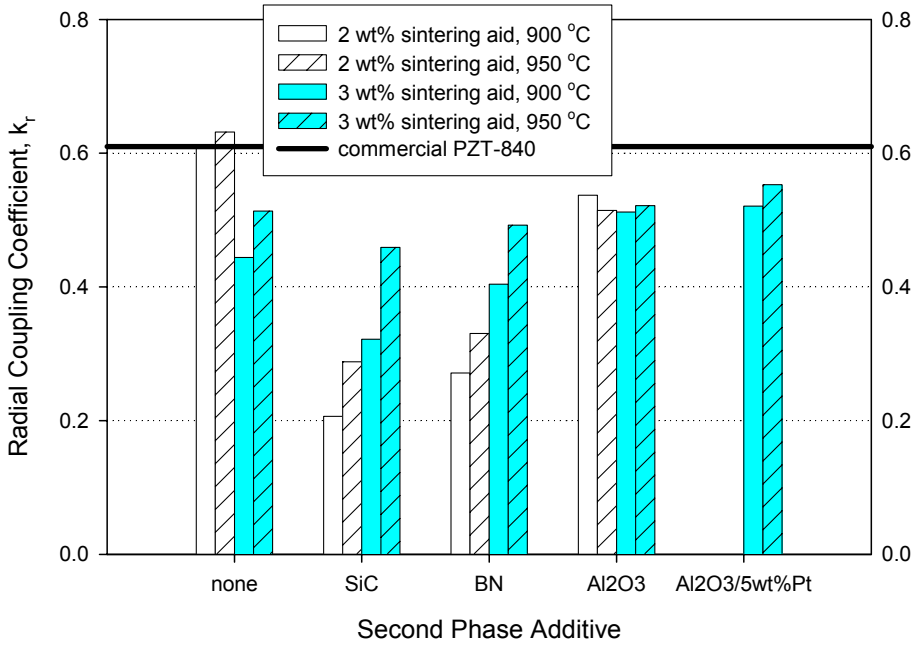

Figure 6. Radial Coupling Coefficient of PZT-840 Doped with Bi_2O_3 Sintering Aid and Second Phase Additives Sintered at 900 and 950 °C.

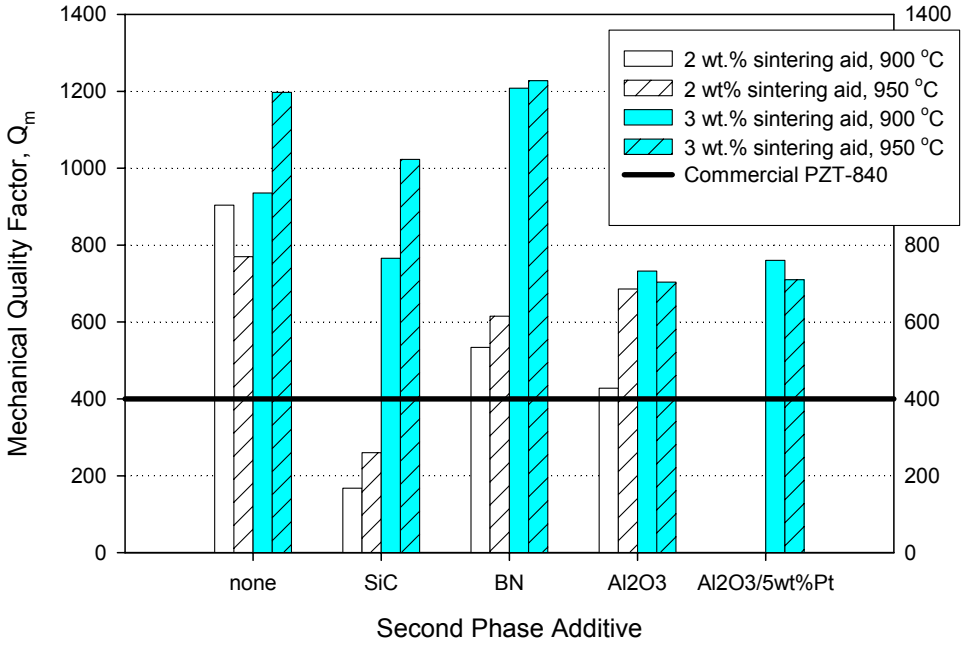

Figure 7. Radial Coupling Coefficient of PZT-840 Doped with Bi_2O_3 Sintering Aid and Second Phase Additives Sintered at 900 and 950 °C.

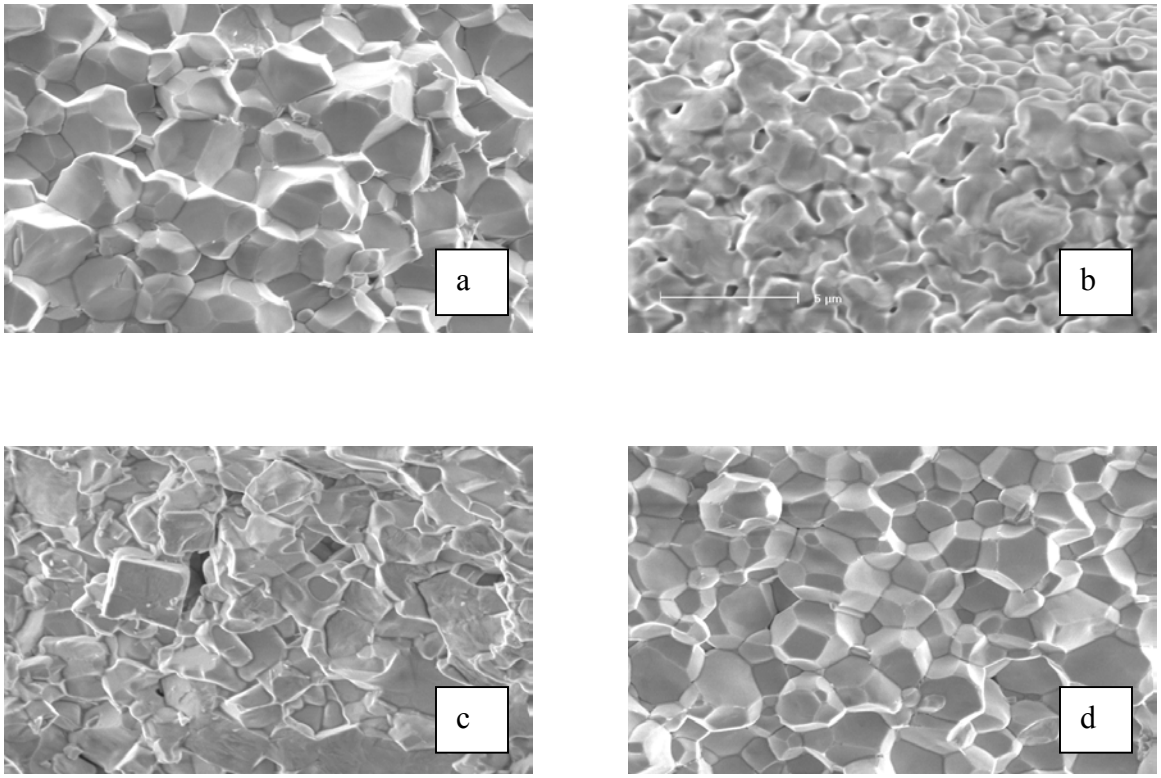

Figure 8. Fracture Surface (5000x) of PZT-840 Sintered for 3 hr at 900 °C Containing 2 wt.% Sintering Aid and a Second Phase Additive (a) none (b) SiC (c) BN and (d) Al_2O_3.

the amount of sintering aid. Addition of SiC lowers the grain size significantly at 900 °C to less than 1μm but has little effect at 950 °C. Though adding BN has no effect on the grain size at 900°C, sintering at 950°C increases the grain size to greater than 2 μm. The addition of nanophase Al_2O_3 to the PZT doped with 2 wt.% sintering aid results in slightly smaller grains that are independent of temperature. Increasing the amount of sintering aid to 3 wt.% while holding the amount of nanophase Al_2O_3 constant does not affect the grain size at 900 °C but at 950 °C the grain size increases to greater than 2 μm. The literature concerning the effect that Al_2O_3 has on the grain size in PZT is contradictory. Tajima has reported that the grain size is both reduced[3] or increased[8] with increasing Al_2O_3 content in PZT/ Al_2O_3 composites. The difference is probably related to the interaction of the Al_2O_3 with additives in the PZT to form a glassy phase that can increase diffusion and grain growth. With our composition, the viscosity of the glass formed by the sintering aid must depend on the concentration of nanophase Al_2O_3 because 2 wt.% sintering aid results in warped samples while flat samples are obtained when 3 wt.% sintering aid is used.

Trivalent Al is soluble in PZT to 1.7 at.%.[9] It is well established that Al^{3+} enters the perovskite structure at a B-site.[10] We added 0.5 vol.% Al_2O_3 which is 1.6 at.% Al^{3+}, so the Al^{3+} was

probably incorporated into the octahedral sites. Al^{3+} substituting at these sites should act as an acceptor ion since it replaces a tetravalent Zr or Ti. However the observed decrease in Q_m

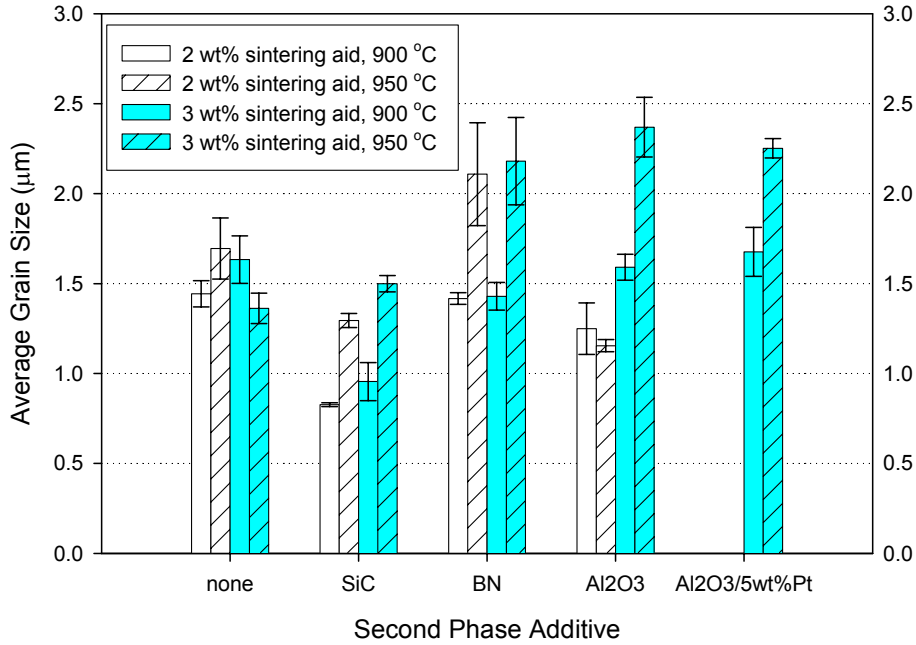

Figure 9. Grain Size of PZT-840 Doped with Bi_2O_3 Sintering Aid and Second Phase Additives Sintered at 900 and 950 °C.

and the increase in d_{33} are contrary to typical effects caused by acceptor ion substitution and is evidence that the Al_2O_3 may be altering the chemistry within the sintering aid.

References:

[1] Standard Test Method for Monotonic Equibiaxial Flexural Strength of Advanced Ceramics at Ambient Temperature, ASTM C 1499-01, American Society for Testing and Materials.

[2] Evans, A. G., Fracture Mechanics Applied to Brittle Materials, ASTM STP 678, S. W. Freiman, Ed., American Society for Testing and Materials, 1979, pp 112-135.

[3] Tajima, K., H. J. Hwang, M. Sando and K. Niihara, J. of the European Ceramic Society, **19** (1999), 1179-1182.

[4] Li Xiaohui, Lin Shengwei, Qu Cuifeng, Yao Chunhua and Jin Qihua, Integrated Ferroelectrics, **13** (1996), 71-77.

[5] Yamamoto, T.; Igarashi, H.; Okazaki, K., Ferroelectrics, **63** (1985), 281-8.

[6] Yang, Jin Si, Xiang Ming Chen, Tatstuhiko Aizawa, and Makoto Kuwabara, Solid State Ionics, **108** (1998), 117-121.

[7] Hwang, Hae Jin, Ken-ichi Tajima, Mutsuo Sando, Motohiro Toriyama and Koichi Niihara, J. of the Ceramic Society of Japan, **108** (2000), 339-344.

[8] Tajima, K., H. J. Hwang, and M. Sando, J. of the American Ceramic Society, **83** (2000), 651-653.

[9] Atkin, R. B. and R. M. Fulrath, J. of the American Ceramic Society, **53** (1970), 51-52.

[10] Jaffe, B., Cook, W. R.,and H. Jaffe, Piezoelectric Ceramics; pp. 158-60, Academic Press, London, U.K. 1971

Task 3 – Paper study "-Diesel Fuel Injection Technology and Piezoelectric Actuator Status

Diesel Fuel Injection Systems

The need for precise control of fuel injection parameters is driven by the idea that the primary system for controlling the operation of the diesel engine is the fuel injection system. Power in the diesel engine is controlled by modulating the fuel rate, as opposed to modulating the air intake, as in a gasoline engine. In the diesel cycle, air is compressed to high pressures then fuel is injected into the compressed air. As the air is compressed, it's temperature increases due to the ideal gas law. The atomized fuel injected into the cylinder evaporates and rapidly reaches its auto-ignition temperature completing the combustion process. Varying the rate and shape of the injection cycle or even using multiple injections can be used to control power, emissions, and fuel economy. Since there are no spark plugs and spark timing in the diesel engine, the combustion process is controlled by manipulating the injected fuel quantity, timing, rate, and pressure.

Unlike spark-ignited engines, the diesel fuel injection systems must deliver fuel at extremely high pressures. The fuel injection systems on most gasoline-powered cars deliver the fuel to the intake manifold just before the intake valve. Most diesel engines use a direct-injection (DI) method in which the fuel is injected directly into the cylinder. The combustion chamber in most DI engines is comprised of a "bowl" in the crown of the piston.[1]

The main primary functions of the fuel injection system are injection metering and injection timing. Another function of the fuel injector is "atomization" or delivery of the fuel in such a way that it easily mixes with the air in the chamber and penetrates the compressed air in the combustion chamber.[2]

Primary Functions of Diesel fuel injection system:

- Injection Timing Control
- Atomization and Penetration
- Injection Metering

Additional Functions of Diesel Fuel Injection System:

♦ Rate Shaping
♦ Multiple Injections

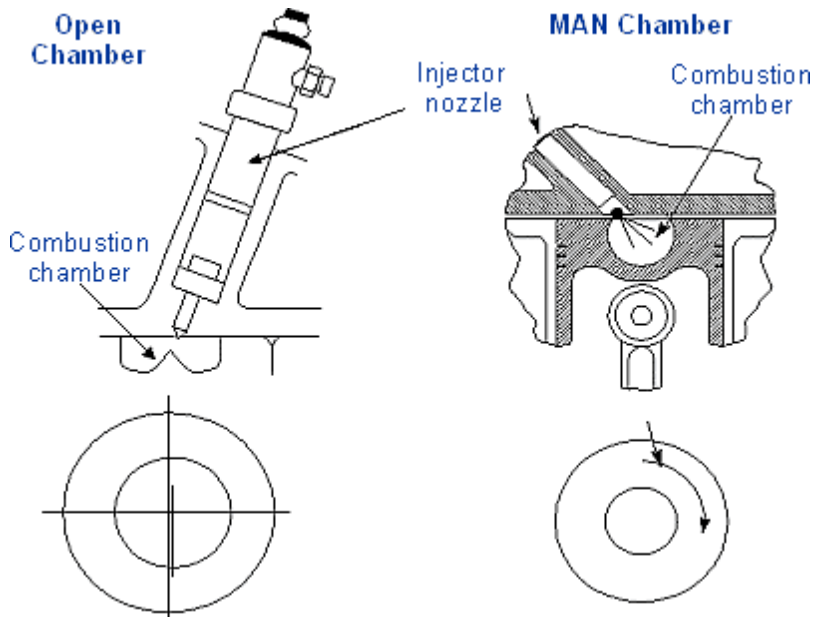

Figure 1: Direct injection fuel system.[1]

♦ Pilot Injection
♦ Post Injection

Additional Fuel Injector Features:

♦ High injection pressures that are independent of engine speed
♦ High injection pressures that are independent of fuel quantity
♦ Precision in fuel metering or injected quantity
♦ Ability to flexibly control and vary injection timing
♦ Ability to perform multiple injections in one combustion cycle
♦ Ability to meter very small quantities of fuel
♦ Minimize cycle-to-cycle variability
♦ Minimize cylinder-to-cylinder timing variations
♦ Minimize cycle-to-cycle timing variations

It has been determined that increasing the injection pressure has a great impact on fuel economy and emissions through its effects on fuel atomization and penetration/mixing. The desire to increase injection pressures has had a major influence on fuel system design. Modern fuel injection pressures range from 135-200 MPa (20,000-29,000psi), and fuel systems must be built to handle these pressures and still provide accurate injection timing and metering. All the features of the fuel injection system can drive the cost of that system up to 30% of the total engine cost.[2]

There are three main types of fuel injection systems and what seems like an infinite amount of variations on those three primary systems. Early diesel fuel injections systems were of the ***pump-line-nozzle (PLN)*** configuration. This configuration was entirely mechanical in operation. In the PLN configuration a central injection pump provides the high pressure for the separate injection nozzle located in the cylinder head above each cylinder. Fuel lines of exactly equal length connect each pump plunger (sometimes each injector has its own pump plunger or unit pump and sometimes there is a fuel 'distributor' injection pump) with the associated injection nozzle. The injection nozzles in this configuration are fairly simple devices incorporating a spring-loaded needle valve and orifices sufficient to provide fuel atomization. (Note there is a Cummings engine with this configuration located in the lobby of the HTML building at ORNL.) Problems with this system are that the maximum pressure of this system is limited compared to others due to fuel line 'dynamics', pressure wave dynamics in the fuel lines cause inaccuracies in the injection timing and metering, and the mechanical controls are limited in the number of variables that can be monitored. Another drawback of this system is that injection pressure depends on engine speed.[2,3]

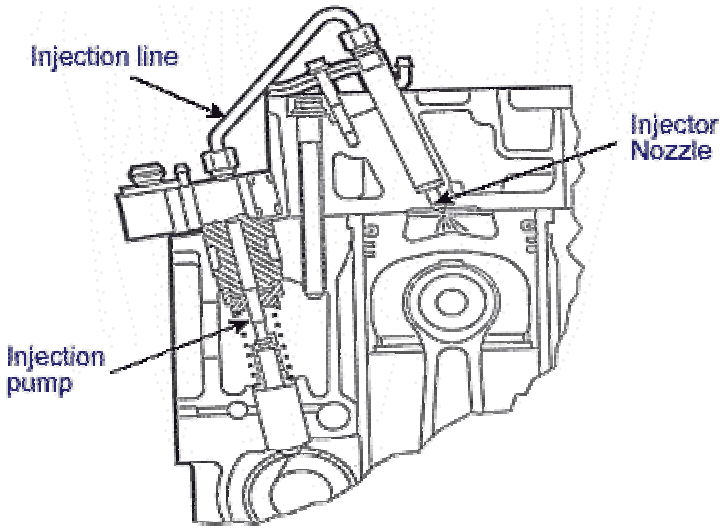

Figure 2: Bosch variation of the pump-line-nozzle configuration called the unit-pump configuration. Note that the injection pump is driven by a cam shaft. An engine with this injection system is located in the lobby of the HTML building.[3]

The unit injector (UI) system is a system that incorporates a high pressure pumping element into each injector. This system is capable of higher pressures and more accurate metering due to the absence of high-pressure fuel lines. An overhead camshaft drives the unit injector. The plunger is rotated by a rack to vary the alignment of fuel flow grooves inside the injector to vary injection timing and metering. This configuration is shown in Figure 3.

Notice the lower part of the unit injector contains a spring-loaded needle valve in Figure 3. The upper portion of this needle valve has a conical shape. When the injection sequence begins, the

pressure increases below the conical portion of this valve until the valve is lifted off of its seat, and fuel is allowed to enter the engine. This is a common feature of many types of fuel injection systems.[2]

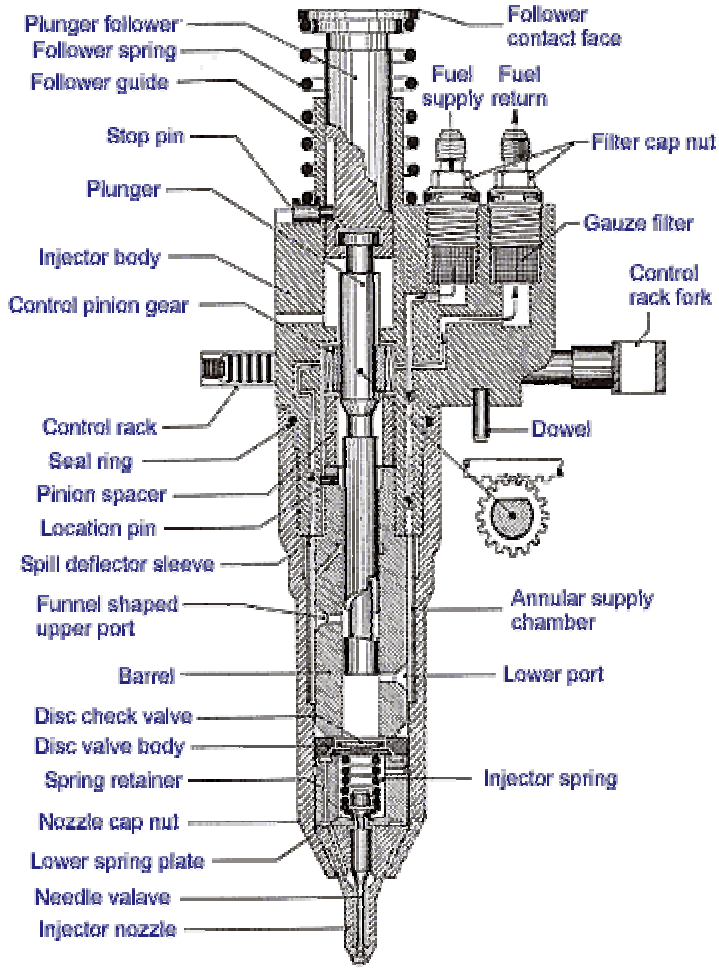

Figure 3: Unit injector schematic.[2]

The ***common-rail*** fuel injection system incorporates many of the features required by today's engines in a fairly simple system. The common rail system features a common fuel accumulator or 'rail' at high pressure located in close proximity to a row of fuel injectors along the engine block. Short, high-pressure injection lines connect the common-rail to the engine injectors that can be actuated by a variety of mechanical (overhead cam or rocker arm) or electronic (solenoid valve or piezoelectric valve) methods. Figure 4 shows a method employed by Bosch incorporating solenoid valves to initiate fuel injection. The common rail system appears to be the easiest system to control electronically. Many gasoline-powered engines employ this method of fuel injection as well.[2,3,4]

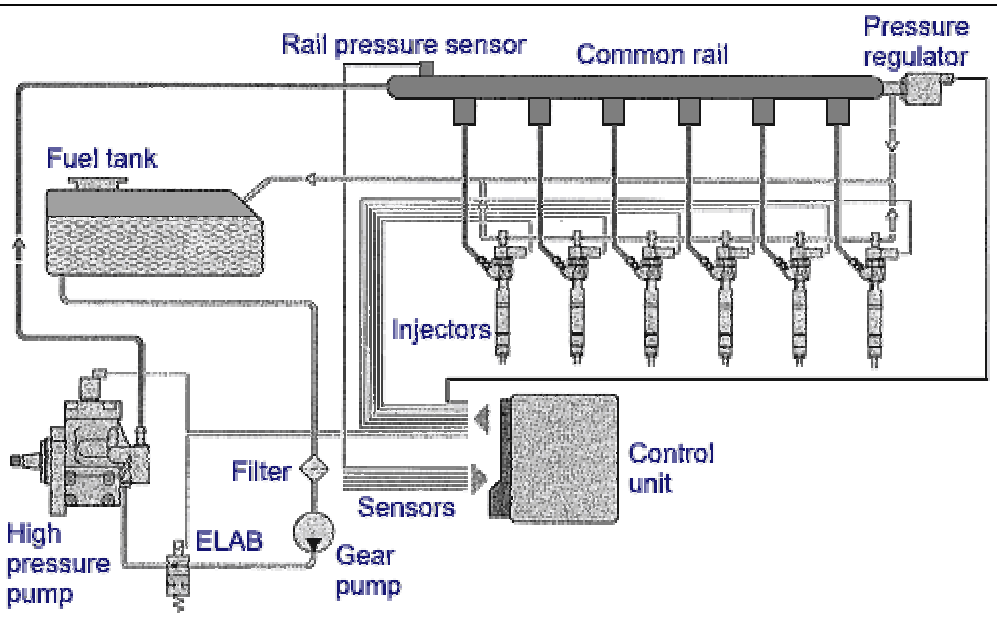

Figure 4: Bosch common-rail diesel fuel injection system.[2]

Actuators

Most fuel injectors make use of a needle valve to open and close the injection ports. These valves tend to be passively controlled by the hydraulic effects of the fuel pressure. The valve generally contains a shoulder, which is exposed to pressurized fuel. The force of the pressurized fuel against this shoulder opens the valve and allows the fuel to enter the combustion chamber through the injection ports, as is shown in Figure 5. The pressure supplied to raise the valve can be supplied by a piston internal to the injector as it the case in the unit injector. In certain cases, high-pressure fuel exists both above and below the needle valve in a pressure balanced valve. In the case of the pressure-balanced valve, the control valve acts to release the pressure above the valve allowing the valve to open. In these situations, the piezoelectric or other actuator operates the valve controlling this pressure. An example of this is the Siemen's fuel injector shown in Figure 7. It is estimated that the actuator needs to be capable of $2x10^9$ actuations over the life of the engine.

Actuator technology has greatly improved in response to microprocessor development and the requirements of electronically controlled fuel injection systems. Solenoid valves have been the most common form of electrical actuation, thus far. Initial designs had problems with high power consumption since they had to develop enough force to withstand high injection pressures. However, more recent designs have used mechanisms that take advantage of the pressure in the system to provide improved sealing and actuation, and reserving the electrical component for control only. Bosch employs solenoids for control rack actuation and spill valve actuation in a distributor pump. The response time of these electromagnetic-driven systems is about 300 ms.

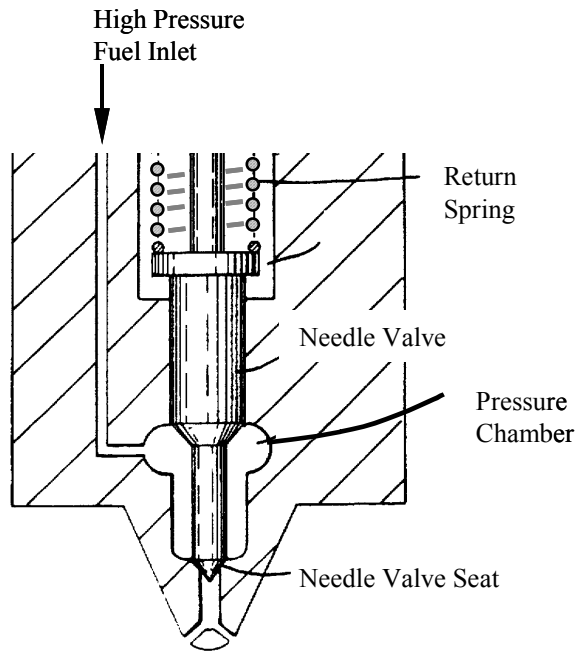

Figure 5: Needle valve actuation schematic. High-pressure fuel pushes the needle valve to raise off of the seat and the fuel injection cycle to begins.

A prototype piezoelectric actuated injector is shown in Figure 6. The main benefits of piezoelectric actuated valves are extremely fast and accurate valve actuation. Piezoelectric crystals seem to work well with the high injection pressures required. The prototype injector is capable of multiple injections, pilot injection and split injection, which can result in reduced engine noise, smoke emissions and fuel consumption. Utilizing a pressure balanced three-way

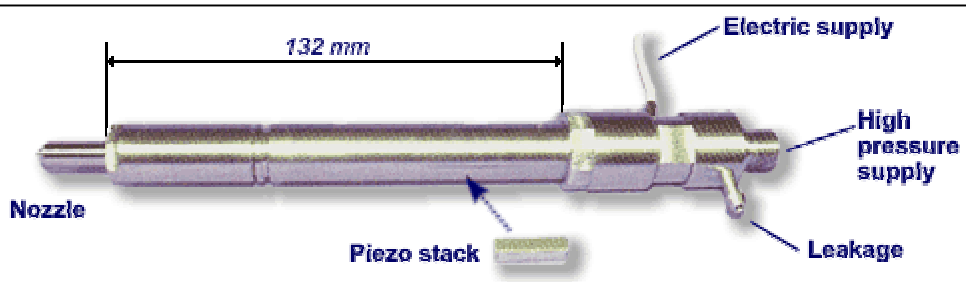

Figure 6: Piezoelectrically actuated injector.[2]

servo valve and a small piezo-actuator (0.5 cm^3 in volume), this injector is capable of extremely low injection quantities of less than 1 mm^3/stroke with good injection quantity repeatability up to rail pressures of 158 MPa (23,000 psi). This injector is quite attractive for small DI diesel engines, where exact and fast fuel metering of very small quantities for pilot injection may be required.

Because of its low moving mass inside the injector, the dynamics are significantly improved compared to conventional high pressure fuel injectors, resulting in a nozzle needle transient time of about 0.25 ms, a marked improvement over electromagnetic solenoid valves. Due to its unique design, this injector requires 0.04 Ws/stroke at low operating current and a maximum voltage of 200 V. Siemens commercialized piezoelectric technology in September of 2000 in a common rail injection system for the Peugeot 307 automobile.[2,4]

A patent search discovered that a significant amount of work has been performed on the use of piezoelectric crystals to actuate fuel injectors in recent years. A list of the patents awarded in the last ten years is included in the Appendix sorted by company. Several designs add the piezoelectric element to directly lift the needle valve or as part of the spring seat to change the amount of fuel pressure required to lift the needle valve. Some designs use the piezo element to control the inlet valve or metering valve. Most designs have seen the need to encapsulate the piezo element or seal the piezo element off from the fuel, as the fuel is apparently damaging to the piezo element. Many patented designs did not seem to require an amplification of the piezo crystal's motion, however several use hydraulic amplification of piezo crystals movement, and one was found to use mechanical amplification with a piezo/Belleville washer type configuration. It is uncertain how well the unamplified injectors will operate, or if those companies were primarily claiming a certain piece of intellectual property or concept. The patents that seemed to correspond to fully developed injectors generally used hydraulic amplification.

Piezoelectric Motion Amplification Systems:
The stroke of the common piezoelectric actuator is approximately 0.1% of its length. Single crystal piezoelectric materials are capable of extending 0.6%, but would probably be too expensive to implement at current costs.[10] The relatively small stroke of the piezoelectric actuator necessitates the use of a system of amplifying this motion. Most patents reviewed used a hydraulic method of amplifying the motion of the piezo crystal. Such an amplification technology is shown in Siemens Patent illustrated in Figure 7.

Another issue that must be addressed in piezoelectric actuated fuel injectors is the difference between the coefficients of thermal expansion (CTE) between the steel injector body and the piezoelectric stack. Piezoelectric materials generally have a very low CTE. Due to this property, the expansion of the injector body can be greater than the stroke of the piezoelectric material. Several schemes have been utilized to address the CTE differences. The Siemens fuel injector and a few others have an additional valve in the hydraulic amplifier that allows additional liquid fuel to be added to the amplification chamber as necessary to compensate for changes in volume of the amplification chamber due to expansion. The refill valve can also compensate for any fuel leaked from the chamber. The amount of fuel leaked from the chamber may vary with wear on the system.

Figure 7 is a schematic of the operation of their piezoelectrically actuated fuel injector utilizing hydraulic amplification. The actuator moves a large piston displacing a volume of fuel. This volume of fuel displaces a smaller piston a greater distance for an amplification of the actuator's stroke. The injector uses a pressure-balanced needle valve. It is exposed to high-pressure fuel on both the upper and lower surfaces. The displacement of the control valve opens a port

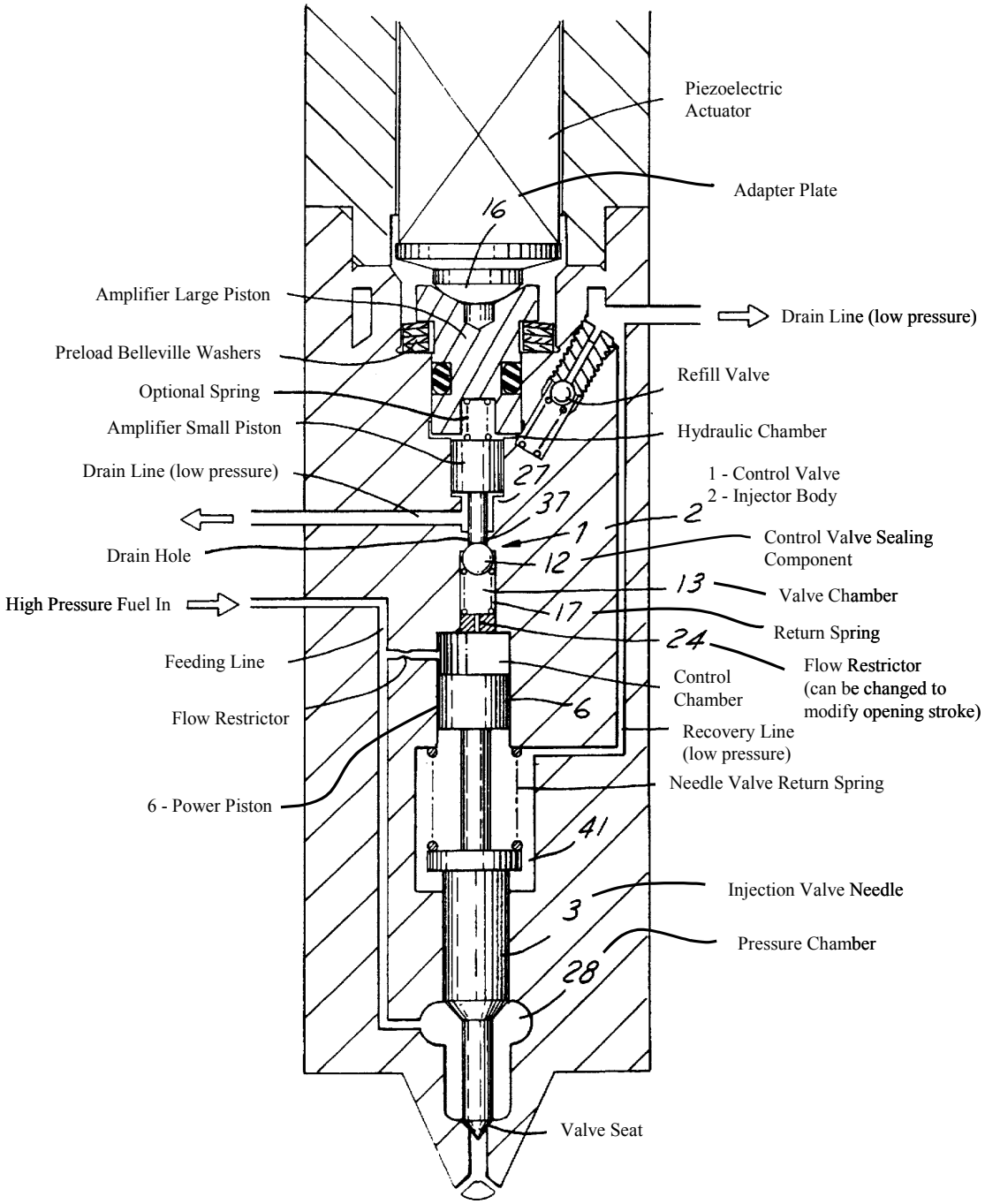

Figure 7. Schematic of Siemens piezoelectric fuel injector containing hydraulic amplification and a refill valve to compensate for thermal expansion and wear. Drawing is from United States Patent number 5,779,149. July 14, 1998. Siemens Automotive Corporation. Auburn Hills, Michigan.[8]

to the drain line and relieves the pressure holding the valve closed. Flow restrictors are used to modify the rate that the valve opens and closes. A refill valve is present to allow more fuel into the hydraulic chamber as needed to thermal expansion or wear. This is a schematic to illustrate

how the valve works, and not a print of the actual injector. The actual injector would be fabricated as a series of concentric cylinders that are assembled thermally with interference fits to ensure that they don't leak. Machined flats or grooves on the sides of the cylinders form flow passages.[8]

Figure 8 displays a mechanically amplified fuel injector designed by Isuzu Motors. This design uses a disc-spring or Belleville washer as a lever and fulcrum mechanism to amplify the motion of the piezo device. The spring-disc washer is attached to a support member. The support

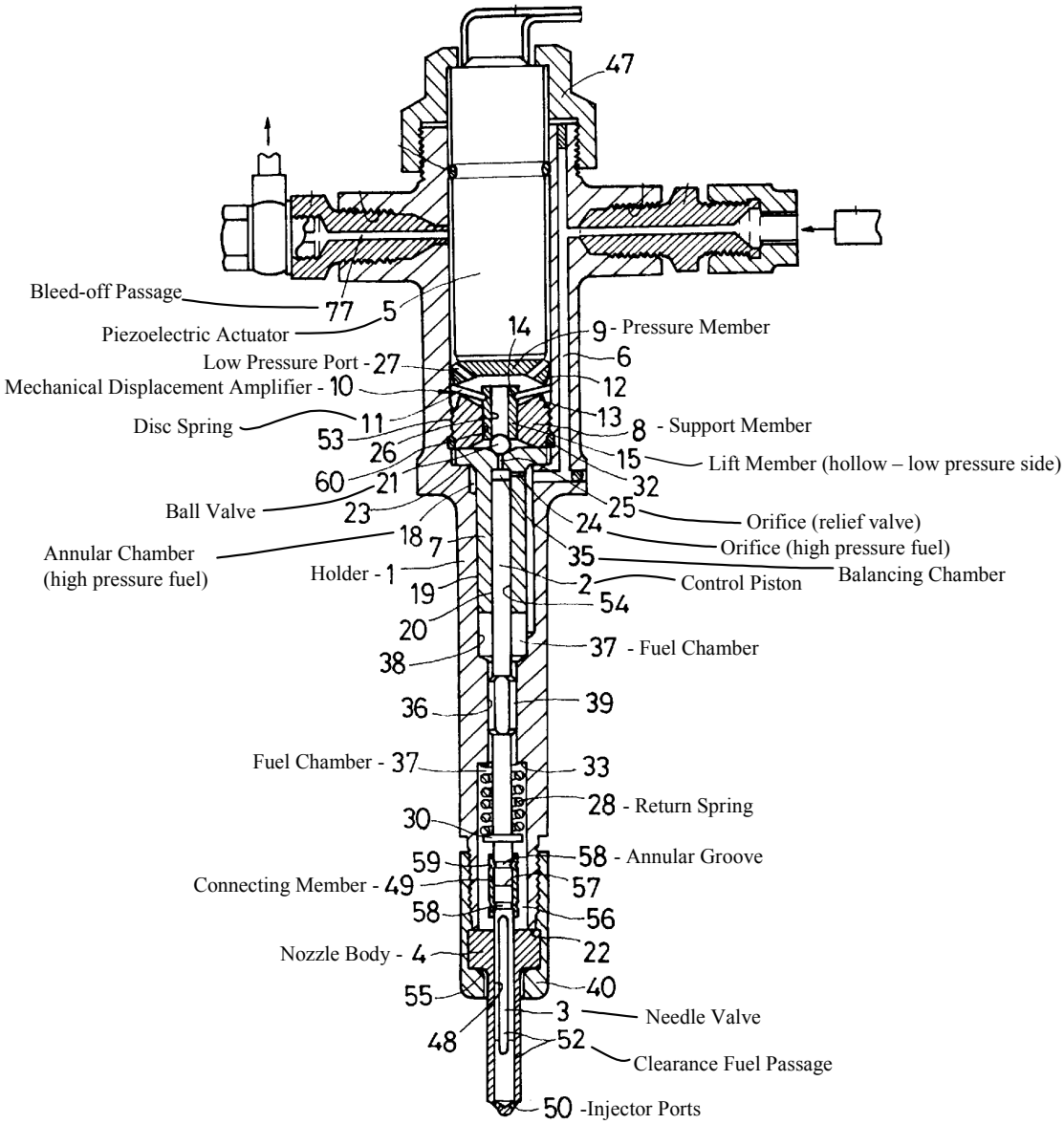

Figure 8: Mechanically amplified fuel injector. United States Patent Number 5,803,361. September 8, 1998. Isuzu Motors Ltd. Japan.[9]10

member opens and closes a ball valve. The ball valve relieves pressure on the control piston. The control piston is attached to the injection needle valve, and relieving the top surface of the control piston allows fuel to be injected in the cylinder.[9]

Conclusions

Piezoelectric actuation is of great interest for fuel injection technology due to extremely fast response times, and the large forces piezoelectric actuators are able to produce. The quick response times of the piezoelectric actuator give the possibility of multiple fuel injections per compression stroke. Pre-injecting a small amount of fuel warms the cylinder prior to the main injection reducing knock and particulate emissions. The drawbacks of these actuators are their small displacement and difference in coefficient of thermal expansion from other injector components. Also, piezoelectric stacks often have unique power requirements. Hydraulic amplification of the piezo actuator's motion has been used to overcome limitations in displacement.

The design life-cycle of a piezolectrically actuated fuel injector is 2×10^9 cycles. Designing a flexure-based amplifier or other mechanical amplification system that would survive 2×10^9 cycles would be challenging due to fatigue and wear issues, but not impossible. One of the benefits of using a mechanical system to amplify the motion of the injection nozzle would be that it would be possible to design a system with direct control of the injection nozzle. Such a system would have the advantage of being able to vary the amount that the valve opens, and give more direct control. If a mechanically amplified system were used, steps would have to be taken to compensate for any CTE mismatches in the system.

Fuel injectors are commonly precision machined from steel and stainless steel materials and have an excellent surface finish. The materials and manufacturing methods used for fuel injectors lend themselves to good fatigue strength. Steel materials exhibit a material property with respect to fatigue called the endurance limit (S_e), and as long as the stress in the material does not exceed the endurance limit, an "infinite" number of fatigue cycles will not result in failure. Nonferrous materials typically do not have an endurance limit and can only be designed for "infinite" life when used in very light duty applications. Even though components are designed using endurance limits, a testing program should be utilized to ensure that failure would not occur under actual conditions.[9] Therefore, with careful design and material selection, it should be possible to design a mechanically amplified system which would meet the requirements of the diesel engine.

Injection systems using hydraulic amplification of piezoelectric motion typically use indirect control of the injection needle valve, which is generally a "poppet" valve and opens automatically when the internal pressure reaches a certain level. Injectors containing hydraulic amplification systems have the ability to self-compensate for wear. Hydraulic systems capable of compensating for wear and thermal expansion are only capable of applying positive forces and could not be used to apply both opening and closing forces. Other actuators have been explored in Oak Ridge that might benefit this application as well.

Appendix

Patents within the last five years incorporating piezoelectric technology in fuel injection systems. (Clicking on the number should bring up the USPTO web page for that patent.) Search criteria was that the patent abstract had to contain the words injector and piezoelectric or piezo-electric.

Patents assigned to Robert Bosch GmbH:

1 6,435,430 Fuel injection valve

2 6,425,376 Fuel injector

3 6,405,942 Fuel injector with compensating sealing element

4 6,371,085 Injector with a multilayer piezoelectric actuator

5 6,318,342 Fuel injection valve and pressure sensor combination

6 6,315,216 Injector comprising a piezo multilayer actuator for injection systems

7 6,240,905 Unit fuel injector

Patents assigned to Siemens:

1 6,400,066 Electronic compensator for a piezoelectric actuator

2 6,345,771 Multiple stack piezoelectric actuator for a fuel injector

3 5,779,149 Piezoelectric controlled common rail injector with hydraulic amplification of piezoelectric stroke

4 5,645,226 Solenoid motion initiator

Patents assigned to Delphi:

1 6,420,817 Method for detecting injection events in a piezoelectric actuated fuel injector

2 6,390,385 Fuel injector

3 6,345,606 Method for controlling fuel rail pressure using a piezoelectric actuated fuel injector

4 6,260,541 Hydraulic lash adjuster

Patents assigned to Cummins:

1 6,253,736 Fuel injector nozzle assembly with feedback control

2 5,979,803 Fuel injector with pressure balanced needle valve

3 5,884,848 Fuel injector with piezoelectric and hydraulically actuated needle valve

Patents assigned to Caterpillar

1 6,412,704 Fuel injector with rate shaping control through piezoelectric nozzle lift

2 6,079,641 Fuel injector with rate shaping control through piezoelectric nozzle lift

3 5,130,598 Apparatus for driving a piezoelectric actuator

Patents assigned to Lucas Industries pic (Great Britain):

1 6,234,404 Fuel injector

2 6,196,472 Fuel Injector

Patents assigned to DaimlerChrysler AG:

1 6,302,333 Injector for fuel injector systems

2 6,085,990 Piezoelectric injector for fuel-injection systems of internal combustion engines

Patents assigned to Detroit Diesel:

1 6,390,069 Fuel injector assembly and internal combustion engine including same

Patents assigned to Isuzu:

21 5,803,361 Fuel injector for internal combustion engines

Stanadyne Automotive Corp:

18 5,988,142 Duration control of common rail fuel injector

Patents assigned to Toyota:

1 5,452,858 Fuel injector for internal combustion engine having throttle portion

2 4,976,245 Unit injector

3 4,966,119 Fuel injection control device for use in an engine

4 4,943,004 Actuator for a fuel injector

5 4,909,440 Fuel injector for an engine

6 4,782,807 Unit injector for an internal combustion engine

7 4,649,886 Fuel injection system for an internal combustion engine

8 4,635,849 Piezoelectric low-pressure fuel injector

9 4,579,283 Pressure responsive fuel injector actuated by pump

10 4,577,496 Transducer and holder there for ultrasonic acoustic tachometer

Patent Applications 2001-2002

1 20020130595 Method for manufacturing piezoelectric actuators and a piezoelectric actuator
2 20020117939 Piezoelectric actuator drive circuit and fuel injection system
3 20020117560 Hydraulic control valve and fuel injector using same
4 20020113717 Method and apparatus for LWD shear velocity measurement
5 20020084872 Piezoelectric device and method for producing the same
6 20020084723 Piezoelectric actuator with insulating member separate from piezoelectric device
7 20020084350 Piezoelectric device for injector, method for producing the same, and injector
8 20020083919 Method for injection fuel, with multiple triggering of a control valve
9 20020053860 Stacked piezoelectric device and method of fabrication thereof
10 20020041475 Method and device for detecting a fault current across a piezoelectric actuator of an injector or its high voltage supply lead
11 20020023622 Method and apparatus for regulating voltages and voltage gradients for driving piezoelectric elements
12 20020017832 Piezoelectric element for injector
13 20020017280 Online optimization of injection systems having piezoelectric elements
14 20020008440 Method and apparatus for timed measurement of the voltage across a device in the charging circuit of a piezoelectric element
15 20020008159 Structure of fuel injector using piezoelectric actuator
16 20020005680 Piezoelectric device for injector
17 20020000218 Fuel injection system
18 20010050512 Compensation of batch variation in the travel due to variations in the layer thickness or number of layers in multi-layer piezoelectric elements
19 20010047796 Piezoelectric device for injector
20 20010035465 Fuel injector with rate shaping control through piezoelectric nozzle lift
21 20010032058 Method and apparatus for controlling system parameters
22 20010028204 Method and apparatus for charging a piezoelectric element
23 20010027780 Method and apparatus for determining charge quantity during charging and discharging of piezoelectric elements
24 20010022489 Method for manufacturing piezoelectric actuators and a piezoelectric actuator

Bibliography

1. "The Case for the Diesel Engine" http://www.dieselnet.com/tech/diesel_case.html
2. "Diesel Fuel Injection" http://www.dieselnet.com/tech/diesel_fuel.html
3. "Pump-Line-Nozzle Injection System" http://www.dieselnet.com/tech/diesel_fuel_pln.html

4. "Common Rail Fuel Injection" http://www.dieselnet.com/tech/diesel_fi_cr.html
5. "Advanced Injection Systems and Their Control" http://www.dieselnet.com/tech/diesel_fuel_adv.html
6. "Injection Systems for Heavy Duty Engines" http://www.dieselnet.com/tech/diesel_fuel_pro.html
7. "Advanced Technologies: Fuel Injection and Combustion" http://www.dieselnet.com/tech/engine_adv_fi.html
8. United States Patent number 5,779,149. July 14, 1998. Siemens Automotive Corporation. Auburn Hills, Michigan.
9. United States Patent Number 5,803,361. September 8, 1998. Isuzu Motors Ltd. Japan.
10. Shigley, J.E. and Mitchell, L.D., Mechanical Engineering Design, McGraw-Hill Book Company, 1983, pp270-342.
11. Shrout, T.R. Penn State University, Center for Single Crystal Piezoelectric Materials, http://www.mri.psu.edu/centers/cscpm.asp

Status of Milestones

1) Evaluate and characterize commercially available PZT materials. Seek methods to improve the properties of these materials through alternative processing and forming methods. Fabricate new PZT compositions that allow sintering of the PZT materials at lower temperatures.

Status: The evaluations of new commercial materials and low temperature PZT materials planned for this milestone are complete.

2) Fabricate new PZT compositions to seek improvement in the electrical and mechanical properties. More specifically, research work will center on dopants that increase toughness of PZT materials.

Status: The evaluations of dopant materials that increase toughness of PZT materials for this milestone are complete. The study is included in the present report. Further work may follow in FY 2003 to include more samples to give a more complete statistical analysis.

3) Use ORNL expertise in motion amplifier devices to design and fabricate motion-amplifying fixtures for fuel injector assemblies. A paper study will be conducted to compare the advantages of fluid-mediated diaphragm amplifiers versus machined, bending structures.
Status: The paper study is included in this report. The emphasis of the study was expanded to include a basic discussion of fuel injector technologies and recent patents that cover the use of piezoelectric materials for fuel injectors.

Low-Cost Manufacturing Processes for Ceramic and Cermet Diesel Engine Components

D. E. Wittmer
Southern Illinois University

Objective/Scope

The purpose of this work is to investigate the potential of low-cost manufacturing processes for ceramic and cermet diesel engine components. The primary task is to develop cost effective processing, forming and sintering methodologies for cermet and ceramic formulations, used by industrial diesel engine manufacturers.

Technical Highlights

Task 1. Collaboration with industrial partner(s).

This task involves the collaboration with industrial partners to assist them in processing and sintering of their diesel engine components. Our goal is provide assistance in processing and sintering which may result in a reduction in surface reactions and part warping. Moreover, this may also provide an alternative sintering process that will allow improved throughput efficiency and manufacturing economy. Due to the proprietary nature of this task, any research data generated from this task is normally controlled by the terms of each specific confidentiality agreement. The reporting of this data and any results are the responsibility of the industrial partner(s).

Task 2. Cost Effective Processing and Sintering of Diesel Engine Components

This task was completed and reported in previous quarterly report.

Task 3. Economic Comparison of Materials and Processing of Cermets for Use as Diesel Engine Components

This task involves the development of an economic model for comparing both materials and processing methods for cermets targeted for use as diesel engine components. The cermet is a combination of an intermetallic and TiC; where the intermetallic can be nickel aluminide, chrome aluminde, nickel chromium. Modification of these intermetallics may be necessary to obtain the properties desired.

During this reporting period, the costs for all of the various powders were obtained and the cost per kg was determined for both the raw material and the feedstock that could be used for low-pressure injection molding. The costs were determined for both the pre-alloyed and the reaction sintered intermetallic, keeping the TiC constant at 40 vol %. These results are shown in Tables

1, 2 and 3. As seen in these results, based on costs associated that have not been adjusted for volume, the feedstock for injection molding NA4RK (reaction sintered, nickel alumined-40 vol % Kennametal TiC) was found to be $32.48/kg or lower. Since none of the powders have been adjusted for large volume, this cost could potentially be reduced by up to 50%. This reduced cost could make it competitive with other materials, such as zirconia; however this remains to be proven. Similarly, the feedstock for NCF4RK (reaction sintered, nickel-chromium-iron-40 vol % Kennametal TiC) was found to be $32.59/kg or less. The pre-alloyed formulations (denoted by P) were all substantially higher because of the alloy powder expense.

During the next reporting period, the cost associated with the various processes associated with these intermetallic bonded cermets will be compiled and input into an economic model. These processes include injection molding, debinding, isopressing and sintering. Both the continuous sintering process and a commercial process based on a vacuum/pressure cycle will be explored.

Status of Milestones

1.	Collaboration with Industrial Partners	On Schedule
2.	Cost Effective Processing and Sintering of Diesel Engine Components	Completed
3.	Economic Comparison	On Schedule

Communications/Visits/Travel

D. E. Wittmer to ORNL to meet with Terry Tiegs for discussions.

Problems Encountered

None

Publications and Presentations

None

Table 1. Costs Associated with Metal and Pre-Alloyed Metal Powders Used for Intermetallics

Powder	**Manufacturer**	**Product ID**	**Particle size (□m)**	**Cost ($/kg)**
Al	Alfa Aesar	41000	3.0-4.5	$75.80
B	Cerac	B-1119	<1.0	$2,940.00
Fe	Alfa Aesar	00170	<10	$80.80
Ni	Novamet	Type 123	3.6	$22.05
Ni	Novamet	Type 4SP	<10	$32.67
Cr	ACU powder	CR301	-325 mesh	$29.63
NiAl	Xform		<44 or -325 mesh	$66.00
NiAlZrB	Homogeneous Metals Inc.	IC-50	-325 mesh	$62.70
NiCr	Alfa Aesar	13108	-140+325 mesh	$282.00
NiCrFe	Alfa Aesar	36604	<44 or -325 mesh	$160.00
TiC (H)	HC Starck		1.2 - 1.6	$95.00
TiC (K)	Kennametal	TIC1000	.8 - 1.2	$26.00

Table 2. Costs Associated with Binder for Low-Pressure Injection Molding

Constituent	Manufacturer	Cost/kg
Paraffin	Gulf Wax	$1.76
Petroleum Jelly	Panef	$7.40
Stearic Acid	Acros	$14.20

Table 3. Cost of Raw Materials and Feedstock for Low-Pressure Injection Molded Cermets

Composition	Optimized Formula	Feedstock ($/kg)	Raw Material ($/kg)
NA20F4PH	37 vol % binder	$77.36	$83.39
NA20F4PK	37 vol % binder	$46.11	$49.70
NA20F4RH	37 vol % binder	$73.93	$79.72
NA20F4RK	37 vol % binder	$42.54	$45.87
NA4PH	37 vol % binder	$73.03	$79.20
NA4PK	37 vol % binder	$41.37	$44.86
NA4RH	37 vol % binder	$64.47	$69.97
NA4RK	37 vol % binder	$32.48	$35.25
NCF4PH	37 vol % binder	$119.85	$129.44
NCF4PK	37 vol % binder	$89.41	$96.57
NCF4RH	39 vo l% binder	$62.34	$67.25
NCF4RK	39 vo l% binder	$32.59	$35.16
NC4PH	37 vol % binder	$178.99	$193.32
NC4PK	37 vol % binder	$148.56	$160.45
NC4RH	40 vol % binder	$52.51	$57.22
NC4RK	40 vol % binder	$23.08	$25.15

N = Nickel A = Aluminum (aluminide) F = Iron 4 = 40 vol %
P = Pre-alloyed R = Reaction Sintered H = H. C. Starck TiC K = Kennametal TiC

Low Cost-High Toughness Ceramics

T. N. Tiegs, F. C. Montgomery, and P. A. Menchhofer
Oak Ridge National Laboratory

Objective/Scope

Significant improvement in the reliability of structural ceramics for advanced diesel engine applications could be attained if the critical fracture toughness (K_{Ic}) were increased without strength degradation. Currently, the project is examining toughening of ceramics by incorporation of ductile intermetallic phases.

Technical Highlights

Previous studies have shown that the properties of the aluminide-bonded ceramics are attractive for diesel engine applications and consequently, development of these materials was started. At the present time, TiC-based composites with 40-60 vol. % Ni_3Al are being developed because they have expansion characteristics very close to those for steel. Preliminary wear testing indicated that improved wear resistance could be achieved by decreasing the grain size of the TiC. Achieving fine grain size with the high binder contents is difficult because of the large inter-grain distances. In addition, it was thought that changing the TiC grain shape from a highly faceted one to a more rounded equiaxed grain would reduce localized stress at sharp corners. This, in turn, would improve abrasion resistance from any wear debris. Consequently, grain size refinement is presently being studied. Several approaches can be used to control the final TiC grain size. The methods studied in the present report include: (1) use of additives to change the interface behavior of the growing TiC grains, and (2) reduction of the initial TiC particle size. The development effort is being done in collaboration with CoorsTek, Inc.

Alternate Precursors for Ni_3Al Formation - All previous work used a combination of Ni and NiAl for an in-situ reaction to form the Ni_3Al. Because the costs of the starting raw materials can be a significant fraction of the total cost of a component, alternative materials for fabricating the cermets is of interest. Compositions have been mixed and pressed that use just Ni and Al for the reaction synthesis of the Ni_3Al since both of these are reasonable cost raw materials. In addition, an Al-Ni product produced by a catalyst manufacturer in large quantities is being evaluated as a possible raw material. These samples have been fired using the same vacuum/low-pressure hot-isostatic-press cycle as previous samples to determine their densification behavior. For both compositions, the densities achieved were >99.5 % T. D.

While the densification was more than acceptable, the sample containing just elemental Al and Ni as the precursors deformed significantly during sintering. In addition, severe cracking was also observed. The deformation and cracking are believed due to non-uniform heating. It is speculated that during heat-up, the samples develop a hot-spot caused by the exothermic reaction between the elemental Al and Ni. Differential thermal analysis of the powder mixture showed a significant exotherm in the range of 640 to 660°C. This is at the melting point of the aluminum and has been observed in previous work. Further efforts will determine if some prereaction via intermediate temperature holds could result in a reduction of the exotherm or a more controlled reaction that would minimize distortion of the part. The sample utilizing the Al-Ni catalyst product is presently being machined into mechanical property specimens.

Statistical Processing of TiC-Ni_3Al Composites - Previously, the general property envelope for the TiC-Ni_3Al composites has been studied and the compositions refined. Further processing studies are needed to ascertain the viability of these materials for diesel engine applications. At the current time, plans are being formulated to study a variety of topics. The studies will examine lot-to-lot variation using statistically designed experiments, determine compaction behavior, assess dimensional control during sintering, identify suitable binders which will not add carbon ash during sintering, develop a viable and cost-effective source of NiAl powder, and perform a machining study.

The project activities will be in close association with CoorsTek Inc. (a parts supplier) for scale-up of the processing, and Cummins Engine Co. (end user) for rig testing of fabricated parts. In addition, efforts will also be coordinated with Southern Illinois University to determine fabrication variations between facilities.

Status of Milestones
On schedule.

Communications/Visits/Travel
None.

Problems Encountered
None.

Publications
None.

Synthesis of Powders for Titanium Carbide/Nickel Aluminide Cermets

Michelle Zeles, Christopher Gump, Alan Weimer
University of Colorado

Scale-up of Submicron TiC Synthesis

Up to this point, all the research on titanium carbide (TiC), nickel aluminide (NiAl), and their cermets has been done on a small scale. The reactions have all taken place inside a TGA crucible where only one to two grams of starting material can be processed. To produce fine TiC for cermet synthesis, TiC will first be produced at larger scale. It will then be used as a diluent to synthesize TiC/nickel aluminide intermetallic cermets. A new reactor is being designed to mimic the way the reactions would be run in an industrial process.

This new reactor will be placed inside a horizontal tube furnace that is capable of reaching temperatures up to 1700°C. The reactor will be composed of high purity graphite and hold about fifty grams of starting material (fifteen times more material than the TGA). Inert gas (Argon or Nitrogen) will flow through the enclosed reactor with a special plate inside the front of the reactor to insure the dispersion of the gas throughout the reactor. The attached Figures 1-4 show the specifications and design of the reactor. This design is being sent out for bid.

The process for producing TiC and the cermet is very similar to the process used in the small-scale TGA setup. To produce TiC, pellets of titania and carbon are extruded so the titania and carbon are in close proximity to react with each other. The titania and carbon black powders are milled together in a 3 to 1 molar ratio. Small amounts of corn and wheat starch are added (5% by mass) to the milled mixture. This dry powder mixture is then mixed with water. The starch and water act as a binder for the mixture and form a paste that is then run through the extruder to form the pellets. These pellets are dried in the new reactor at around 300°C for about four hours to drive off the water and calcine the starches. Afterwards, the temperature will be increased to 1500°C for carbothermal reduction of the TiO_2 to form TiC. The TiC product will then be used as the diluent material to synthesize fine nickel aluminide intermetallic based cermet powders. Nickel and aluminum will be mixed with TiC in the reactor and heated to a temperature of 700°C. The product from this reaction will be compared to the product obtained from the TGA experiments. Samples will be submitted to ORNL scientists for evaluation.

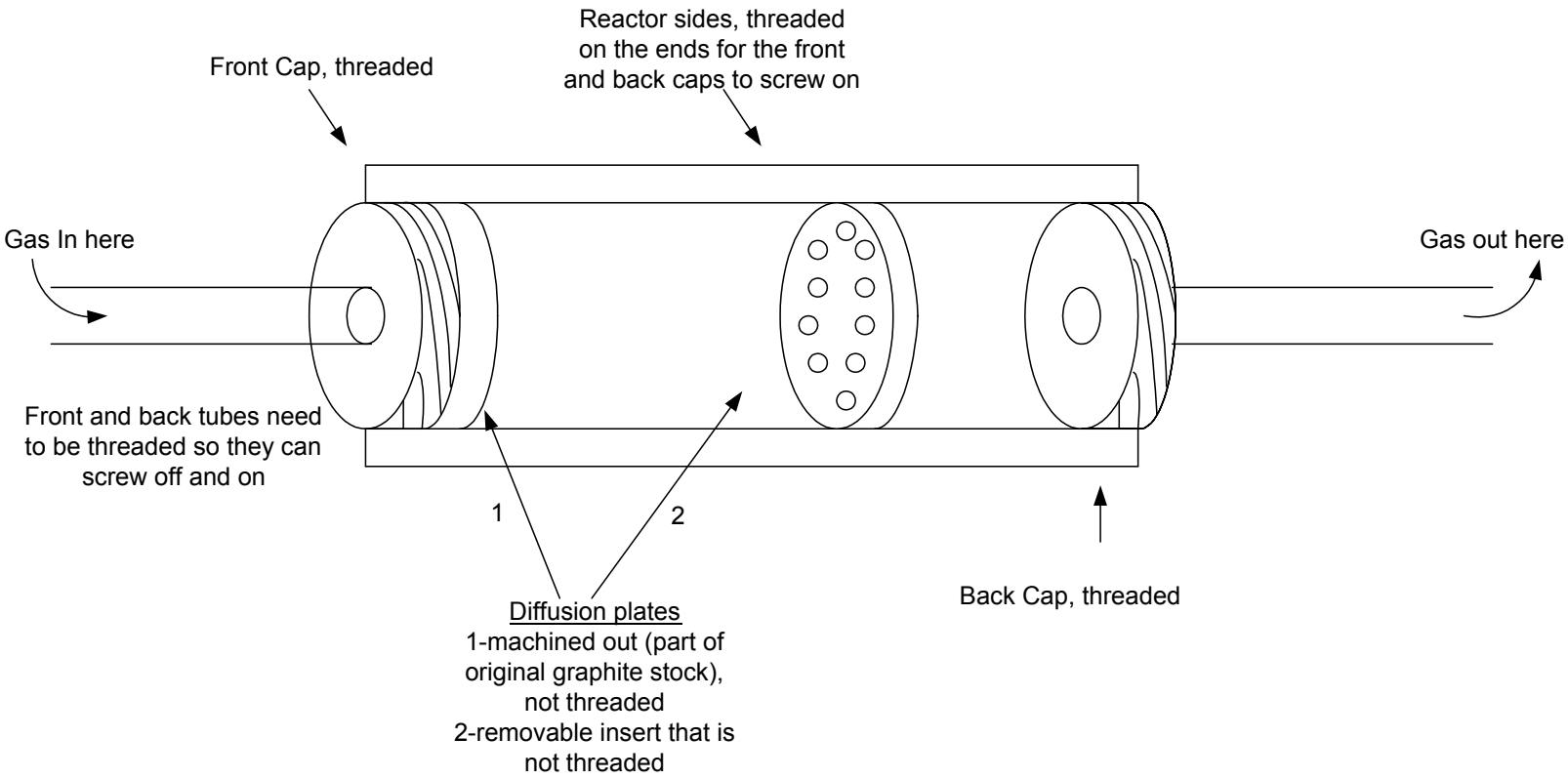

This reactor must be made out of high or ultra high purity graphite. The temperatures it will be subjected is anywhere from 300 deg C to 1500 deg C. This reactor needs to fit inside a horizontal tube furnace with a hot zone of 3 inches in length. The inner diameter of the tube furnace is 2 inches and the reactor fits inside it.

Figure 1 - Overall view of the reactor

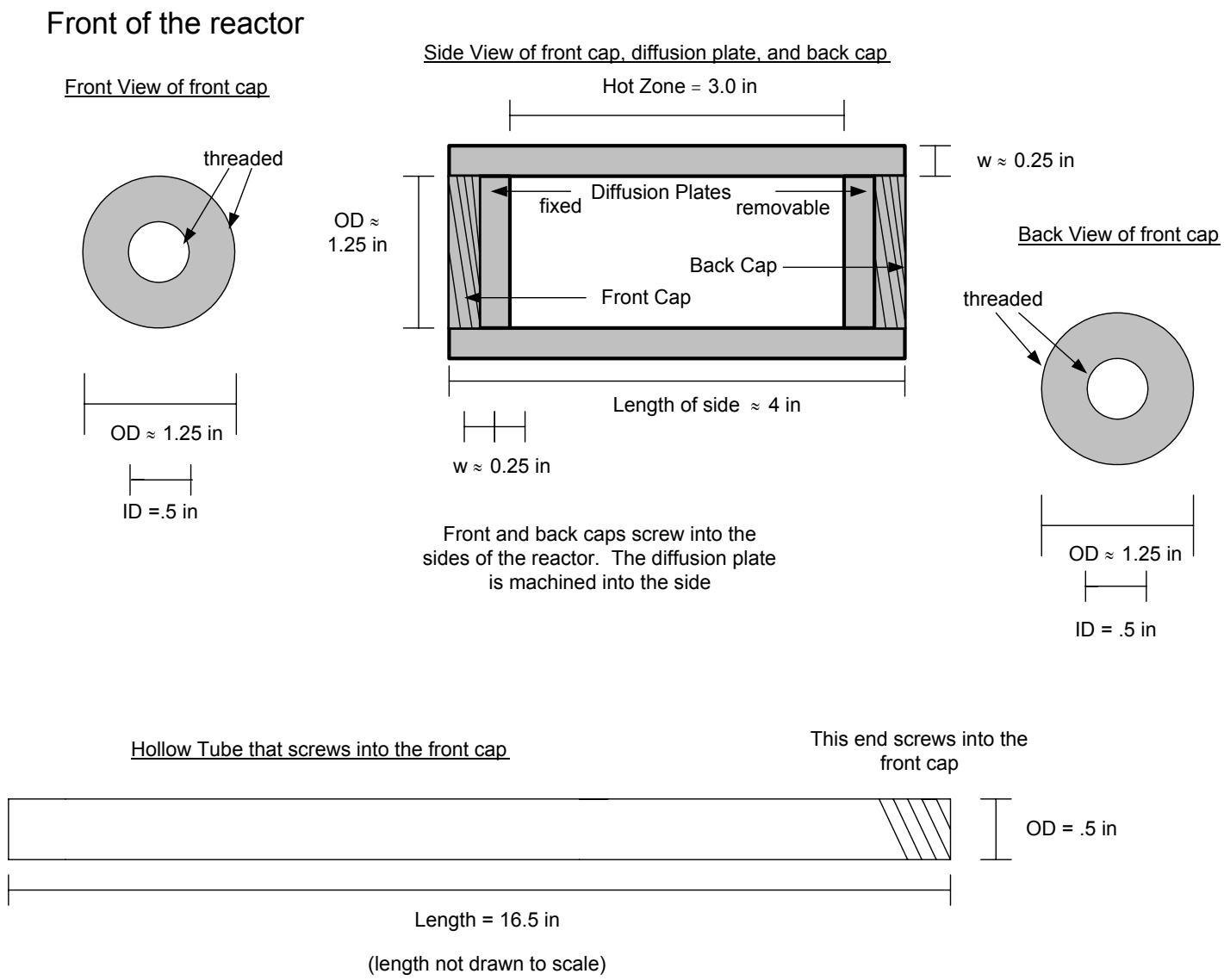

Figure 2 - Front and side view of the reactor with specifications

Diffusion Plate

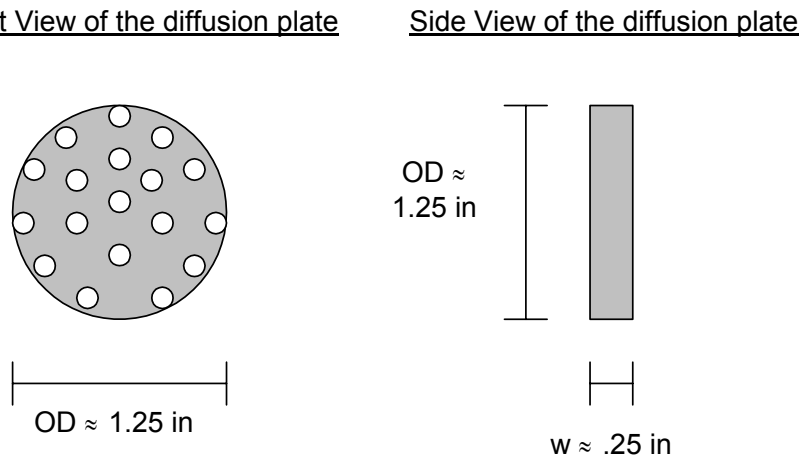

Holes NOT drawn to scale. They must be very small to let the gas (argon) diffuse through but not the specimen. The gas needs to be spread throughout the tube. The holes should be 1/32 inch if possible and there should be about 20 individual holes

These two plates serve two different purposes and the plates look the same but are slightly different. The first plate is next to the front cap and must be machined into the reactor (connected to the sides). The point for this is so the incoming gas is dispersed evenly throughout the reactor and doesn't escape around the side of the plate. The second plate is in front of the back cap. The job of the second plate is to keep all product in the reactor and not escape into the out gas. The second plate is removable so that samples can be put into the reactor and the plate will stand between the samples and the back cap.

Figure 3 – View of the diffusion plate with information on the purpose of the each plate

Back of the Reactor

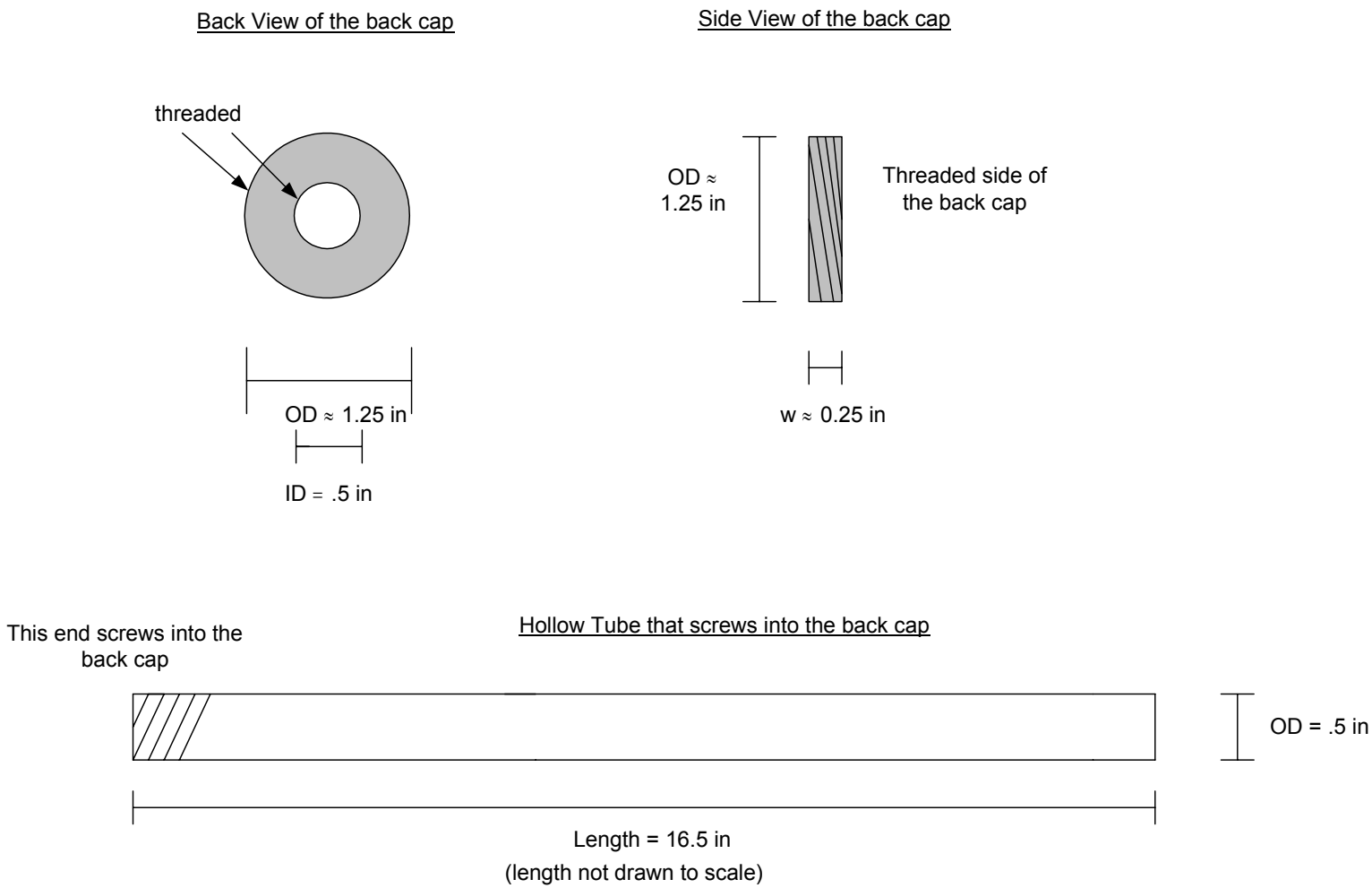

Figure 4 – The back view of the reactor

Intermetallic-Bonded Cermets

P. F. Becher and S. B. Waters
Oak Ridge National Laboratory

Objective/Scope

The goal of this task is to develop materials for diesel engine applications, specifically for fuel delivery systems and wear components (e.g., valve seats and turbocharger components). This will require materials that have a minimum hardness of 11 GPa and a thermal expansion coefficient of between 10 to 15 x 10^{-6}/°C. The material should also have excellent corrosion resistance in a diesel engine environment, flexure strength in excess of 700 MPa, and fracture toughness greater than 10 MPa√m to ensure long-term reliability. The material should also be compatible with steels and not cause excessive wear of the steel counter face. The upper temperature limit for fuel delivery systems applications is 200° C, and for the other wear applications, the limit is 815° C. Finally, the total material processing costs for these advanced materials should be competitive with competing technologies such as TiN or other ceramic coatings on high-speed tool steels.

Technical Highlights

Based on the successful development of high strength-high toughness Ni_3Al bonded nonoxide-based cermets, it was felt that there was value in exploring the potential for oxide-based cermets. However, past studies reveal that fabrication of cermets containing an oxide and aluminum-based intermetallics is inhibited by the inability of the intermetallic to wet the oxide [1]. This problem is similar to the poor wetting of oxides by aluminum and its alloys. The oxidation of the aluminum surface is, of course, thermodynamically favored under most conditions. In the last report, the approach of adding carbon to reduce the contact angle between molten aluminum on alumina and thus improving the wetting was discussed. Apparently, the carbon coating on the alumina substrate is sufficient to overcome the formation of an oxide layer on the aluminum droplet that inhibits wetting.

Another approach utilizes the exothermic reaction between aluminum and NiO to form mixtures of Al_2O_3 and Ni, various Ni-Al intermetallic compounds depending on the formulation of the starting mixture [2,3]. Most previous work has relied on hot pressing to form high-density cermets in this system [e.g., 3], which limits the ability to fabricate complex shapes and adds to the processing cost. A preliminary experiment confirms that we were able to form an oxide-intermetallic product by sintering. The exothermic reaction can be controlled by the addition of Al_2O_3 to the starting mixture and by reducing the heating rate through the melting point of the aluminum [2]. Future studies will address how to tailor the starting compositions and sintering conditions to produce dense sintered oxide-based cermets and optimize their properties.

References

1. K.B. Alexander, J.H. Schneibel, H.-T. Lin and P.F. Becher, pp. 877-82 in Processing and Fabrication of Advanced Materials for High Temperature Applications III, V.A. Ravi, T.S. Srinivasan and J.J. Moore (eds.), TMS, Warrendale, PA, USA, 1994.
2. S. Schicker, D. E. Garcia, J. Bruhn, R. Janssen and N. Claussen, *Acta Mater*. 46(7) 2485-92 (1998).
3. C. H. Henager, Jr., J. L. Brimhall and L. N. Brush., *Mater. Sci. & Eng'g* A195: 65-74 (1995).

Status of Milestones
On Schedule

Communication/Visits/Travel
None

Publications
None

Low-Cost Manufacturing of Precision Diesel Engine Components

S.B. McSpadden, Jr.
Oak Ridge National Laboratory

Objective/Scope

- To develop and demonstrate optimized, cost-effective fabrication processes for producing precision components for use in diesel engines.
- To develop and demonstrate optimized, cost-effective, non-destructive testing methods for detecting and preventing machining-induced damage in engine components.

Technical Highlights

Scanning Acoustic Microscope Upgraded – The Ernst Leitz scanning acoustic microscope (ELSAM) has been upgraded with a new dual-computer-system and control/imaging software package and is fully operational. Since this microscope is now manufactured by Kraemer Scientific Instruments, GmbH, the microscope will be called the SAM2000 Scanning Acoustic Microscope (SAcM) in future references. The fully functional SAcM has working frequencies from 100 MHz to 2 GHz, offering spatial resolution up to 0.4 μm. The SAcM has unique capabilities and advantages when compared with other methods of microscopic imaging such as the optical microscope and the SEM:

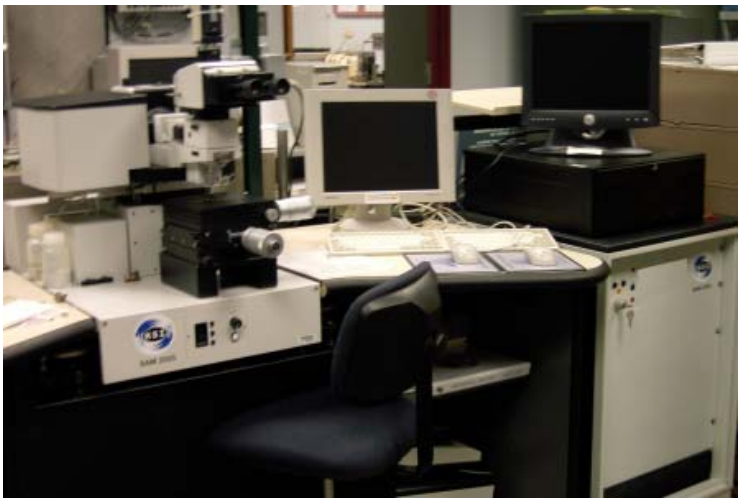

- It can generate images and measure subsurface features of both transparent and opaque solid bodies.
  - It can measure the thickness of coatings or thin layers. The minimum measurable thickness could be down to a few microns depending on different materials. Figure 1 shows the surface and subsurface images of a nickel alloy specimen coated with nickel-aluminide. By focusing on the surface, Fig. 1(a), and the interface, Fig. 1(c), the coating thickness was obtained, about 30 μm.
  - It can evaluate subsurface damage such as cracks caused by machining. Both the size and angle of a crack can be measured.
  - It can analyze microelectronic interconnections and packaging.
- It can generate images and analyze elastic properties.
  - Can visualize residual stress and strain distribution. (A special lens is needed for quantitative measurement.)
  - Can characterize both isotropic and anisotropic materials.
- It can be used to probe biological cells and tissues.

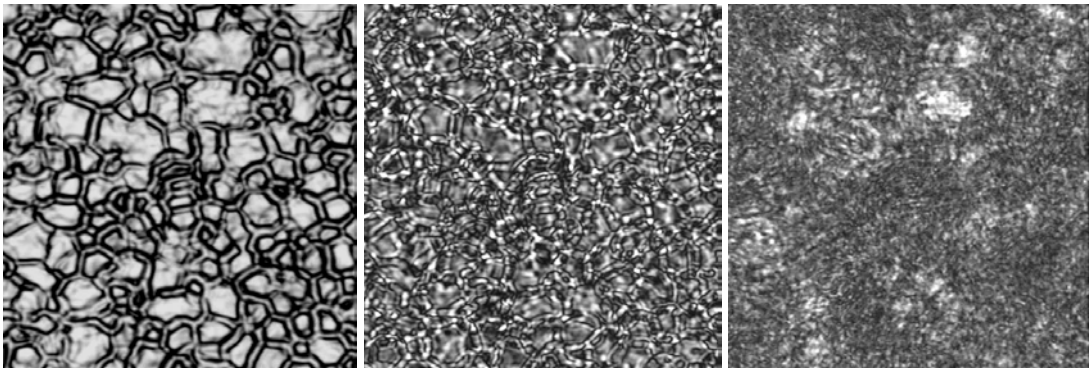

Figure 1. Examples of images generated while measuring the thickness of a NiAl coating on a Ni alloy sample. Working frequency: 400 MHz, coating thickness: 30 mm. (a) Focused on the surface. (b) Focused below the surface. (c) Focused on the interface.

Tabletop Turning and Machining Centers Provide New Machining Capabilities – Machining capabilities at the Machining, Inspection, and Tribology User Center have been expanded to include turning and milling with the purchase of two tabletop machines. The Prolight 3000™ computer-controlled lathe and the Benchman 4000™ vertical machining center have just been installed and will be modified to include dynamometer and other instrumentation in the near future. These miniature machine tools will provide much-needed new capabilities for machining research on high-performance materials. They have most of the capabilities of full-scale industrial machines, but have the advantages of a very small footprint, low initial cost, ease of operation, and extremely low operating and maintenance costs.

Communications/Visits/Travel

None.

Publications

None.

Cylindrical Wire Electrical Discharge Machining (EDM) and Temperature Measurement

Albert Shih
University of North Carolina

Objective/Scope

To develop precise, efficient, and cost-effective cylindrical Wire Electrical Discharge Machining (WEDM) process for cermet and other electrically conductive advanced engineering materials, and temperature measurement methods for grinding and diesel exhaust aftertreatment devices.

Technical Highlights

The infrared-based temperature measurement system for diesel exhaust aftertreatment filters was further developed. The infrared-based temperature measurement system uses a single crystal sapphire fiber with polished 45 deg tip to collect the infrared radiation from a small area inside the cavity walls of diesel exhaust aftertreatment filters. The infrared signal transmits through the fiber and collects by a PbS/PbSe two-color infrared sensor, which is sensitive to the radiation at two mid-infrared spectrum wavelengths, about 2.5 μm for PbS and 3.4 μm for PbSe, to enable the measurement of low, 250 to 700°C temperature. The accurate temperature measurement is important to understand the chemical reactions and regeneration process in diesel exhaust filters. The two-color sensor converts the radiation into two voltage outputs. Based on the theory of radiation thermometry, the temperature of the target can be derived from these two voltages. This quarterly report focuses on experimental results on measuring the temperature in a microwave-heated filter.

Setup for Mapping the Temperature Distribution in Microwave Heated Filters

A ceramic filter, provided by Industrial Ceramic Solutions LLC at Oak Ridge, TN, was used in the microwave heating experiment. This filter contains the SiC whisker, which reacts promptly and efficiently under microwave to generate heat. Figure 1 illustrates the positions to place the tip of the sapphire fiber to measure the real-time temperature vs. time data at 15 locations in a filter during microwave heating. The filter was placed in a fixed position in a microwave oven, as shown in Fig. 1(a). As shown in Fig. 1(b), five cavities, marked from A to E, are selected in the filter. In each cavity, as shown in Fig. 1(c), three locations in the back, center, and front of cavity are identified to place the tip of the sapphire fiber. The front is designated as the location where the fiber entering the fiber. The spacing from the front to center position and from the center to back position is 25.4 mm. There are 15 locations in the filter for the temperature measurement to study the uniformity of microwave heating. At every point, four repeated microwave heating tests are conducted. In total, 60 temperature vs. time data at 15 locations are collected and analyzed for mapping the temperature distribution and history in the microwave heating of a diesel exhaust aftertreatment filter.

The optical fiber was inserted into the filter through the wall of the microwave oven. An overview of the setup of the microwave heater, sapphire fiber, chopper, chopper control, thermoelectric cooling unit, two-color sensor, and data-acquisition system is shown in Fig. 2(a). A table is used to adjust the height of the fiber, as shown in Fig. 2(b). An array of holes, all smaller than 1 mm to prevent the leaking of microwave, was drilled on the wall of the microwave. This hole pattern matches to that of the filter and can guide the sapphire optical

fiber to the five cavities (A–E) shown in Fig. 1(b). Each microwave heating test lasts for 4 min. The output from PbS and PbSe sensor is recorded using an oscilloscope. After the 4 min of heating, the filter is cooled down. The fiber tip is placed to another position. Another 4 min. heating and sensor output recoding are conducted. These steps repeat for all 15 locations in the filter.

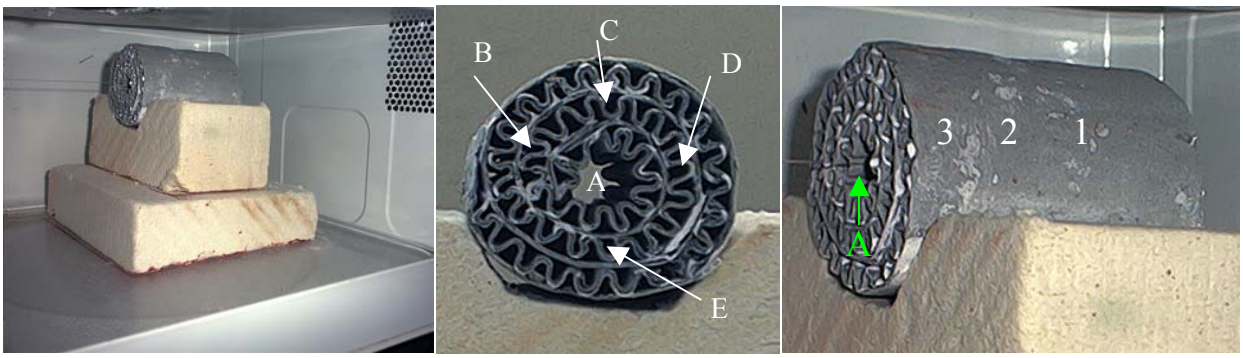

(a) (b) (c)

Fig. 1. Mapping the temperature distribution in a filter.

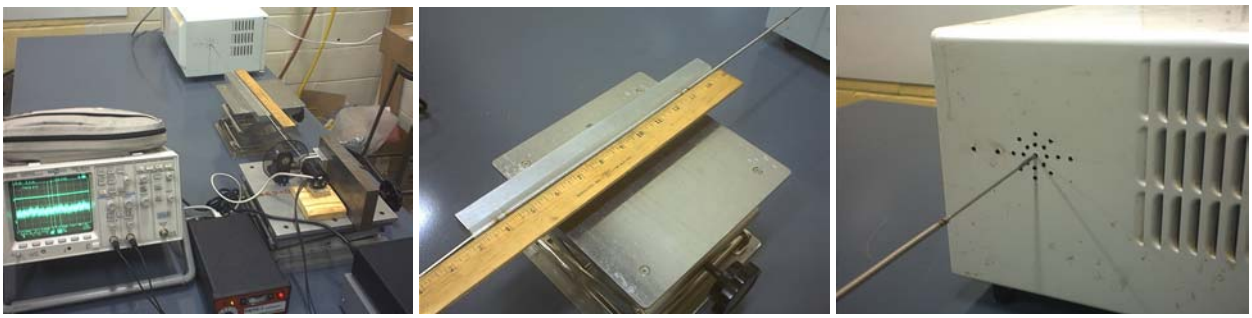

(a) (b) (c)

Fig. 2. Overview of the microwave heating experiment setup.

Since the filter is kept at the same position in the microwave oven, the electromagnetic field distribution and the filter heating are anticipated to be repeatable. The length and location of the sapphire fiber in the microwave did change at different measurement locations. The sapphire is transparent to microwave and its effect to the electromagnetic field distribution is negligible. The measured temperature at each of the location shall be repeatable. This assumption will be validated later by repeated heating tests and temperature measurement results.

Preliminary Experimental Results and Discussion

Figure 3 shows an example of the sensor output by microwave heating at the position A1. The sensor output was recorded in 1 min interval for the 4 min heating duration. The chopping frequency was set at 250Hz. Voltage outputs of PbS and PbSe had 4 ms period in the waveform, as indicated in Fig. 3. The peak-to-valley values of the waveforms were used to calculate the temperature according to the calibration curves documented in previous report.

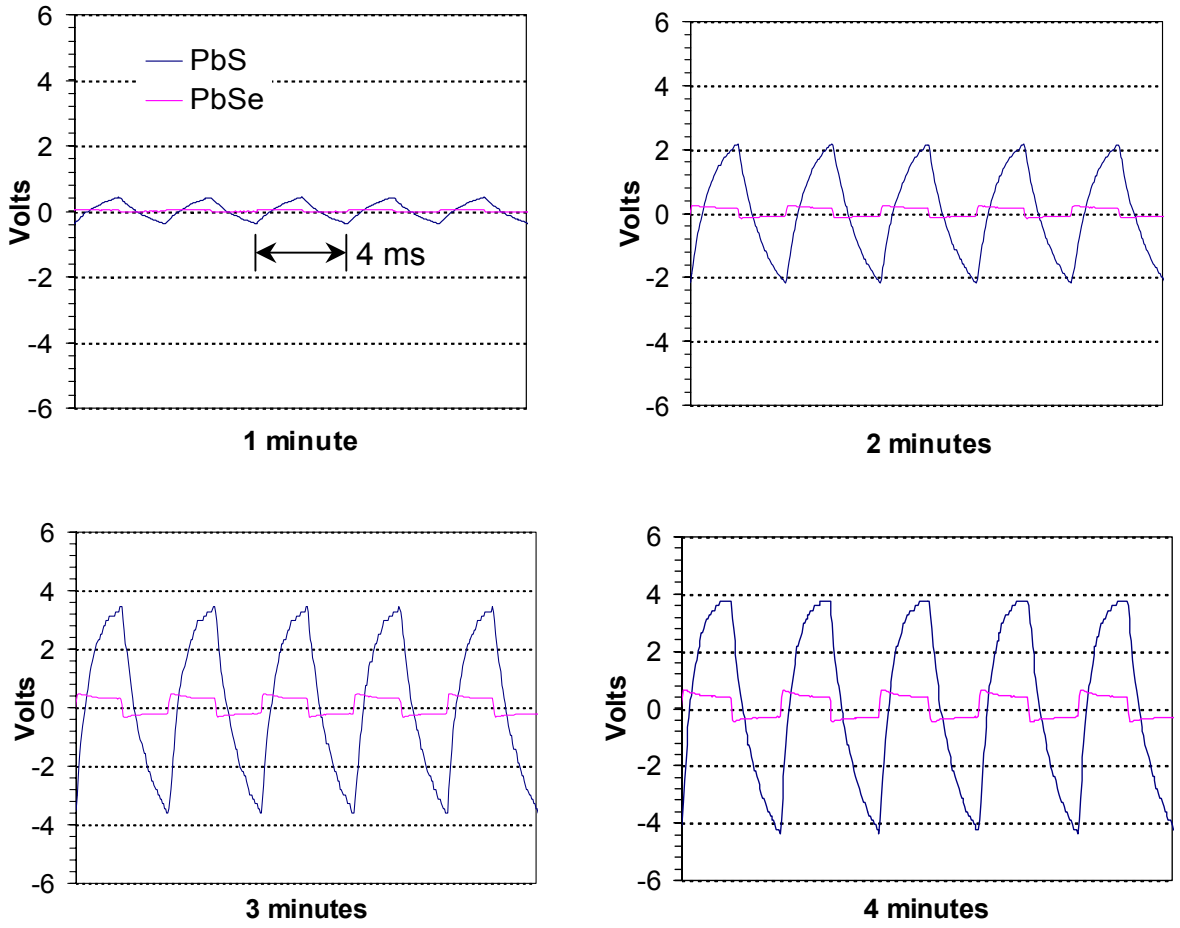

Fig. 3. Sensor output by microwave heating.

Both the one-color and two-color methods can be used to convert the peak-to-valley voltage readings to temperature. For the one-color method, PbS and PbSe can be treated as a one-color temperature sensor, and their voltage output can be used to predict the target temperature. For the two-color method, the ratio of PbS and PbSe output voltages is calculated and the temperature is derived using the calibration data. The temperature measurement results using both one-color and two-color methods are compared to identify a good approach to accurately convert the recorded voltage to filter temperature.

Results of analyzed temperatures at position A1 are presented in Tables 1, 2, 3, and 4. The four repeated heating tests are marked as Test I to IV. Temperature results using the PbS and PbSe outputs as two one-color sensors are listed in Table 1 and 2. Comparing the output voltages and the temperature in four repeated tests in Tables 1 and 2, the repeatability of temperature in repeated tests is good. This validates the assumption that the same heating condition occurs at the same location in the filter in a specific position in the microwave.

Results of temperature calculated using the ratio method are listed in Table 3. Since most of the ratio values in the first two minutes of heating are outside the ratio range generated in the calibration, which is from 2.69 to 1.7 corresponding to the temperature from 250°C to 850°C, the low temperature in early heating period cannot be found. This indicates that the current two-color method is still unable to detect the temperature below 500°C and further research, such as the newly developed spectrometer, is necessary.

Table 1. PbS voltage output and the converted temperature at A1.

Heating duration	Test I		Test II		Test III		Test IV	
	Volts	Temp (°C)	Volts	Temp (°C)	Volts	Temp (°C)	Volts	Temp (°C)
1 min.	0.688	329	0.813	342	0.625	321	0.625	321
2 min.	4.56	539	4.31	528	4.53	538	4.53	538
3 min.	7.19	658	7.03	651	7.03	651	7.19	658
4 min.	8.44	713	8.13	699	7.97	692	7.97	692

Table 2. PbSe voltage output and the converted temperature at A1.

Heating duration	Test I		Test II		Test III		Test IV	
	Volts	Temp (°C)	Volts	Temp (°C)	Volts	Temp (°C)	Volts	Temp (°C)
1 min.	0.0469	335	0.047	334	0.047	335	0.016	257
2 min.	0.297	507	0.275	497	0.281	500	0.281	500
3 min.	0.594	610	0.563	602	0.578	606	0.578	606
4 min.	0.813	667	0.766	653	0.766	653	0.750	649

Table 3. PbS/PbSe output ratio and the converted temperature at A1.

Heating duration	Test I		Test II		Test III		Test IV	
	Ratio	Temp (°C)	Ratio	Temp (°C)	Ratio	Temp (°C)	Ratio	Temp (°C)
1 min.	2.69	254	2.86	N/A	2.59	473	3.69	N/A
2 min.	2.73	N/A	2.75	N/A	2.78	N/A	2.78	N/A
3 min.	2.49	553	2.53	534	2.50	550	2.52	537
4 min.	2.34	618	2.36	609	2.34	617	2.36	609

Table 4. Average temperature results.

	1 min.	2 min.	3 min.	4 min.
PbS (one-color)	328	536	654	699
PbSe (on-color)	315	501	606	656
Ratio (two-color)	N/A	N/A	543	613

Discussion

The average of the four temperatures measured in repeated tests are listed in Table 4. The PbS and PbSe stand for the one-color method and the ratio is based on two-color method. It can be seen that the temperature reported by PbS is higher than that of PbSe. The lowest temperature is reported by the two-color ratio method.

Without the detailed knowledge on the emissivity of the filter material, it is not possible to judge which method is the most accurate. If the emissivity is unknown or varying during the measurement, the ratio method, in theory, can provide more accurate temperature predictions than the one-color method. This is based on the assumption that the emissivity at the two chosen wavelength ranges does not vary sharply in the measured temperature range. This is an on-going research in implementing the method developed in this study to assist the advancement of diesel exhaust filter technology. The emissivity of the filter material has been tested and the experimental data analysis is under way.

The fiber will work in a strenuous operating condition in the filter with different levels of exhaust gas flow through under different engine operating conditions. Varying amounts of diesel exhaust soot will obscure the fiber's field of view. The filter surface condition will also change due to the different levels of loading of soot and NOx. In this case, the ratio method is less affected by the changing conditions and, once again, in theory, can provide better prediction of the target temperature. This makes the two-color ratio method or even the spectrometer method more preferable than the one-color method. This is yet to be proven in field tests.

Without the effect of exhaust stream, the temperature results reported by regarding PbS and PbSe as two single-color sensors can be used to estimate the local temperature in the filter. An isothermal opaque cavity forms a blackbody and has unit emissivity inside. Since the filter cavities are small and long, if also isothermal, the apparent emissivity [1] in the filter is independent of the filter material itself and very close to the blackbody emissivity. This is the case for the calibration method mentioned in the last quarterly report. New calibration methods have been studied and will be discussed in more detail in the next quarterly report.

When the filter is heated by microwave, the temperature in a cavity of the filter is not uniform as expected and temperature gradients occur over the cavity. The apparent emissivity at any point of the inside cavity is no longer to be the unit. But, it is still generally high and closer to the blackbody emissivity due to the multi-reflective effect in the filter. The error resulting from the uncertainty in emissivity can be estimated by the following equation [1]:

$$\frac{dT}{T} = \frac{\lambda T}{c_2}\frac{d\varepsilon}{\varepsilon} \tag{1}$$

where T is the target temperature; λ is the chosen wavelength; ε is the (apparent) emissivity; and c_2=14388μm·K is the second radiation constant. If $d\varepsilon$ is set, the temperature error can be calculated. For example, the error reported by PbS sensor at the 4-minute mark in Test I is 34°C or 4.8%, if $d\varepsilon$ is set as 0.2. The research on error prediction is also on-going.

Status of Milestones

Milestone 1: Develop process technology to achieve high material removal rate in cylindrical WEDM of advanced engineering materials.

Status: Three journal and two conference papers have been published or accepted on this research.

Milestone 2: Determine the level of form tolerances and surface finish achievable by the cylindrical WEDM.

Status: Nothing to report. The surface finish was as low as 0.68 μm Ra, comparable to rough grinding, for the carbide materials.

Milestone 3: Prototype needles, armature pins, and plungers for diesel engine fuel injectors.

Status: Currently working with Cummins Technical Center to transfer the technology of cylindrical wire EDM for the roughing operation in prototype plunger manufacturing.

Milestone 4: Develop mathematical models for material removal rate and surface finish of the cylindrical WEDM.

Status: The mathematical models for material removal rate and surface finish have been derived. These results have been summarized in two technical papers.

Milestone 5: Characteristics of the recast layer after WEDM and cylindrical WEDM and the surface condition after abrasive blasting.

Status: The nano-indentation tests and Micro SiC abrasive blasting results are summarized in two technical papers.

Milestone 6: Development of the optical fiber based temperature measurement method, with applications for grinding process and diesel exhaust aftertreatment filters.

Status: The preliminary experimental results on measuring temperature in a microwave-heated filter were analyzed. The calibration method of the infrared-based temperature measurement system for diesel exhaust aftertreatment filters has been systematically studied. Due to the advancement of catalytic technology, the temperature for regeneration has been lowered. This is a new challenge for infrared-based temperature measurements.

Communications/Visit/Travel

John Kong, the PhD student who is working on the infrared-based diesel exhaust aftertreatment filter temperature measurement, is working at Cummins Technical Center in Fall 2002 semester as a Ph.D. co-cp student. He will further expand the methods used for infrared temperature measurements of diesel exhaust filters.

Albert Shih is planning to visit Cummins Technical Center on Oct. 21 and 22.

Publications

J. Qu and A. J. Shih, "Analytical Surface Roughness Parameters of an Ideal Profile Consisting of Elliptical or Circular Arcs," Machining Science and Technology (submitted).

J. Kong, A.J. Shih, R.O. Scattergood, T.M. Yonushonis, D.J. Gust, M.B. Grant, and S.B. McSpadden (2003) "Cost-Effective Form Grinding of Zirconia using Silicon Carbide Wheels and Ceramic Grinding Temperature Measurement," *2003 NSF Design, Service and Manufacturing Grantees and Research Conference*, Birmingham, Alabama, Jan. 6-9, 2003 (accepted).

References

[1] D.P. Dewitt and G.D. Nutter, *Theory and Practice of Radiation Thermometry*, John Wiley & Sons, 1989, pp. 60−80 & 565−623.

QUARTERLY PROGRESS REPORT

JULY-SEPTEMBER 2002

Task Title: **NDE/C Technology for Heavy Duty Diesel Engines:**

Fuel Delivery and Insulating Materials

Principle Investigator: **W. A. Ellingson**
Argonne National Laboratory

Objective/Scope

The objective of the work in this task (part of the Testing and Characterization research area of the Heavy Vehicle Propulsion System Materials Program) is to develop enabling nondestructive evaluation/characterization (NDE/C) technology for lower-cost and high-performance materials. Specifically, this project addresses development of advanced NDE/C technology for: (a) advanced fuel delivery systems (including injector nozzles), and (b) insulating materials for reducing heat losses in the combustion zone. Fuel delivery systems for heavy-duty diesel engines are complex, very expensive, and represent a significant portion of the cost of a heavy vehicle diesel engine. High pressures inside these fuel delivery systems contribute to poor fuel delivery and hence poor emissions. Materials development is part of Goal 3 of the heavy vehicle propulsion materials program. Insulating materials are also a significant materials development area because of the improvement in engine efficiency if reduced heat losses can be obtained. NDE/C technology that can provide information for reliable cost production and engine component surveillance would be of benefit to reaching the goals.

Technical Highlights

The technical highlight this period is that we have worked on the scanning using the ABB robot arm. Further that investigations are underway to better detect subsurface features using the polarized laser back-scatter method.

Technical progress

The efforts this period have been on modifying the scanning set on the robot arm for better data acquisition as well as better defining the optimum set up for the laser back-scatter to acquire subsurface features in the plungers.

(a) Robot arm back scatter laser scans

This period we modified the laser scatter data acquisition parameters for the 6-axis articulated arm robot. As a part of this effort, we again used the special aluminum plate previously discussed. The high-resolution back-scatter image of the aluminum plate was generated, see

Fig. 1, from a scan that consisted of sequential scan 135 lines with 180 points acquired on each line. The scan shown in Fig. 1 took 56 minutes to complete. The earlier version of the scans for this plate (see Fig. 2) was generated from a scan that consisted of 20 sequential lines with 100 points on each line. This scan took 3 minutes to complete.

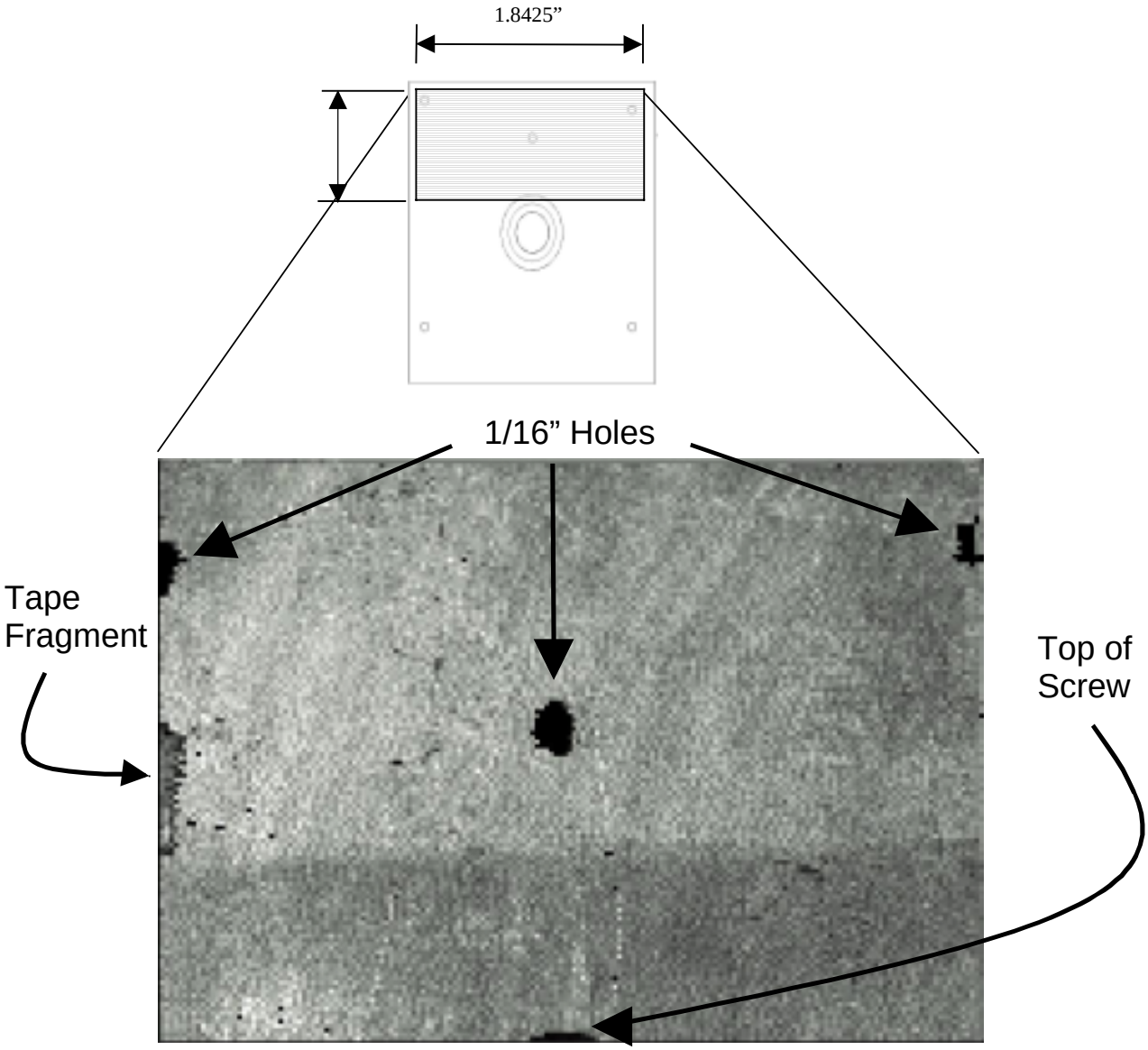

Fig. 1. High resolution laser back-scatter scan with robot arm

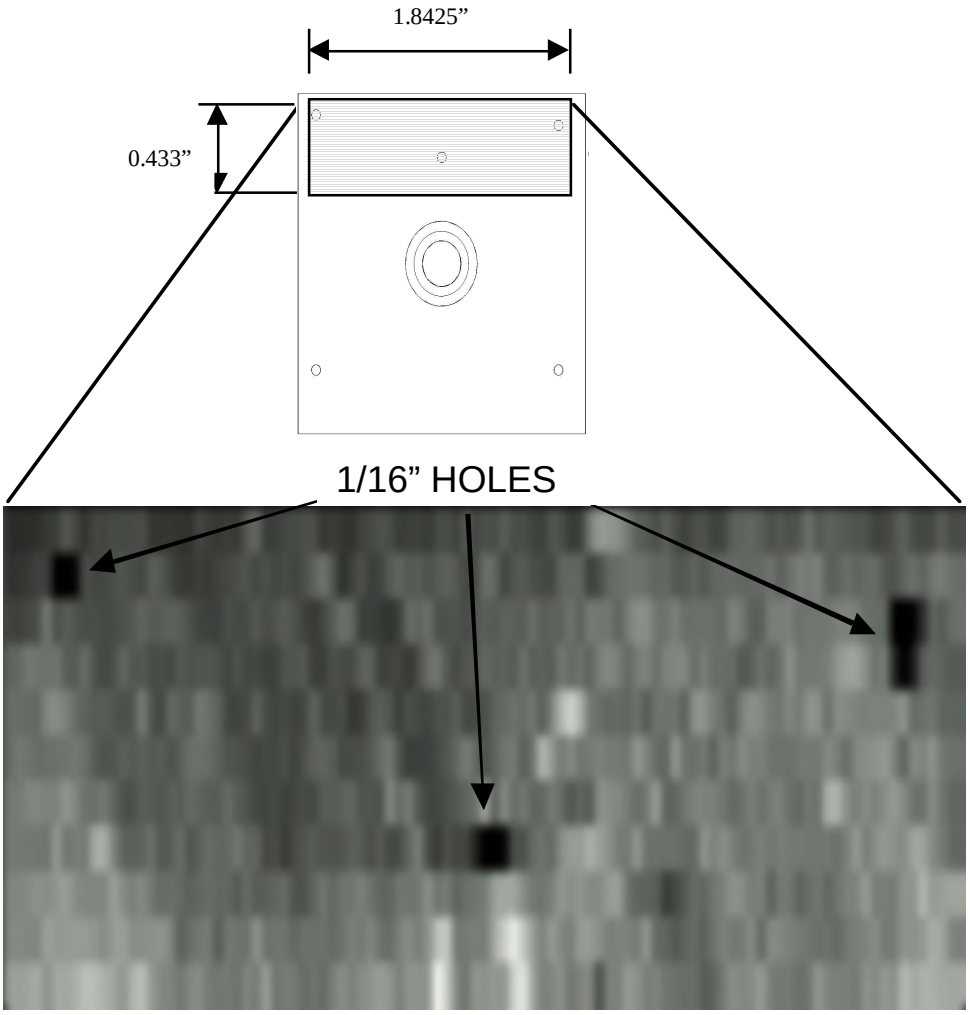

Fig. 2. Low-resolution laser back-scatter scan with robot

(b) <u>Fuel injector plunger</u>

This period we also continued efforts on the laser back-scatter acquisition for the fuel injector plunger. One issue we have is that the data are dependent upon the precision of the centering of the plunger. Shown in Fig. 3 is a scan of the plunger as discussed last period but with the effects of non-precise centering. The data of Fig. 3, a single line scan, consists of 360 points. It takes 6 minutes to complete.

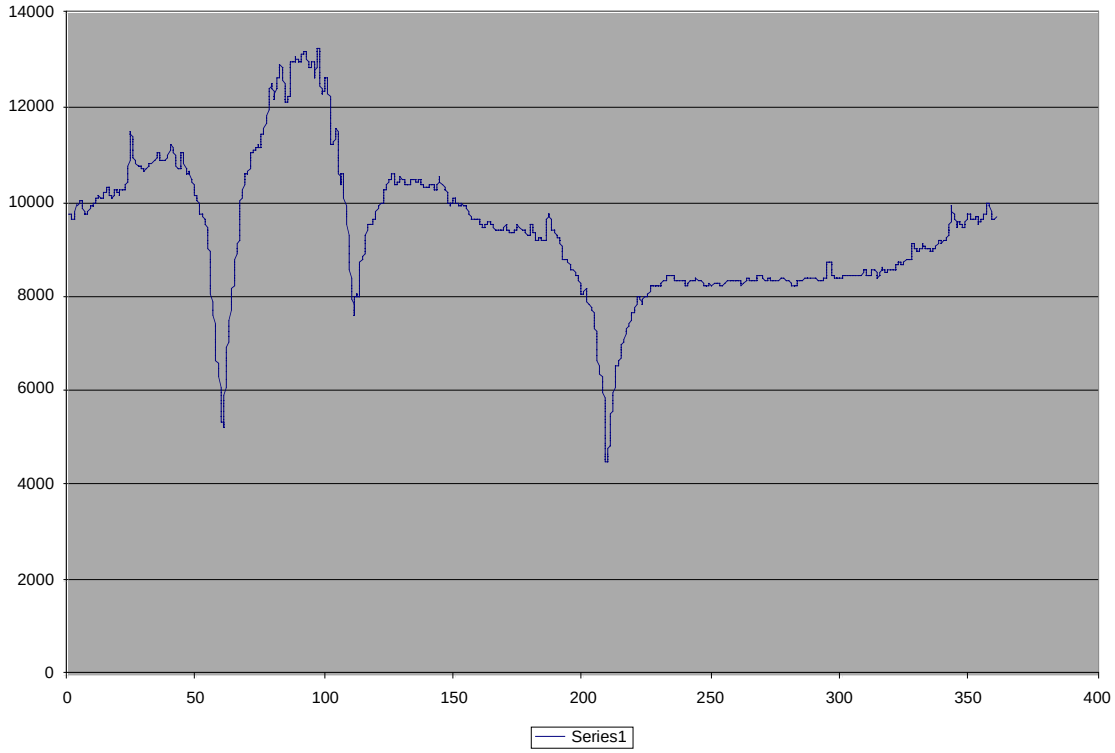

Fig. 3. Scan of plunger with effects of non-precise centering

Meetings, Trips, Communications

A. Meetings

None

B. Trips

None

C. Communications

None

NDE Development for Ceramic Valves for Diesel Engines

J. G. Sun, J. Zhang, W. A. Ellingson
Argonne National Laboratory
and M. J. Andrews
Caterpillar, Inc.

Objective/Scope

Emission reduction in diesel engines designated to burn fuels from several sources has lead to the need to assess ceramic valves to reduce corrosion and emission. The objective of this work is to evaluate several nondestructive evaluation (NDE) methods to detect defect/damage in structural ceramic valves for diesel engines. One primary NDE method to be addressed is elastic optical scattering. The end target is to demonstrate that NDE data can be correlated to material damage as well as used to predict material microstructural and mechanical properties. There are three tasks to be carried out: (1) Characterize subsurface defects and machining damage in flexure-bar specimens of NT551 and SN235 silicon nitrides to be used as valve materials. Laser-scattering studies will be conducted at various wavelengths using a He-Ne laser and a tunable-wavelength solid-state laser to optimize detection sensitivity. NDE studies will be coupled with examination of surface/subsurface microstructure and fracture surface to determine defect/damage depth and fracture origin. NDE data will also be correlated with mechanical properties. (2) Assess and evaluate subsurface damage in ceramic valves to be run in bench test and in a single-cylinder-engine test. All valves will be examined at ANL prior to test, during periodic scheduled shut downs, and at the end of the planned test runs. (3) Evaluate healing of subsurface damage by laser glazing on machined surfaces of GS44 ceramics. ANL will perform laser-scattering characterization on machining surfaces at before and after glazing treatment. NDE data will be correlated with glazing parameters and mechanical properties.

Technical Highlights

Work during this period (July-September 2002) focused on calibrating laser scatter data for a C-crack and on developing laser scatter system for full-valve scans.

1. Elastic Optical Scattering NDE for Machining Damage

During this period we continued effort on calibration of laser scatter data using a NIST standard NBD-200 silicon-nitride specimen with a C-crack. The surface profile of the C-crack is shown in Fig. 1a and its presumed cross-sectional profile is illustrated in Fig. 1b. NBD-200 ceramic has been previously measured to have a 1% light transmission (for He-Ne laser at 633 nm wavelength) at ~100 μm depth, so a significant portion of the subsurface crack should be detected by the laser-scattering system.

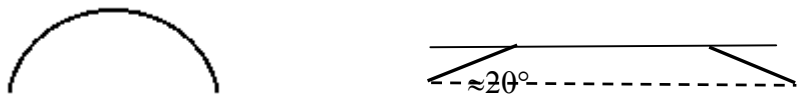

(a) (b)

Fig. 1. (a) Profile of C-crack on surface and (b) cross-sectional profile of C-crack in subsurface.

It is known that many setup parameters of laser scattering system may affect the experimental results, such as stage step size, input optical power, incident angle, focused beam spot size, etc. Three parameters were studied: the stage step size (or pixel size), incident laser beam intensity, and focusing on the specimen (beam spot is larger at unfocused condition). The measured width of the subsurface C-crack is used to evaluate the detection sensitivity at different experimental conditions. This width is determined from the full-width-at-half-maximum (FWHM) of the scatter-intensity profile across the C-crack. Figure 2 shows a scatter image and a corresponding vertical profile from which the FWHM is determined.

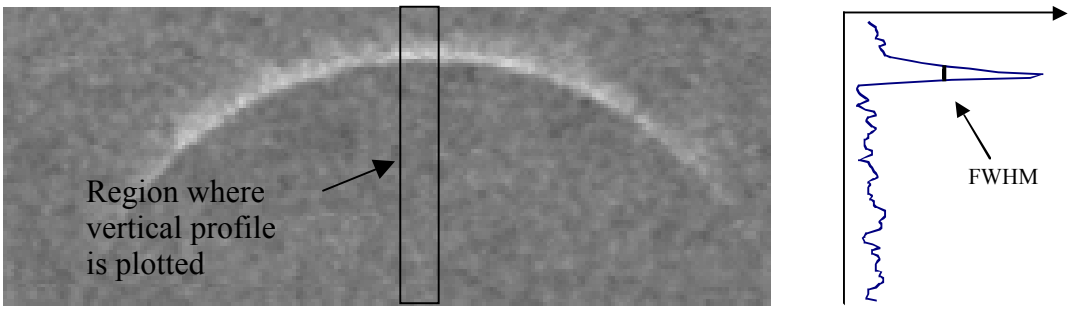

(a) (b)

Fig. 2. (a) A laser-scattering image showing the region for plotting a vertical profile and, (b) laser-scattering profile with the FWHM of C-crack indicated.

Table 1 lists the experimental conditions and correspondingly measured widths of the subsurface C-crack. The laser-scattering sum images from these tests are shown in Fig. 3. It is apparent that the stage step size and the incident beam intensity do not affect the measured width, but focusing has a significant effect on the measured width of the subsurface C-crack. Tests are continued to study the effect of focused laser-beam spot size and/or incident angle on the detection sensitivity of the C-crack.

During this period we received from Caterpillar Inc. three sets of flexure-bar specimens with some treated by laser glazing on the machined surface: 11 transversely ground GS44 bars (5 treated), 6 longitudinally ground GS44 bars (5 treated), and 11 longitudinally ground SN235P bars (5 treated). Figure 4 shows photos of these specimens. They are currently being tested to determine if laser scattering can detect and quantify the laser-glazing effect. Results will be presented in the next report.

Table 1. Experimental condition and measured width of the subsurface C-crack

Step size (μm)	Beam intensity	Focusing	C-crack width (μm)
2	low	focused	56
5	low	focused	45
2	high	focused	48
5	high	focused	50
2	low	unfocused	80
5	low	unfocused	75
2	high	unfocused	88
5	high	unfocused	80

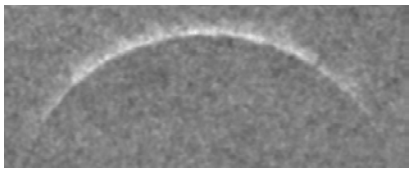
2 μm step size, low intensity, focused

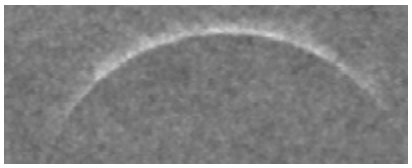
5 μm step size, low intensity, focused

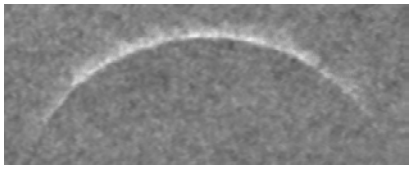
2 μm step size, high intensity, focused

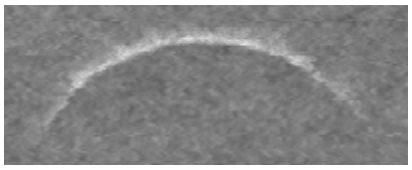
5 μm step size, high intensity, focused

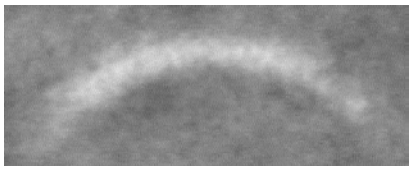
2 μm step size, low intensity, unfocused

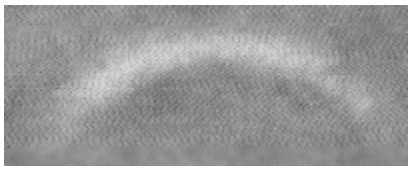
5 μm step size, low intensity, unfocused

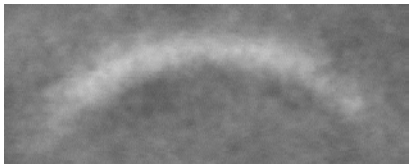
2 μm step size, high intensity, unfocused

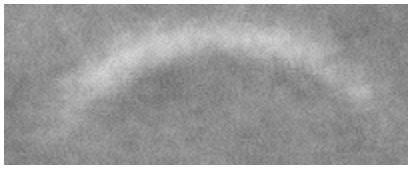
5 μm step size, high intensity, unfocused

Fig. 3. Laser scattering images under different test conditions (image size is 1.0 x 0.4 mm^2).

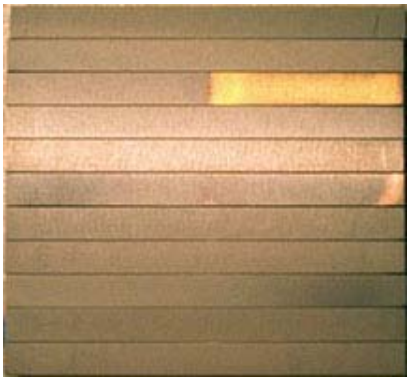

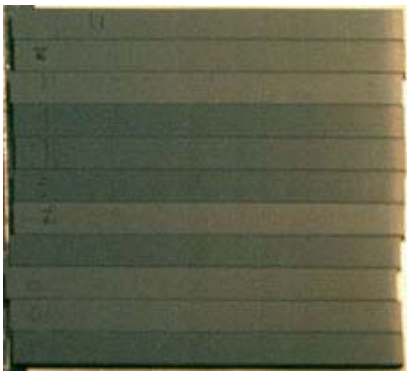

transversely ground GS44 longitudinally ground GS44 longitudinally ground SN235P

Fig. 4. Photos of flexure-bar specimens with 5 in each set treated by laser glazing.

2. Laser-Scattering System Development for Si_3N_4 Valves

During this period we continued development of the laser-scattering system suitable for scanning an entire valve. The schematic diagram of the system was presented in the previous report (Fig. 2 in our April-June 2002 report) and the experimental setup is shown in Fig. 5. This system has been successfully demonstrated for valve scan and preliminary data were obtained. We are currently optimizing the system setup and the scan software. The most critical issue is to maintain a constant-axial-scan step (in the order of 10 μm) of the focused beam on the valve surface by synchronizing the movement of the detection train so that the laser beam is always normally focused on the valve surface. Because there is a long distance between the rotation axis of the detection train and the valve surface, a small step shift (e.g., 10 μm) of the focused beam spot on the valve surface may require a large movement of the detection train (e.g., several centimeters). The system is expected to be fully operational in the next period and results will be reported.

Status of Milestones

Current ANL milestones are on or ahead of schedule.

Communications/Visits/Travel

Dr. M. J. Andrews of Caterpillar Inc. visited ANL on September 26, 2002 to discuss project issues.

Problems Encountered

None this period.

Publications

J.M. Zhang, J.G. Sun, and Z.J. Pei, "Designed Experimental Study on Set-Up Parameters of Laser Scattering System," paper submitted for a presentation at the North American Manufacturing Research Conference, NAMRC Thirty-One, May 20-23, 2003, McMaster University, Hamilton, Ontario, Canada

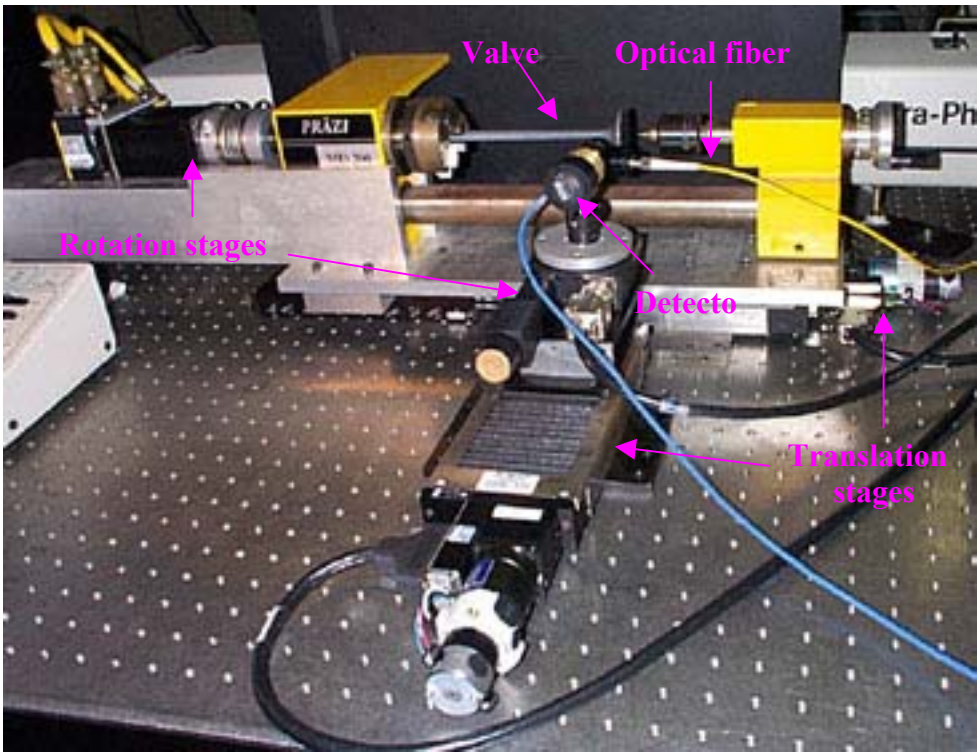

Fig. 5. Photograph of the laser-scattering system for scanning an entire valve.

Processing and Characterization
of Structural and Functional Materials for Heavy Vehicle Applications

J. Sankar and D. Kumar
North Carolina A & T State University

Objective/Scope

Continue to investigate the nanomagnetic materials processed through the Pulsed laser Deposition technique

Task

The report gives an update on the Task "Magnetic Properties Of Self-Assembled Single-Domain Nickel And Iron Nanomagnets" The research work was carried out in collaboration with J. Narayan, A. Tiwari, H. Zhou, C. Jin, and A.V. Kvit of Center for Advanced Materials and Smart Structures, Department of Materials Science and Engineering North Carolina State University, Raleigh, NC 27695; and S.J. Pennycook and A. Lupini of Solid State Division, Oak Ridge National Laboratory, Oak Ridge, TN 37831.

Technical Highlights

I. INTRODUCTION

Nanoscale magnetism currently provides a wealth of scientific interest and of potential applications.[1-3] When the size of magnetic particles is reduced to a few tens of nanometers, they exhibit a number of outstanding physical properties such as giant magnetoresistance, superparamagnetism, large coercivities, high Curie temperature, and low saturation magnetization as compared to the corresponding bulk values. The coercivity exhibits a strong dependence on the size of magnetic materials. Typically, the coercivity is zero up to a critical size and then it goes through a maximum. Absence of coercivity and remanence is associated with superparamagnetic behavior. Up to the coercivity maximum, nanocrystals behave as single domains and above this size there is a multi-domain behavior where coercivity decreases as the size increases. Therefore, the synthesis of magnetic systems with characteristic nanoscale dimension has attracted a lot of research attention. Inert gas condensation, sputtering, mechanical attrition, aerosol, ball milling, etc. are some of the common methods adopted to synthesize ultafine magnetic particles.[4-5] While most of these methods have met with considerable success, producing heterogeneous magnetic materials in a controlled compositional, structural and reproducible manner is still not satisfactory. It is in this context that we have developed a laser-assisted method to uniquely produce nanocrystalline materials in an amorphous insulating matrix. The method is generic in nature and can be applied to the synthesis of magnetic, optical, mechanical, electroluminescent, etc. fine particles. In the present investigation, Ni and Fe nanocrystallites in the single domain regime are embedded into nonmagnetic (amorphous and crystalline α- Al_2O_3) matrix. By controlling the size of the nanocrystalline magnetic materials, we can tune the magnetic properties from superparamagnetic to ferromagnetic. In addition, large volume of coercivity and remanence can be achieved by optimizing the size of nanocrystallites in the single domain regime. The details of size distribution, shape and morphology of nanocrystallites are studied by cross-section transmission electron microscopy (TEM), and these

results are correlated with magnetic measurements using a superconducting quantum interference device magnetometer (SQUID).

II. EXPERIMENTAL

Nanocrystalline iron and nickel particles were embedded separately in alumina matrix by laser ablation. For this purpose, a multitarget pulsed laser deposition system was used where iron or nickel and alumina targets are alternatively ablated. The depositions were carried out on silicon substrates in a high vacuum environment (~5 X 10^{-7} Torr). The substrate temperature was approximately 500 ^{O}C. The energy density and repetition rate of the laser beam used were 2J/cm^2 and 10 Hz. The size of the Fe and Ni particles were controlled by carefully selecting the deposition time of magnetic materials and insulating matrix and the deposition temperatures. In the present work, the deposition times were 40-60 sec for magnetic materials and 120 sec for insulating materials. The numbers of alternating layers (Fe-Al_2O_3 and Ni- Al_2O_3) were chosen to be five so that we get enough signal during magnetic measurements. The size distribution of Fe and Ni particles and the crystalline quality of both the matrix and magnetic particles were investigated by cross-sectional high-resolution transmission electron microscopy (HRTEM). The magnetic properties of Fe-Al_2O_3 and Ni-Al_2O_3 systems were measured using superconducting quantum interference device (SQUID) magnetometer.

III. RESULTS AND DISCUSSION

In magnetic studies on fine particles the single property of most interest is the coercivity (H_c), for two reasons: (i) it must be high to be of any value for permanent-magnet applications, and (ii) it is a quantity which come quite naturally out of theoretical calculations of the hysteresis loop. Shown in Fig. 1 are the M-H loops at 300 K for Fe-Al_2O_3 samples having three different Fe particles sizes. The particle size of Fe in these samples, named sample #1, sample #2, and sample #3, are found to be 4.5, 7 and 9 nm, respectively from TEM studies. The size of Fe nanocrystals was determined by the amount of laser deposition and the substrate temperature. The times of Fe deposition were 20, 40, and 60 sec in sample 1, 2, and 3, respectively. The time of Al_2O_3 deposition was kept the same (120 sec) in each sample.

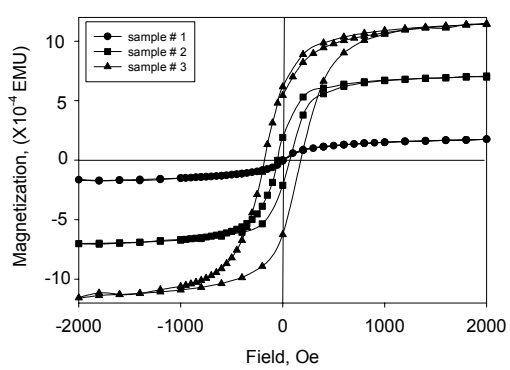

Fig.1. M-H plots for three Fe-Al_2O_3 samples at 300 K

As seen in Fig.1, the coercivity decreases from 100 to 50 Oe as the particle size decreases from 9 nm to 7 nm and finally the sample turns superparamagnetic when the Fe particle size becomes 5 nm (sample # 1). These values of H_c may be attributed to the presence of iron particles in the form of single domains where magnetization reversal could take place only by rotation of saturation magnetization (M_s) vector in accordance with the Stoner and Wohlfarth model.

Shown in Fig. 2 is the variation of zero field magnetization (M) as a function of temperature (T) in the range of 10-350 K for Fe- Al_2O_3 and Ni- Al_2O_3 samples. The field applied during the magnetization measurements of both the samples was 500 Gauss. According to the M-T curve for Ni- Al_2O_3 sample, its magnetization rises as the temperature is lowered and reaches a peak ~70 K. Beyond this temperature, the magnetization decreases with the decrease in temperature. This temperature at which M-T peak occurs is known as blocking temperature (T_B), which is defined as a temperature below which magnetization is stable. Obviously, such a peak in missing in the M-T curve from Fe- Al_2O_3 sample, which might be taken to suggest that the T_B of Fe-Al_2O_3 sample is higher than 350 K.

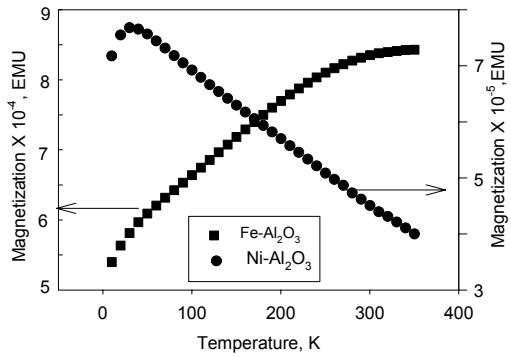

Fig.2. Variation of zero field magnetization as a function of temperature in the range of 10-350 K for Fe- Al_2O_3 (squares; sample #3) and Ni- Al_2O_3 (circles) samples.

IV. CONCLUSIONS

In summary, we have demonstrated that single-domain nanocrystalline magnetic particles can be distributed uniformly in an insulating matrix in a controlled manner by a pulsed laser deposition technique. Fabrication of heterogeneous fine magnetic materials in a controlled compositional, structural and reproducible manner might open a way of developing artificially nanostructured materials for fundamental studies in nanomagnetism and for applications such as patterned magnetic recording media.

References

1. C. Stamm, F. Marty, A. Vaterlaus, V. Weich, S. Egger, U. Maier, U. Ramsperger, H. Fuhrmann, and D. Pescia, Science **282**, 449 (1998).
2. E. Gu, E. Ahmad, S.J. Gray, C. Daboo, J.A.C. Bland, L.M. Brown, and J.C. Chapman, Phys. Rev. Lett. **78**, 1158 (1997).
3. O. Fruchart, J.-P. Nozieres, W. Wernsdorfer, D. Givord, F. Rousseaus, and D. Decanini, Phys. Rev. Lett. **82**, 1305, (1999).
4. L. Lu, M.L. Sui, and L. Lu, Science **287**, 1463 (2000).
5. G.A. Prinz, Science **282**, 1660 (1998)

Status of Milestones

On Schedule

Communications/Visitors/Travel

None

Problems Encountered
None

Publications

1. Kumar D., Zhou H., Nath T.K., Kvit A.V., Narayan J.,"Self-assembled Epitaxial and Polycrystalline Magnetic Nickel Nanocrystallites,"Applied Physics Letters, 79(17), Oct.22, 2001, pp.2817-2819
2. D. Kumar, J. Sankar, J. Narayan, H. Zhau, A. V. Kvit, and T. K. Nath, "Magnetic and Mechanical Properties of Metal-Ceramic Thin Film Composites," 2001 ASME International Mechanical engineering Congress and Exposition, New York, "Processing and Understanding of Structural and Electronic Ceramic Materials"(Full Peer Reviewed Proceeding), Volume MD95.
3. D. Kumar, J. Sankar, J.Narayan, A.K.Sharma, A. Kvit and Jin, "Tunable Mechanical and Magnetic Properties in Metal Ceramic Composite Smart Films," The 18th Biannial ASME Conference on Mechanical Vibration and Noise, Pittsburg, USA, Sept 9-13, 2001.
4. D. Kumar, J. Sankar, Narayan, A. Tiwari, H. Zhou, C. Jin, A.V. Kvit, S.J. Pennycook and A. Lupini, "Magnetic properties of self-assembled single-domain nickel and iron nanomagnets," (Invited), ICCE-9, San Diego, July 1-6, 2002
5. D. Kumar, J. Narayan, A.K. Sharma, A. Kvit, C. Jin, and J. Sankar,"Magnetic Properties of Iron and Nickel Particle of Nanometer Dimension," Journal of Solid State Electronics, in press.

Life Prediction of Diesel Engine Components

H. T. Lin, T. P. Kirkland, and M. K. Ferber
Oak Ridge National Laboratory
and M. J. Andrews
Caterpillar, Inc.

Objective/Scope

The valid prediction of mechanical reliability and service life is a prerequisite for the successful implementation of structural ceramics and advanced intermetallic alloys as internal combustion engine components. There are three primary goals of this research project which contribute toward that implementation: the generation of mechanical engineering data from ambient to high temperatures of candidate structural ceramics and intermetallic alloys; the microstructural characterization of failure phenomena in these ceramics and alloys and components fabricated from them; and the application and verification of probabilistic life prediction methods using diesel engine components as test cases. For all three stages, results are provided to both the material suppliers and component end-users.

The systematic study of candidate structural ceramics (primarily silicon nitride) for internal combustion engine components is undertaken as a function of temperature (< 900°C), environment, time, and machining conditions. Properties such as strength and fatigue will be characterized via flexure and rotary bend testing.

The second goal of the program is to characterize the evolution and role of damage mechanisms, and changes in microstructure linked to the ceramic's mechanical performance, at representative engine component service conditions. These will be examined using several analytical techniques including optical and scanning electron microscopy. Specifically, several microstructural aspects of failure will be characterized:

(1) strength-limiting flaw-type identification;
(2) edge, surface, and volume effects on strength and fatigue size-scaling;
(3) changes in failure mechanism as a function of temperature;
(4) the nature of slow crack growth; and
(5) what role residual stresses may have in these processes.

Lastly, numerical probabilistic models (i.e., life prediction codes) will be used in conjunction with the generated strength and fatigue data to predict the failure probability and reliability of complex-shaped components subjected to mechanical loading, such as a silicon nitride diesel engine valve. The predicted results will then be compared to actual component performance measured experimentally or from field service data. As a consequence of these efforts, the data generated in this program will not only provide a critically needed base for component utilization in internal combustion engines, but will also facilitate the maturation of candidate ceramic materials and a design algorithm for ceramic components subjected to mechanical loading in general.

Technical Highlights

Studies of mechanical properties in tension for TiAl intermetallic alloy after oil immersion test at temperatures ranging from 20°C to 800°C in air were completed during this reporting period. The oil immersion test was carried out at 750°C for 48 h in air. Five specimens were tested in tension at each temperature. The TiAl alloys have been considered as one of the potential candidates for exhaust valve applications. The purpose of this study is to develop database necessary for probabilistic design and life prediction, and also to understand the effect of oil ash environment on the mechanical properties of TiAl alloy. The test result for the as-received materials, obtained from Caterpillar, was used as a reference for comparison. Results of ultimate tensile strength (MTS) showed that the exposed TiAl specimens exhibited 8-12% decrease in UTS at temperatures ≤ 600°C, as shown in Fig. 1. The measured UTS values for both as-received and exposed specimens became similar at temperatures of 700 and 800°C. The decrease in UTS at temperatures below 600°C could arise from the development of a subsurface damage zone due to the oil ash exposure. The surface healing effect at temperature ≥ 700°C in an oxidizing environment could attribute to the observed increase in MTS for the exposed samples. A detailed analysis of data obtained will be carried out in order to compare the values of yield strength, Young's modulus, and elongation between the as-received and exposed samples.

In addition, preliminary SEM analysis showed that the surface of exposed TiAl sample exhibited a loss oxide scale formed due to the oxidation of oil ash powder, as shown in Fig. 2. The original machining marks were still visible after exposure (Fig. 2). The oxide scale contained a composition of Ti, Al, V, Zn, P, S, and Ca. Note the Zn, P, S, and Ca were the additives typically employed in the engine oil. Polished cross section of tensile specimen tested at room temperature will be conducted to characterize the extent of corrosion and, thus, the depth of subsurface damage zone due to the exposure.

Initial bench rig tests on Norton NT551 silicon nitride exhaust valve resulted in substantial wear in the metallic seat insert due to the angle mismatch. The new seat inserts were redesigned and machined to ensure a proper alignment and minimum bending stress. After the employment of newly deigned seat insert, the re-test of NT551 valves have been very successful, and little wear has been observed. The NT551 vales after bench rig test at Caterpillar will be forwarded to ORNL for retained strength evaluation at room temperature. The strength evaluation will provide an understanding on the effect of test cycles on the mechanical reliability of silicon nitride exhaust valves.

Status of Milestones

Milestone: "Complete testing and analysis of prototype silicon nitride valves after bench rig testing" was not completed due to the angle mismatch between NT551 valves and metallic seat insert. The new completion date set for the milestone is April 30, 2003.

Communications / Visitors / Travel

Update of the status of initial bench test on Norton NT551 exhaust valves was held with M. J. Andrews at Caterpillar.

Communication with Juses Chapa-Cabrera at Caterpillar on the tensile test results of TiAl alloy.

Problems Encountered
None.

Publications
None.

References
[1] H. T. Lin, T. P. Kirkland, M. K. Ferber, and M. J. Andrews, "Life Prediction of Diesel Engine Components," Heavy Vehicle Propulsion System Materials Program Bimonthly Technical Progress Report to DOE Office of Transportation Technologies, April – June 2002.

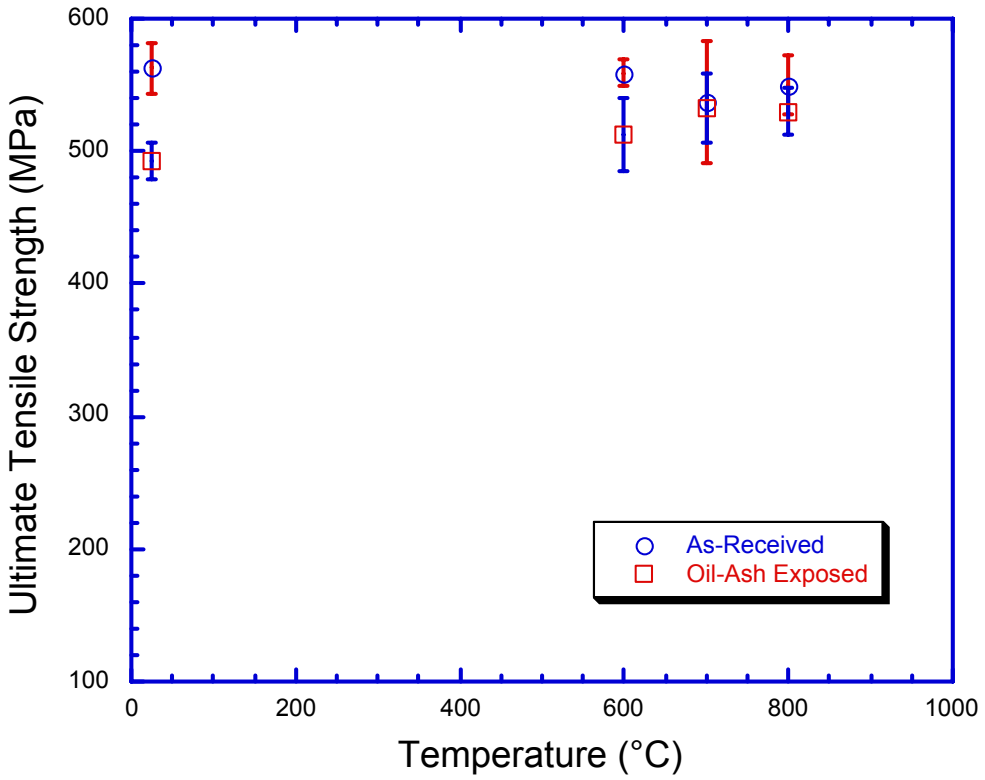

Figure 1. Comparison of ultimate tensile strength between TiAl alloy in as-received condition and after oil-immersion test.

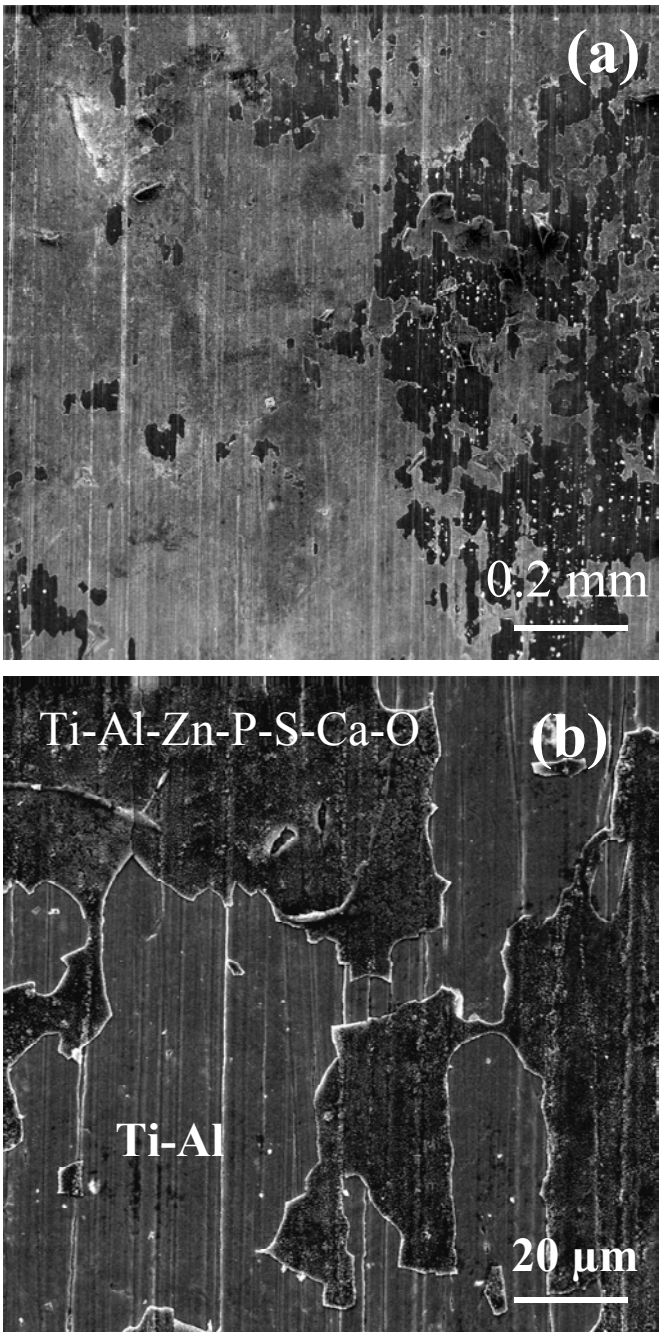

Figure 2. SEM micrograph of surface features for TiAl alloy after exposure to an oil ash environment.

Durability of Diesel Engine Component Materials

Peter J. Blau and Ronald D. Ott
Oak Ridge National Laboratory

John Truhan
University of Tennessee, Knoxville, TN

Jun Qu
ORISE Post-Doctoral Fellow

Objective/Scope

The objective of this effort is to enable the development of more durable, low-friction moving parts in diesel engines for heavy vehicle propulsion systems by conducting friction, lubrication, and wear analyses of advanced materials, surface treatments, and coatings. The scope of materials and coatings is broad and includes any metallic alloy, intermetallic compound, ceramic, or composite material which is likely to be best-suited for the given application. Parts of current interest include scuffing-critical components, like fuel injector plungers and EGR waste gate components. Bench-scale simulations of the rubbing conditions in diesel engine environments are used to study the accumulation of surface damage, and to correlate this behavior with the properties and compositions of the surface species. The effects of mechanical, thermal, and chemical factors on scuffing and reciprocating sliding wear are being determined, as are methods to detect the onset of damage and portray its progression. Results will be used to refine material selection strategies and suggest materials for durability-critical engine components.

Technical Highlights

Fuel Injector Plunger Scuffing. In order to meet stricter emissions requirements, advanced heavy-duty fuel injection systems will be required to operate at higher pressures, temperatures and in fuels that have poorer lubricity. Scuffing, as a mode of failure, severely limits injector life and new materials and processes are required to resist scuffing in these more stringent operating conditions. Consequently, there is a need to test the ability of candidate fuel systems materials to resist the on-set of scuffing in fuel-lubricated environments. ORNL is approaching this need by developing testing methodology to study scuffing behavior of traditional and promising new materials for use in injector plungers. Since fuels with low sulfur are being introduced, material compatibility in such environments is also of interest.

A 'pin-on-twin' testing geometry has been developed for use on the Plint and Partners TE/77 High-Frequency Friction Machine. An upper cylindrical pin is oriented with its axis perpendicular to that of two lower pins of equal diameter, mounted in parallel to each other. The upper pin moves back and forth under load on the twin pins to produce elongated wear scars on the lower specimens and twin notches on the upper one. All three pins are 9.5 mm in diameter.

Cylinders of annealed AISI 52100 high-Cr bearing steel were tested in three states of lubrication: (1) no lubricant (dry), (2) lubricated with Jet A aviation fuel, and (3) lubricated with on-highway #2 diesel fuel. Aviation fuel was selected to represent the next generation of low-sulfur diesel fuels. The cylindrical pins were polished with 600 grit SiC paper to provide a consistent surface

finish, averaging 0.08 μm in arithmetic average roughness (R_a). The reciprocating frequency and stroke length were set to 10 Hz and 10 mm, respectively. Loads and test times were varied depending on the objective of each test.

Effect of the different lubricants on friction and wear

Three tests were conducted under a load of 100 N for 300 seconds under dry, Jet A, and diesel fuel-lubricated conditions. The wear scars are shown in Fig. 1. Figure 1(a) is a low magnification optical view of the three wear scars labeled (b), (c) and (d). These scars are shown in corresponding SEM images to the right. The scar width, roughness, and the coefficient of friction of the three tests are listed in Table 1. In the dry test, the wear scar was huge and rough, and the original surface was severely damaged (Fig. 1(b)). The coefficient of friction was also fairly high, at least 0.9. Although Jet A and diesel fuels are not considered effective lubricants, there was a significant improvement in both the degree of surface damage and material loss compared to the dry sliding condition. The surfaces of the lubricated tests were only slightly scuffed, with a small amount of material removed and transferred between the worn surfaces, as shown in Fig. 1(c) and (d). The coefficient of friction was much lower as well. Comparing the two lubricated tests, more severe wear was observed in the test lubricated by Jet A fuel because of its poorer lubricity.

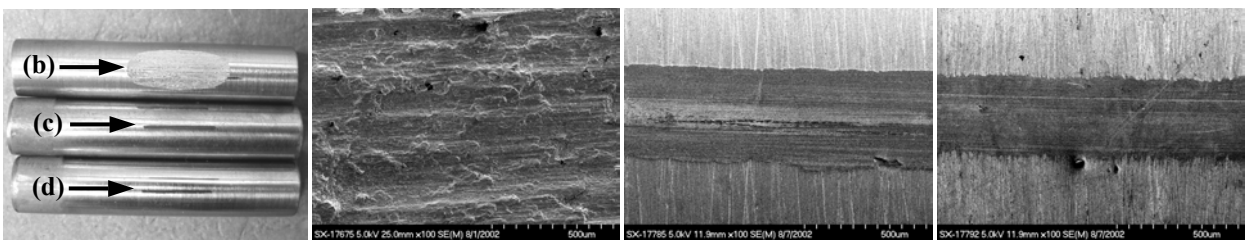

(a) (b) (c) (d)

Figure 1. Effect of the lubricants. (a) Bottom pins tested dry, lubricated by Jet A and Diesel fuels. (b) The wear scar of dry test. (c) The wear scar of Jet A test. (d) The wear scar of Diesel test.

Table 1. Results of tests under dry and lubricated conditions.

Quantity	Dry	Jet A	Diesel
Coefficient of friction	0.9	0.25	0.15
Wear scar width (mm)	6.5	0.52	0.43
Wear scar roughness (μm)	6.95	0.18	0.16

Detecting the Onset of Scuffing

Two sets of lubricated tests, hereafter called Experiments I and II, were conducted using both Jet A and #2 diesel fuels. In the Experiment I, five tests were run at different loads, 10, 20, 50, 75, and 100 N, for 300 seconds to study the effects of load. The friction force, as shown in Fig. 2, was monitored to trace the onset of scuffing. Three stages have been identified on the friction force traces based on low, transition, and high friction levels. In the Experiment II, tests were terminated in the low friction (30 s), transition (90 s for Jet A and 120 s for Diesel), and high friction (300 s) regimes to investigate the surface morphology of the three wear stages. A fixed load 100 N was applied.

The transition of the friction force was found to give a reliable real-time determination of the onset of scuffing as verified by microscopy of the wear scar. The SEM micrographs of the wear scars of the interrupt tests are shown in Fig. 3. In the low friction stage, as shown in Fig. 3(a), only mild wear occurred and somehow smoothened the original surface, so this stage is named the "polishing" stage. Figure 3(b) shows the wear scar at the transition stage. The worn surface is mostly smooth, except for two longitudinal grooves extending all way through, indicating the start of scuffing. The wear scar in the high friction stage (Fig. 3(c)) shows relatively severe wear features with material removal and transfer, generally characteristic of scuffing.

The wear scar width and surface roughness of the three wear stages, polishing, transition, and scuffing, have also been measured and analyzed. The results showed the dependency of wear on the lubricant, load, and time, but did not accurately detect the onset of scuffing.

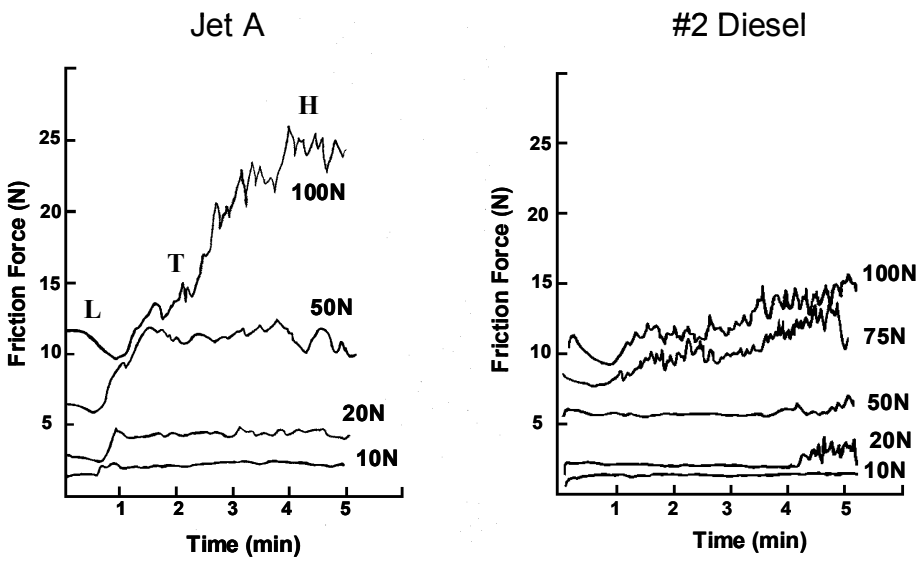

Figure 2. The friction force traces for different lubricants, loads, and time.

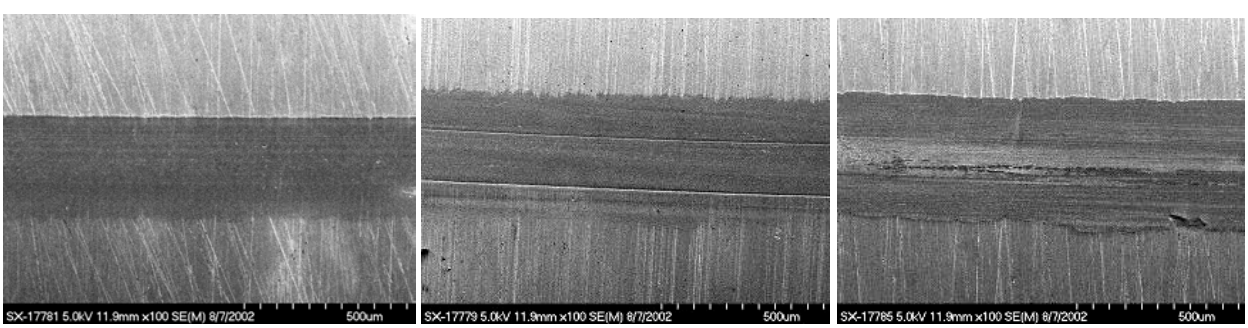

(a) (b) (c)

Figure 3. The wear scars at three wear stages: (a) polishing stage, (b) transition stage, (c) scuffing stage.

Future Plans

1. Continue metallurgical studies of scuff-tested specimens, including the use of the scanning acoustic microscope where appropriate.

2. Apply the pin-on-twin test, under Jet A and diesel fuel-lubricated conditions, to hardened 52100 steel and zirconia, which are typical fuel injector plunger materials in diesel engines.
3. Begin to investigate other potential plunger materials and coatings.
4. Evaluate the use of an alternative contact configuration, flat-on-flat, as a better simulation of the stresses and types of damage seen in actual plunger components.

Travel

None.

Status of FY 2002 Milestones

1) Complete design and construction of fixtures to adapt existing ORNL friction and wear testing machine for fuel injector plunger materials. (December 15, 2001 – completed.)

2) Complete elevated temperature scuffing tests of leading candidate materials. Submit report. (March 31, 2002 - completed)

3) Complete tests of candidate ceramic materials and cermets for fuel injector applications. Submit report. (September 30, 2002 – the pin-on-twin test configuration under Jet A and Diesel fuel-lubricated conditions are established and systematic tests have been conducted on AISI 52100 steel to detect onset of scuffing. Tests on other candidate materials and new configuration will be conducted in next quarter.)

Publications

J. Qu, J. Truhan, P.J. Blau, and R. Ott, "The Development of a Scuffing Test to Evaluate Materials for Heavy Duty Fuel Injectors, Part 1. Pin-on-Twin Configuration," for submission to *Lubrication Engineering*.

Laser Surface Texturing Of Lubricated Ceramic Parts

Peter J. Blau and Jun Qu
Oak Ridge National Laboratory

Objective/Scope

The objective of this effort is to evaluate the frictional benefits of laser dimple patterns on the lubrication of ceramic surfaces. This project is part of a joint Argonne National Laboratory/ ORNL analysis of the benefits of a laser surface texturing (LST) process developed by Prof. Itzhak Etsion, Surface Technologies, Ltd., Israel. That process uses a computer-controlled laser to produce a pattern of shallow, rounded dimples on bearing surfaces. Based on calculations, preliminary tests, and limited field trials, the developer claims that LST enhances the ability of a lubricated surface to establish a load-bearing hydrodynamic film that decreases friction relative to a non-dimpled surface. The ORNL portion of this joint effort is focused on two aspects of LST: (1) conducting reciprocating tests of ceramic surfaces using lubricating fluids with various viscosities, and (2) determining the microstructural changes that are associated with the LST process.

Technical Highlights

Acoustic microscopy of LST damage in TTZ. In the last report, scanning electron microscope images of laser-induced damage produced in TTZ were described. The recent upgrade of the scanning acoustic microscope at ORNL has enabled additional studies of the dimple structure below the surface. Figure 1 is a high-frequency scanning acoustic image of a crater in LST TTZ.

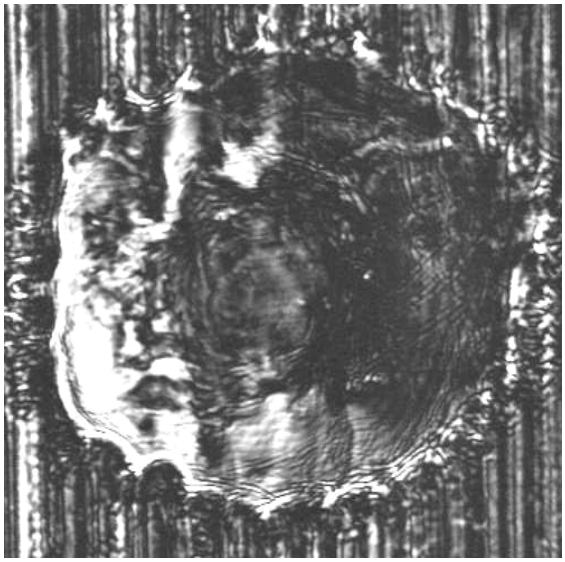

Figure 1. Scanning acoustic image of a crater showing both interference fringes and additional details in the sub-surface structure. Approximate field size 150 μm x 150 μm. (frequency 1.0 GHz; defocus depth Z = - 6 μm)

Features corresponding to subsurface residual grinding damage, fringes due to surface topography, and other features associated with subsurface micro-cracks are visible in this image.

The sources of contrast and the interpretation of such images are described in more detail the September 2002 project milestone report that has been provided separately to DOE (see below under "Publications").

Further studies of subsurface damage are underway. These involve cross-sectioning and polishing of the dimple craters for optical and acoustic microscopy.

Lubricated sliding tests of SiC specimens. Previous work revealed the sensitivity of reciprocating friction results to the alignment of the contact surfaces. Therefore, a different test apparatus and set of holders was prepared to address this issue for testing LST SiC specimens. Tests were performed on a custom-built reciprocating tribometer in which there was more control over specimen alignment than in the Plint and Partners TE-77 machine used in earlier studies of LST TTZ. Tests of laser-textured and as-ground flat-sided cylinders were performed at 5 N normal force and 2 Hz reciprocating rate in both mineral oil and fresh Valvoline diesel engine oil ('Cummins Blue'). Oscillating motion, friction force data were sampled on a computer data acquisition system, rectified, and averaged to provide kinetic friction coefficients for periodic intervals during the 3500 cycle tests. Results are summarized in Figure 2.

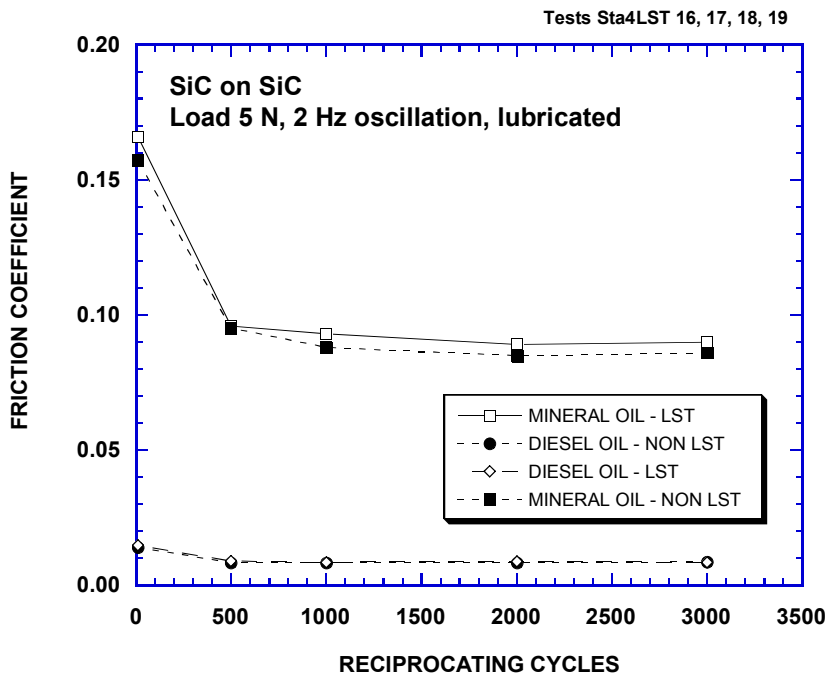

Figure 2. Friction coefficient versus number of cycles for LST and non-treated SiC cylinders on SiC flat tiles sliding in mineral oil and diesel oil.

As the data in Fig. 2 show, there was no detectable difference in the friction for laser-textured and non-laser-textured SiC under these test conditions. The trends in friction coefficient and the repeatability of experimental results for each lubricant type was excellent despite the differences

in localized surface topography. These data suggest that the conditions were not sufficient to detect the effects of LST on SiC.

Results for tests and analyses of LST SiC mechanical face seals showed distinct advantages of such texturing [I. Etsion, Y. Kligerman and G. Halperin, "Analytical and Experimental Investigation of Laser-Textured Mechanical Seal Faces," *Tribology Transactions*, Vol. 42, No. 3, July 1999, pp. 511-516.] The current geometry was an attempt to determine whether similar advantages could be measured in reciprocating, narrow contacts. Current results were discussed with Prof. Etsion and it was suggested that higher speeds and better running-in of the surfaces might be advisable. These suggestions are being considered in designing further tests of LST SiC.

Future Plans

(1) Continue friction tests on LST and non-LST SiC materials at higher speeds.

(2) Continue to characterize LST damage to both TTZ and SiC.

Travel

None.

Status of FY 2002 Milestones

1) Complete design and construction of fixtures to adapt existing ORNL friction and wear testing machine for cylinder on flat testing. (January 31, 2001 – completed.)

2) Complete baseline friction tests of as-ground ceramics in three liquid lubricants. (May 31, 2002 - completed)

3) Complete friction tests of laser surface textured ceramics in three lubricants. Submit report. (July 31, 2002 – delayed in order to include additional results on SiC)

4) Characterize laser dimpling effects on the microstructures of selected ceramics. Submit report. (September 30, 2002 – completed.)

Publications

P. J. Blau and J. Qu (2002) "Characterization of Laser Surface Dimpling Effects on Transformation-Toughened Zirconia," project milestone report submitted to DOE, FreedomCAR and Vehicle Technologies Program, September 30, 2002.

Implementing Agreement For A Programme Of Research And Development On Advanced Materials For Transportation Applications

M. K. Ferber
Oak Ridge National Laboratory

Objective/Scope

The International Energy Agency (IEA) was formed via an international treaty of oil consuming countries in response to the energy crisis of the 1970s. A major objective of the IEA is to promote secure energy supplies on reasonable and equitable terms. The governing board of the IEA, which is composed of energy officials from each member country, regularly reviews the world energy situation. To facilitate this activity, each member country provides energy experts who serve temporary staff assignments at IEA headquarters. These staff or secretariat support the governing board by collecting and analyzing energy data, making projections in energy usage, and undertaking studies on specialized energy topics. The governing board is also assisted by several standing groups, one being the committee on energy research and technology (CERT), which encourages international cooperation on energy technology. Implementing agreements (IAs) are the legal instruments used to define the general scope of the collaborative projects. There are currently 40 active implementing agreements covering research topics such as advanced fuel cells, coal combustion science, district heating and cooling, enhanced oil recovery, fluidised bed conversion, fusion materials, solar heating and cooling, pulp and paper, hydropower, heat pumping technologies, hybrid and electric vehicles, high temperature super conductivity, wind turbines, and high temperature materials. A complete listing can be found at the IEA website, www.iea.org.

This progress report summarizes recent activities in the implementing agreement entitled, "Implementing Agreement For A Programme Of Research And Development On Advanced Materials For Transportation Applications." This implementing agreement currently consists of one active annex entitled," Annex II: Co-Operative Program on Ceramics for Advanced Engines and Other Conservation Applications." The motivation for this IA is the development of new and improved ceramic materials, brittle material design methods, and life prediction methodology. The objective of Annex II is coordinated R&D on advanced ceramics leading to standardized methods for testing and characterization.

The Executive Committee for the IA on Advanced Materials is also exploring the possibility of adding new efforts (Annex III and Annex IV). Annex III focuses on the characterization of contact damage (fatigue) while Annex IV deals with materials for hydrogen storage.

Technical Highlights

The annual Executive Committee meeting was held this reporting period. This meeting was held in conjunction with the CIMTEC 2002 Meeting on Tuesday, July 16 from 3:00 to 6:00 p.m. in Florence, Italy. The main objectives of this meeting were to review the current status of our IA and to discuss future activities. The attendees included Sidney Diamond (Department of Energy (DOE) Office of FreedomCAR and Vehicle Technologies, United States and Executive Committee Chairman), Rolf Wäsche (Bundesanstalt für Materialforschung und-Prüfung/German Executive Committee Member), Mr. Katsuji Otsubo (New Energy and Industrial Technology

Development Organization/Japanese Executive Committee Member), Shinya Tamura (New Energy and Industrial Technology Development Organization/Japanese Alternate Executive Committee Member), Mineo Mizuno (Japan Fine Ceramics Center/Japanese Technical Leader of Subtask 11), and Said Jahanmir (National Institute of Standards and Technology/Alternate Working Group Coordinator of Subtask 1-Annex III). The major achievements of the meeting were (1) the addition of two new subtasks to the existing Annex II and (2) the creation of a new Annex III focusing on the assessment of contact damage in advanced materials.

Status of Milestones

All milestones are on track.

Communications/Visits/Travel

None.

Publications

None.

References

None

Standards For Reliability Testing Of Heavy Vehicle Propulsion Materials

Said Jahanmir and William Luecke
National Institute of Standards and Technology

Objective/Scope

The objective of this project is to develop international standard test methods for assessing the reliability of ceramic components used in diesel engines and other heavy vehicle propulsion systems. Advanced ceramics such as silicon nitride offer a unique combination of properties that include light weight, excellent high-temperature strength, and resistance to wear and corrosion. These properties make them particularly attractive for diesel engines, where their use as key engine components will allow the higher operating temperatures that lead to higher thermal efficiencies and environmentally cleaner propulsion systems. Reliability and cost-effectiveness are critical issues in implementing ceramics in the valve train of diesel engines. Ceramic valve train components are subjected to demanding conditions that include high contact loading, elevated temperatures, and corrosive environments. To ensure a reliable service life, standard test methods are needed to evaluate the performance of potential ceramics in highly loaded rolling and sliding contacts. This project will develop test methods for evaluating the contact damage behavior of ceramics under rolling and sliding conditions that simulate the cam roller followers, valves and valve seats. In support of this goal we will pursue four research thrusts: 1) fundamental issues in the relation between ceramic microstructure and performance reliability, 2) basic mechanisms that lead to formation and propagation of contact damage and the effect on reliability of residual stresses developed during machining and by contact, 3) effect of machining damage on contact reliability as well as the interactions between machining and contact damage that may lead to premature failure, 4) development of international standards for assessing contact damage.

Technical Highlights

IEA Annex III Activities

Activities under the IEA Annex III, approved by the Executive Committee in July, include various forms of contact damage testing and evaluations relevant to the implementation of advanced materials in engines. These include rolling contact fatigue, sliding and fretting wear, fretting fatigue, and other mechanical performance phenomena that control the reliability of contacts in advanced engines. Materials under consideration may include structural ceramics, composites, and nanostructured friction/wear coatings.

Two Subtasks were initiated under this new annex. The objective of Subtask 1 (Technical Information Exchange) is to achieve a balanced exchange of technical information between the participating countries on contact reliability of ceramics and coatings. The Subtask activities may include (a) Exchange of reports, studies, and software packages as agreed upon in advance by the Executive Committee on an annual basis; (b) Joint technical meetings; (c) Reciprocal invitations to workshops and conferences; and (d) Reciprocal visits to research facilities.

The objective of Subtask 2 (Rolling Contact Fatigue Testing) is to compare the currently employed test methods used for evaluating rolling contact fatigue of advanced ceramics to

develop a uniform, internationally agreed-upon testing protocol. Four test configurations are currently in popular use. These include 3-ball-on-rod (mostly used in the U.S.), cylinder-on-cylinder (mostly used in Europe), 4-ball (primarily used for lubrication analysis), and the thrust bearing (mainly used for bearing life testing). Each test configuration has unique attributes. However, no attempt has been made to compare and correlate the data generated by these test configurations. Many issues require particular attention: defining 'failure", understanding the method by which "failure" is detected, distinguishing wear from fatigue, specifying parameters for surface finish, evaluating possible influences from machining damage, and incorporating microslip and sliding into models.

Dr. Wataru Kanematsu (AIST Chubu) has agreed to represent Japan, and Dr. Mathias Woydt (BAM) has agreed to represent Germany. Said Jahanmir (NIST) will represent the U.S. and serve as the Subtask Coordinator. The National Technical Coordinators will perform a preliminary assessment of the rolling contact fatigue testing methods used in their country. They shall seek participation of relevant industrial, academic and government organizations. The assessment shall specify the design and operating conditions of the most popular test machines (e.g., rotational speed, contact load, lubrication condition, failure detection method, etc.), the desired specimen configuration, surface preparation specifications, number of specimens required for acceptable statistical evaluations, statistical data analysis, methods of data reporting, and sample data for each test configuration. Each participating country is encouraged to design and carryout a round robin, if the results of the assessments warrant such a study. The test materials and testing parameters shall be selected jointly with other National Technical Coordinators to allow cross comparisons between participating countries.

Based upon the information gathered by the participants, the Subtask Coordinator, jointly with the National Technical Coordinators, shall decide if a common testing procedure and specimen configuration can be used for a round robin, or if selected common materials should be used in different test configurations for intercomparisons. The Subtask Coordinator, in consultation with the National Technical Coordinators, shall set up a format for reporting the results of the assessment and any round robin results. Each country participating in this effort will issue an interim progress report by March 2003 and a final report by March 2004. The Subtask Coordinator shall prepare a final report integrating all the results by June 2004. The final report shall include recommendations for follow-on activities if necessary.

Pre-Standards Research for Rolling Contact Fatigue

Research during this reporting period extended the results on contact damage in Si_3N_4 during single cycle indentation using spherical WC indenters. Twelve different silicon nitrides (Table 1) were characterized for hardness, toughness and indentation response. The different silicon nitrides fall into three basic types: bearing-grade materials, high-temperature materials, and higher-strength materials. Previously reported and augmented data are summarized in Tables 1-4. Formulae for calculating hardness and toughness from data are given at the end of this section.

The response to contact damage from spherical indenters was characterized for both the appearance of a residual impression as well as the formation of ring cracks around the indent site. Testing employed 6.35 mm and 3.175 mm WC indenters. After indentation at 25 N/s the shape and depth of the residual impression, d_{max}, were characterized by profilometry (Mahr

Perthen Perthometer PRK). Residual impressions were typically up to 1 μm deep and 0.75 mm in diameter with a roughly spherical profile. Most often, there was little detectable uplift (h<0.05 μm) surrounding the indent. The one notable exception was the NBD-100, where the residual impressions inside the ring cracks were flat-bottomed and material outside the ring crack was raised up over the surface by up to 0.3 μm. Note also that the NBD-100 has significantly larger Knoop and Vickers hardness (Table 1). The surface roughness of some of the specimens, as well as their slight (~1 μm over 6 mm) curvature, limited the accuracy of the residual impression depth to +/-0.03 μm. Often it was possible to find residual impressions by profilometry that were not detected using differential interference contrast (DIC or Nomarski) in the optical microscope. The existence of ring cracks surrounding the indent site was verified using optical microscopy, typically using DIC.

Generally the residual impression depth, d_{max}, increased linearly with load, P, above the critical load, P_Y. Figures 1 and 2 show linear regressions of the residual impression depth, d_{max}, above the critical load, P_Y. The linear regressions extrapolate back to significantly different critical loads, P_Y, for formation of the residual impression.

Lawn and coworkers[1] have recently advanced a model for predicting whether quasi-plasticity or brittle fracture will dominate under spherical indenters in ceramics. When quasi-plasticity dominates under the indenter, the critical load for permanent deformation, P_Y, is related to the hardness, H, reduced modulus E', and indenter radius r, by

$$\frac{P_Y}{r^2} = \frac{1.1\pi}{c^3}\left(3\frac{1-\nu^2}{4}\right)^2 H\left(\frac{H}{E'}\right)^2, \tag{1}$$

where c=3, a constraint factor that is the proportionality constant that maps yield strength into hardness ($H = cY$). The normalized critical load, P_Y/r^2, increases linearly with hardness parameter $H(H/E')^2$. As long as the critical loads for quasi-plasticity, P_Y, and for ring crack formation, P_C, are not too different (so that the change in the geometry does not invalidate their calculation), the ratio of critical load for quasi-plasticity to brittle fracture for a material with hardness, H, and toughness, T, is

$$\frac{P_Y}{P_C} = \frac{D}{A}\frac{H}{E'}\left(\frac{H}{T}\right)^2 r, \tag{2}$$

where D=0.79 for ν=0.2, and A is a constant. Lawn et al have assumed A = 8600 from a fit to their data for a number of ceramics (not including silicon nitride). For purposes of comparison of the silicon nitrides here, the absolute value is not important. In this research we are interested in determining if Eq. 2 can be used to rank different grades of silicon nitride for their contact damage resistance. The absolute value of P_Y/P_C (i.e. > or < 1) is less important than understanding if the relation predicts the observed propensity for damage formation.

Figures 3 and 4 show the observed critical load for quasi-plasticity, P_Y, (determined from the linear regressions of Figures 1 and 2) normalized by the indenter radius, r^2 as a function of the hardness parameter (the second term in Eq. 1). The solid line is the predicted slope of the relation in Eq. 1. As Lawn et al also found for silicon nitride, all the data lie above the predicted line. More importantly, taken as a group, there is no correlation between actual critical load, P_Y/r^2, and the hardness parameter $H_{V10}\ (H_{V10}/E')^2$. However, the bearing grades of silicon nitride, denoted by the open circles, generally have greater contact damage resistance (as evaluated by

P_Y/r^2) than do the high-temperature and experimental grades. Note also that the hardness parameter calculated from the measured Vickers hardness and toughness does not differentiate the bearing grades from the other grades. Data for the NBD-100 (the symbol at the largest hardness parameter) should be interpreted with caution, since its flat-bottomed failure mode is so different from the other grades.

Lawn et al. have demonstrated that Eq. 2 can be used to discriminate between brittle fracture and quasi-plasticity between different classes of ceramics. We are interested in seeing if Eq. 2 can be used to make a similar discrimination within the class of silicon nitrides. Table 4 shows that the predicted and actual values of P_Y/P_C for the grades of Table 1 are uncorrelated, indicating that the simple test for hardness and toughness cannot predict the occurrence of quasi-plasticity over brittle fracture for silicon nitride. Some entries in the table are given as minimum or maximum values. These correspond to tests where the either the maximum or minimum value for P_Y or P_C is still undetermined.

Formulae for hardness and toughness used in the plots

Knoop hardness, H_{K1}, was measured from five or six indents using a P = 9.8 N (1 kg) load following ASTM C1326 and calculated from

$$H_{K1} = 0.014229\left(\frac{P}{d^2}\right), \tag{3}$$

where d is the long diameter (in mm) of the indent measured optically. Fracture toughness, K_{1c}, was measured using the indentation crack length method of Anstis et al.[2] using both 98 N and 49 N loads:

$$K_{1c} = 0.016\left(\frac{E}{H}\right)^{1/2}\left(\frac{P}{c^{3/2}}\right), \tag{4}$$

where E = Young's modulus, H = hardness, P = load and $2c$ = the tip-to-tip length of the resulting indentation crack. The indentation diagonal length, d (in mm) was used to calculate the Vickers hardness, H_V, from the load, P, in N:

$$H_V = 0.0018544\frac{P}{d^2} \tag{5}$$

Testing employed the general procedure of ASTM C1327, but the loads were much higher: 49 N and 98 N. The calculation of the fracture toughness (Eq. 3) used this hardness. For purposes of comparison, we have assumed ν=0.2, and E=310 GPa for all twelve silicon nitrides. The manufacturers reported values lie with 10 GPa of this value. For the Co-bonded WC E = 640 GPa. The uncertainties reported in Table 1 represent only the statistical variability of the length measurements, and do not include any systematic errors.

Status of Milestones

1. Propose to the IEA Executive committee the formation of a new subtask under Annex II to study contact damage (December 2001): complete.
2. Compare the nature of failure mechanisms in single-cycle ball-on-flat contact damage to those in rolling contact fatigue for silicon nitride. (March 2002) complete.
3. Compare the nature of failure mechanisms in multi-cycle contact damage to those in rolling contact fatigue for silicon nitride. (July 2002) complete.

4. Explore the feasibility of standardizing the 3-ball-on-rod rolling contact fatigue (RCF) test and assemble a team of users of the 3-ball-on-rod RCF test to conduct an interlaboratory study of RCF of engine ceramics. (September 2002) complete.

Communication/Visits/Travel

None this period

Publications

S Jahanmir, "Model for wear transition in ceramics" Proceedings of the Australian Tribology Conference, Sydney, Australia, 2002 (submitted).

References

[1] Y.-W. Rhee, H.-W. Kim, Y. Deng, B. R. Lawn "Brittle Fracture versus Quasi-Plasticity in Ceramics: A Simple Predictive Index," *J. Am. Ceram. Soc.* 84[3] 561-565 (2001).

[2] G. R. Anstis, P. Chantikul, B. R. Lawn and D. B. Marshall, *J. Am. Ceram. Soc.* **64**[9] 533-538 (1981).

Table 1: Si_3N_4 Properties

Material	Typical use	H_{K1} GPa	$u(H_{K1})$ GPa	H_{V10} GPa	$u(H_{V10})$ GPa	K_{1c} MPa $m^{1/2}$	$u(K_{1c})$ MPa $m^{1/2}$
147-31N	Bearing	14.07	0.15	14.88	0.16	4.32	0.05
N8201	Bearing	13.68	0.15	14.83	0.14	4.56	0.07
NBD-100	Bearing	16.14	0.11	18.61	0.23	3.41	0.08
NBD-200	Bearing	14.48	0.11	15.32	0.16	4.34	0.02
TSN-03NH	Bearing	14.48	0.11	15.45	0.17	4.67	0.07
GN-10	High-T	14.30	0.11	15.51	0.34	4.67	0.28
AS800	High-T	13.36	0.17	14.70	0.31	4.74	0.08
SN88	High-T	14.18	0.11	14.56	0.21	3.80	0.10
NT-164	High-T	14.53	0.16	15.72	0.22	3.94	0.09
GS44	High strength	13.52	0.11	15.12	0.39	4.72	0.08
5Y-2Al-1Mg	experimental	14.68	0.39	14.27	0.09	5.21	0.15
13Yb-.05Al	High-Tl	13.21	0.19	15.20	0.47	4.71	0.13

Table 2: Critical Loads, P_C, for ring crack formation

	3.175 mm WC ball				6.35 mm WC ball			
	Cracking load (N)		P_C	$u(P_C)$ *	Cracking Load		P_C	$u(P_C)$
Material	Yes	No	(N)	(N)	Yes	No	(N)	(N)
147-31N	1044	860	952	92	1550	1451	1500.5	49.5
N8201	860	699	779.5	80.5	2239	1761	2000	239
NBD-100	560	N/D†			1019	N/D		
NBD-200	560	N/D			1019	N/D		
TSN-03NH	860	699	779.5	80.5	1761	1356	1558.5	202.5
GN-10	N/D	1044			N/D	2796		
AS800	1252	1019	1135.5	116.5	N/D	3439		
SN88	777	699	738	39	1550	1356	1453	97
NT-164	860	699	779.5	80.5	2796	2239	2517.5	278.5
GS44	1252	1044	1148	104	3439	2796	3117.5	321.5
13Yb-.05Al	N/D	860			N/D	2796		
5Y-2Al-1Mg	N/D	1044			N/D	N/D		

(*) uncertainty in critical load (max-min)/2 † N/D = not determined—critical load is above or below max or min load
? replicate tests give different critical loads in the range XX < P < XX

Table 3: Critical load, P_Y, for residual impression

	3.175 mm WC Ball				6.35 mm WC Ball			
Material	Yes	No	P_Y	$u(P_Y)$	Yes	No	P_Y	$u(P_Y)$
147-31N	440	339	389.5	50.5	1761	1653	1707	54
N8201	699	560	629.5	69.5	2796	2239	2517.5	278.5
NBD-100	699	560	629.5	69.5	1356	1019	1187.5	168.5
NBD-200	699	560	629.5	69.5	2239	1761	2000	239
TSN-03NH	860	699	779.5	80.5	N/D	2796		
GN-10	699	N/D			1761	N/D		
AS800	255	N/D			1019	743	881	138
SN88	560	440	1761	1550	1761	1550	1656	106
NT-164	560	440	500	60	1356	1019	1187.5	168.5
GS44	440	339	389.5	50.5	1019	N/D		
13Yb-.05Al	560	N/D			1356	N/D		
5Y-2Al-1Mg	560	N/D			N/D	N/D		

Table 4. Theoretical and actual critical load ratios

		d = 3.175 mm		d=6.35 mm	
	Material	P_Y/P_C theoretical	P_Y/P_C actual	P_Y/P_C theoretical	P_Y/P_C actual
Bearing Grade	147-31N	0.11	0.41	0.22	1.14
	N8201	0.09	0.81	0.19	1.26
	NBD-100	0.27	>1.13	0.54	>1
	NBD-200	0.12	>1.13	0.24	>2
	TSN-03NH	0.10	1.0	0.21	1.79
Other grades	GN-10	0.10	>0.33	0.20	<0.63
	AS800	0.08	0.11	0.16	<0.25
	SN88	0.15	0.68	0.30	1.14
	NT-164	0.15	0.64	0.30	0.47
	GS-44	0.08	0.34	0.17	0.16
	13Yb-0.05Al	0.08	<0.53	0.16	<0.48

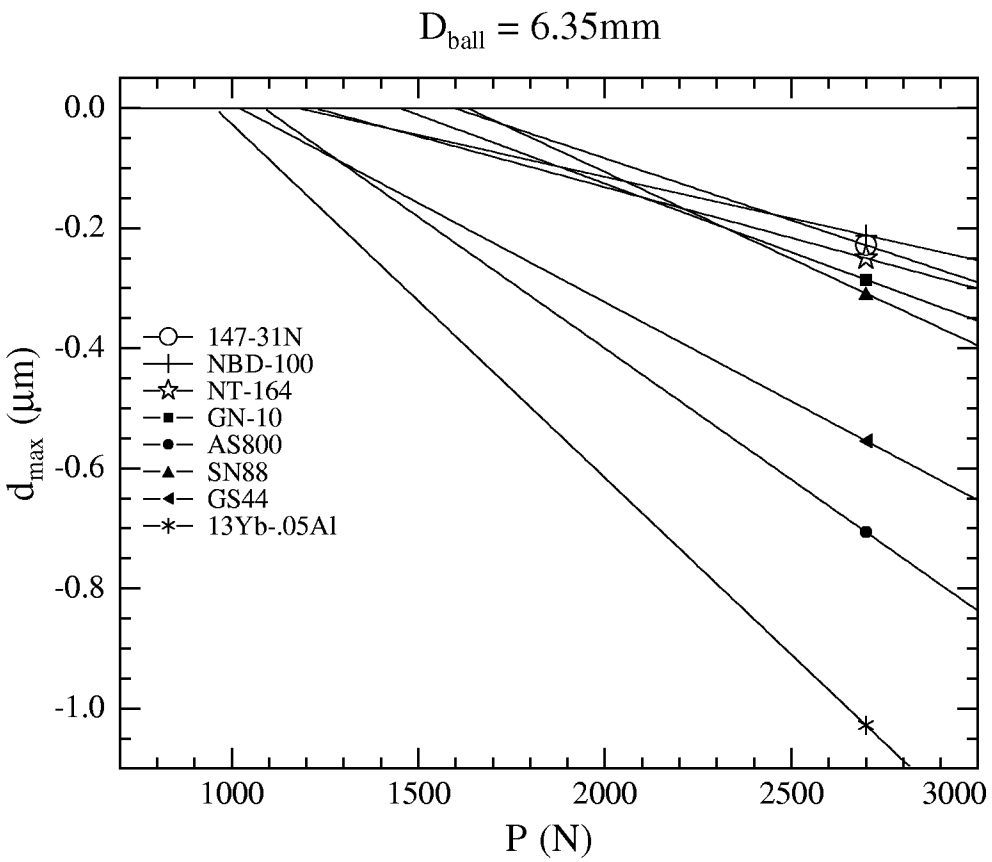

Figure 1 Residual impression depth for 6.35 mm WC indenter as a function of load showing extrapolation to critical load, P_Y.

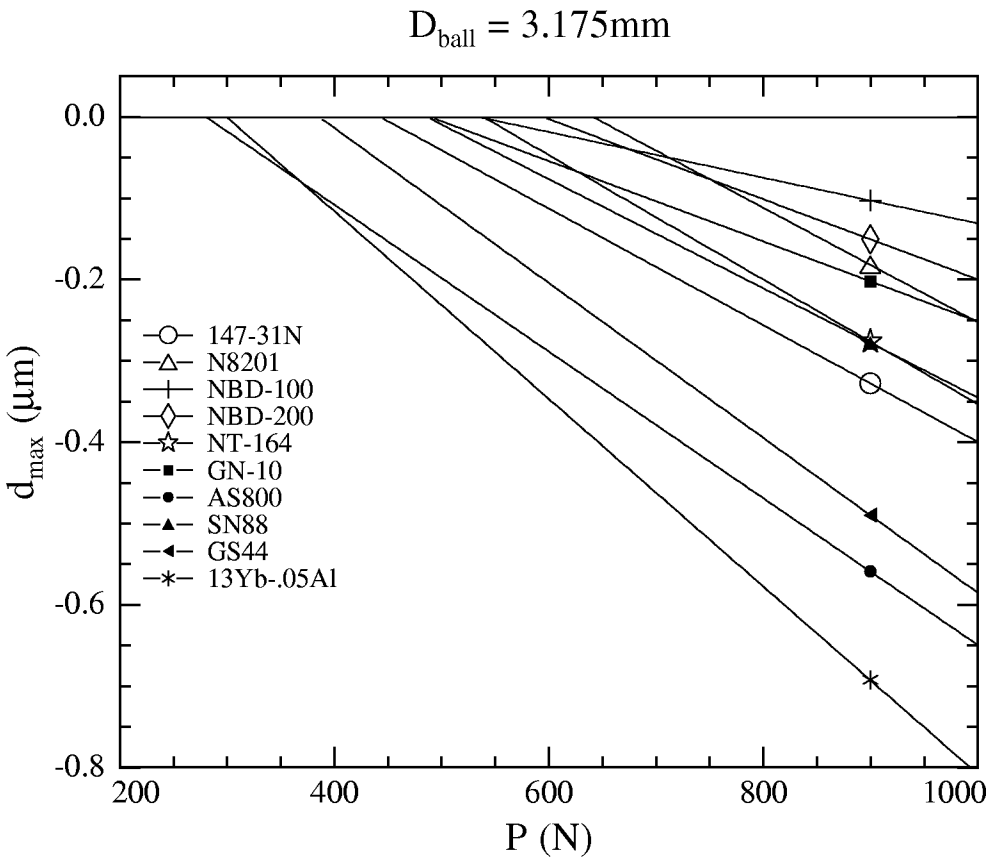

Figure 2 Residual impression depth for 3.175 mm WC indenter as a function of load, showing extrapolation to critical load, P_Y.

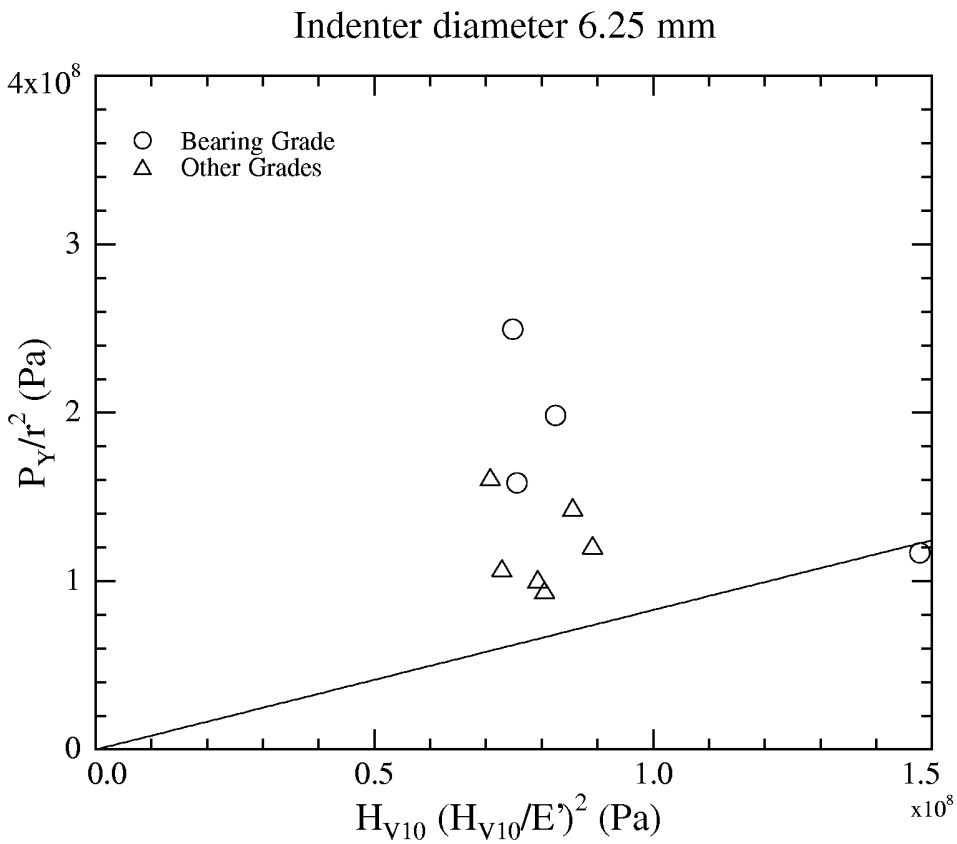

Figure 3 Normalized critical load for quasi-plasticity as a function of predicted load via the hardness parameter for 6.25 mm WC ball indenter

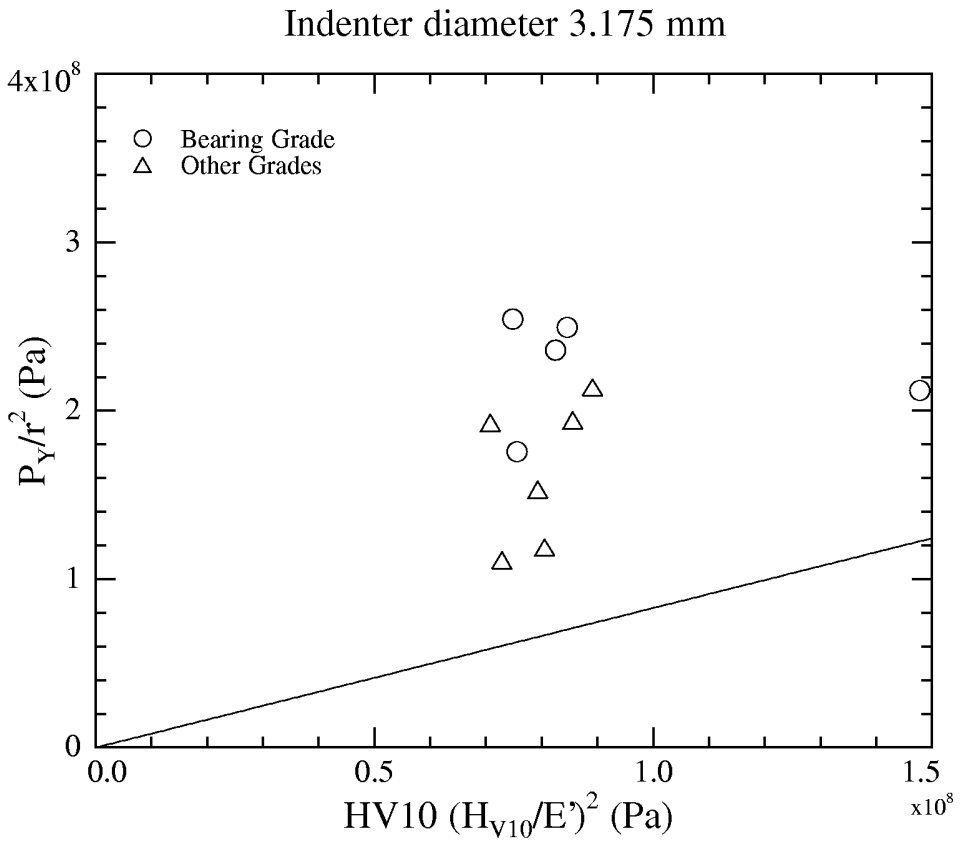

Figure 4 Normalized critical load for quasi-plasticity as a function of predicted load via the hardness parameter for 3.175 mm WC ball indenter.

Mechanical Property Test Development

George Quinn

NIST

Objective/Scope

This task is to develop mechanical test method standards in support of the Propulsion Systems Materials Program. Test method development should meet the needs of the DOE engine community but should also consider the general USA structural ceramics community as well as foreign laboratories and companies. Draft recommendations for practices or procedures shall be developed based upon the needs identified above and circulated within the DOE engine community for review and modification. Round robins will be conducted as necessary. Procedures will be standardized by ASTM and/or ISO.

Technical Highlights.

1. General

The manuscript on machining damage characterization that was completed in May has been held up since our attention was diverted to another pressing topic. In this quarterly period we finished the preparation of **Standard Reference Material 2831, Vickers Hardness of Ceramics and Hardmetals.** SRM 2831 is a tungsten carbide (12% cobalt) disk that has been polished and indented with master Vickers indentations at NIST. Users may measure the size (35 μm) of the Vickers indentations and make their own indentations in order to verify the correct operation of their hardness testing machines. The indentation load is 9.8N (1 kgf). This SRM will support the ASTM standards C 1327 for Hardness of Ceramics and E 384 for Microhardness of Materials, as well as the new (2000) ISO standard 14705 and the new European CEN standard EN 843-4.

2. Fracture Toughness

a. ASTM C 1421 This topic is completed. A paper on the application of C 1421 to Ceradyne's production grade sintered reaction bonded silicon nitride grade Ceraloy 147 was prepared and sent to the American Ceramic Society. Consistent results were obtained by when the 3 test methods specified in C 1421 were used.

b. ISO DIS 18756, Fracture Toughness by the SCF method

This document is nearing completion. It is in a 5-month ballot which will close out on October 16, 2002.

3. Flexural Strength of Advanced Ceramics – Rectangular Specimens

a. ASTM C 1161 *Revisions*

The proof copy of C 1161, which was extensively revised in early 2002, was reviewed in the prior quarterly period. A handful of promotional notices and short articles were published this quarter and a few dozen inquiries about the changes to C 1161 have been received and answered.

b. ASTM C 1211*, Elevated Temperature Flexural Strength Revisions*

This standard, which is the elevated temperature version of C1161, was due for an overhaul. The ballot for twenty separate revisions closed out on September 10th. As of this writing, Mr. Quinn has received no feedback. The changes are similar to those made to C 1161, the room temperature standard.

c. ISO 17565, *Elevated Temperature Flexural Strength*

This document has or will shortly enter its 5-month enquiry stage ballot phase as a FDIS, "Final Draft International Standard."

4. ASTM Standard C 1322, Fractographic Analysis of Advanced Ceramics

The first round of major revisions to C 1322 was balloted by ASTM in late January- mid March 2002. The ballot responses were reviewed at the ASTM Committee meeting in St. Louis at the end of April 2002. A second set of revisions was balloted in July – September 2002. The second set included eight groups of definitions, which were tripped out by a negative ballot in the first ballot round.

5. New NIST Guide to Practice for Fractographic Analysis

Although the ASTM Standard Practice for Fractographic Characterization of Fracture Origins has been on the books for six years now, NIST management felt that there was still a need for a separate user-friendly "Guide to Best Practice" for fractographic analysis. Work will commence on this topic in FY 2003.

6. Flexural Strength Testing of Cylindrical Ceramic Specimens

The NIST Ceramic Machining Consortium program was completed in December 2001. Follow on analysis and intensive fractographic examination of hundreds of specimens continued until the end of May 2002. We have reached the point that we can detect transverse machining damage fairly easily in many materials. This was quite an achievement, since at the beginning of the study; the machining cracks seemed very elusive! ASTM standard C 1322 was revised in early 2002 to include numerous illustrations and general schematics of machining damage cracks. In the last quarterly report, we included some illustrations of the machining damage and a discussion of some key findings.

A first draft major new report on detection and characterization of the machining damage has been written, but progress on refining the draft has been held up while we completed work on the Vickers hardness reference disks described below.

7. New Standard Reference Materials for Vickers Hardness

During this quarterly report, we finished the preparation of the long overdue SRM 2831, Vickers Hardness of Ceramics and Hardmetals. One hundred and eight tungsten carbide disks were prepared, indented, and measured. Ninety-six were accepted for distribution by the NIST Reference Materials Office. The disks are finished and ready, but the Statistical Engineering Division must review the data collected and the uncertainty estimates so that a proper certificate to accompany the disks may be prepared. This should not be too difficult, since we did this once before with the SRM 2830 Knoop Hardness Reference disks material which have been available since late 1996. SRM 2831 should be available in a matter of 2-3 months.

Table 1 shows the three Standard Reference Materials, which support several of the standards developed in this program. Regrettably, the market for these SRM's has been soft. Department of Energy contractors and researchers are encouraged to inquire further about these SRM's which are valuable tools to verify proper instrument operation. The SRM's are also valuable aiding product compliance with specifications.

Table 1 Reference Materials

SRM	Specifics	Availability	Images
#2100 Fracture Toughness of Ceramics K_{Ic}	(5) silicon nitride bend specimens with certified fracture toughness values: 4.57 MPa√m. Any method may be used.	Immediate $355	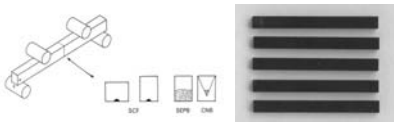
#2830 Knoop Hardness of Ceramics HK2	(1) hot-isopressed (NBD-200) silicon nitride disks with 5 NIST 19.6 N (2 kgf) indentations HK ~ 14.0 GPa; 1,400 kgf/mm^2	Immediate $581	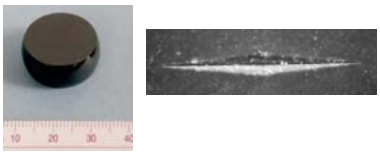
#2831 Vickers Hardness of Ceramics and Hardmetals HV1	(1) hot-isopressed tungsten carbide disk (12% cobalt) with (5) NIST 9.8 N (1 kgf) indentations. HV ~ 15.0 GPa; 1500 kgf/mm^2	Estimated Dec. 2002 Estimated $450	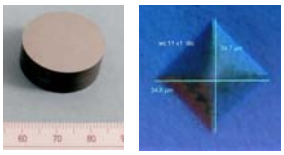

For more information about these SRM's, or any of the NIST power size standards, contact:

http://ts.nist.gov/ts/htdocs/230/232/232.htm

Figure 1 shows the new SRM 2831 and a close up of the indentation pattern and one sample measurement set. The SRM is a hot-isostatically pressed tungsten carbide containing nominally 12% cobalt binder phase, fabricated in the form of disks that have been ground and polished to provide a very flat, parallel, high quality surface for Vickers indentations. The average grain size of the carbide grains is approximately 0.5 µm. The disks have a nominal diameter of 25 mm and a thickness between 9.4 mm and 9.6 mm. Five NIST Vickers indentations are located in the disk center on the polished surface and are arranged in a pattern as shown in Figure 1. The certified individual diagonal lengths and the average hardness for the 5 NIST indentations will be listed on an accompanying certificate, but is of the order of 35.0 µm.

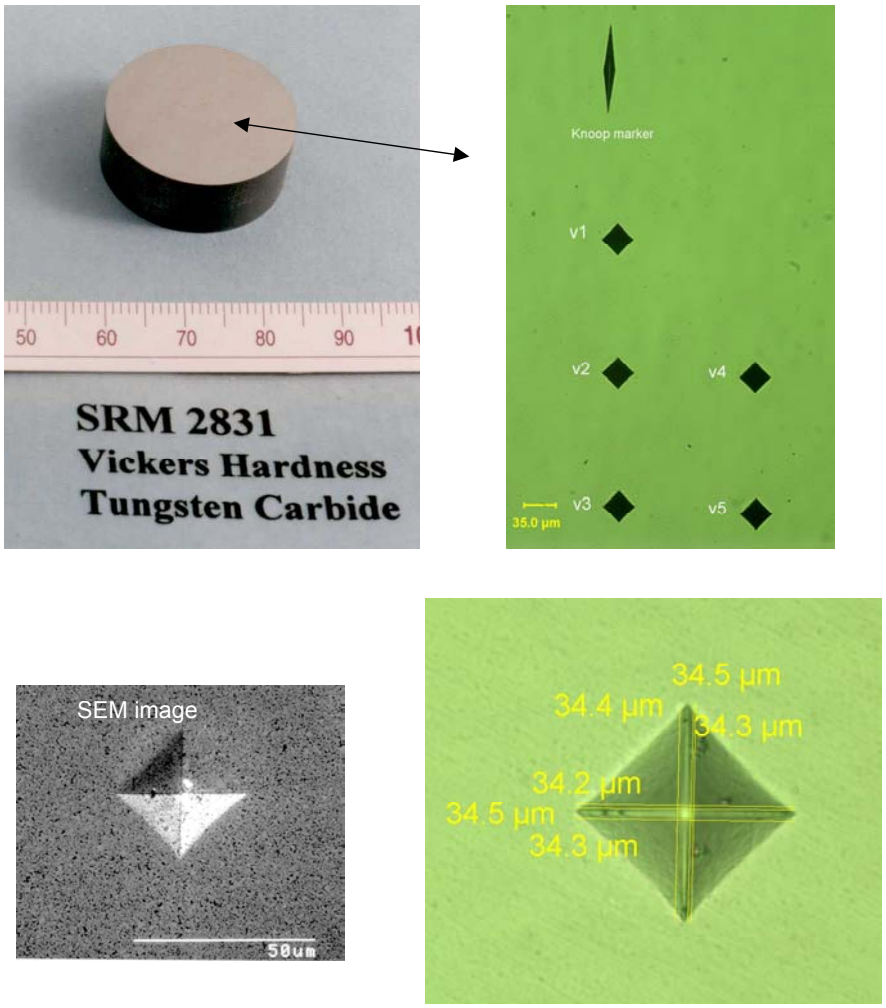

Figure 1 Standard Reference Material 2831 Vickers Hardness of Ceramics and Hardmetals

The five NIST indentations were made by a dedicated Tukon 300 table model hardness testing machine. The Vickers diamond had average face angles of 135° 57' 13" and a tip offset of 0.19 μm. A single Knoop indentation (not measured) serves as a marker. The indentations were made in accordance with ASTM E 384-1999, Test Method for Microhardness of Materials, ASTM C 1327-1996a, Test Method for Vickers Hardness of Advanced Ceramics, CEN prEN 843-4 (2001), and ISO 14705-2000 Fine Ceramics (Advanced Ceramics, Advanced Technical Ceramics) – Test Method for Hardness of Monolithic Ceramics at Room Temperature.

These indents were then examined and digitally photographed with a high-resolution digital camera (3 color CCD, 11.8 mm x 8.9 mm chip, 1600 x 1200 pixels) on a Leica DMRM laboratory research microscope using a 40X objective lens with a numerical aperture of 0.6. Bright field illumination with a green filter was used with properly adjusted aperture and field diaphragms. A 1.6X slider and a 3.2X camera magnifier magnified the image further. The image was projected onto a high-resolution (1600 x 1280 pixel) SVGA flat monitor with 0.22 mm pitch. The indentations appeared 68 mm large (~2000 apparent magnification) on the monitor as shot, but were digitally enlarged to 200 mm (~5,700 magnification) for close inspection of the diagonals and the tips.

The horizontal (d_1) and vertical (d_2) diagonal lengths were measured on the computer digital image to a resolution of 0.1μm. An optical stage micrometer (WILD model 31045) was used to calibrate and frequently recheck the length calibration measurements. The stage micrometer was calibrated by the NIST calibration services to an accuracy uncertainty of better than 0.01%.

8. Other

The new paper on the surprising finding that conversion (or scaling) factors for converting ASTM flexural strengths to JIS strengths is independent of whether flaws are surface or volume distributed was approved by the Journal of the American ceramic Society. Conversion of strength numbers from JIS to ASTM or to CEN or ISO standards does not depend upon what kinds of flaws are present. Fractographic analysis is unnecessary! A simple factor may be used to convert strengths from testing configuration to another. The manuscript was revised in response to reviewers' comments.

The companion paper on the Weibull effective volumes and surfaces of cylindrical rods required major revisions and has been resubmitted to the Journal.

A visiting German Scientist, Mr. Jens Eichler from Technical University Darmstadt, brought some yttria stabilized TZP zirconia disks (~50) and bend bars (~12) to NIST in early September 2002 for fractographic

evaluation. We were able to find the fracture origins in these specimens and went a step further and measured the fracture mirror sizes. There were several batches of Y-TZP with average grain sizes from 100 nm to 500 nm. A short paper on the fracture mirror interpretations and the mirror constants is in preparation. When we revised the ASTM standard C 1322 for fractographic analyses, we came to the realization that more mirror constants are needed for contemporary ceramics, since many of the published values were for older materials. We took this opportunity to obtain a fresh set of results for the mirror constant for Y-TZP.

Status of Milestones

412146	Ballot major revisions to ASTM C 1161 flexural strength	September 2001, **Completed, October 2002✓**
412147	Prepare ballot revisions for ASTM C 1322, Fractographic Analysis	April 2002, **Completed, January 2002✓**
412148	Prepare follow on specimen machining revisions to ASTM C 1161 flexural strength if needed	April 2002 **Completed, April 2002✓**
412149	Prepare ballot-ready first ASTM draft of cylindrical rod flexure strength test	April 2002 **Delayed**
412150	Prepare paper on effect of machining on strength of SRBSN rods.	May 2002 **In progress, First draft done**
412151	Prepare review paper on flexural testing of cylindrical rods.	October 2002 **Delayed by completion of SRM 2831, HV**

Communications/Visits/Travel

Additional announcements and letters and specimen blueprints about the ASTM C 1161 revisions were sent out to about 20 interested parties.

A set of bend bar fragments from the fracture toughness reference material, SRM 2100, were sent to Jon Salem at NASA-Glenn. Jon will see if miniature chevron notch specimens (3 x 4 x 20+ mm specimens tested on a 20 mm span) produce results comparable with the full size chevron notch specimens. If so, then the ASTM and ISO standards may be revised to include this convenient miniature size. The standards already include miniature SCF and SEPB specimens.

Publications and presentations

1. G. D. Quinn, J. J. Swab, and M. J. Motyka, "Fracture Toughness of a Toughened Silicon Nitride by ASTM C 1421," subm to J. Am. Ceram. Soc., May 2002.
2. G. D. Quinn, "Weibull Strength Scaling for Standardized Rectangular Flexure Specimens," accepted J. Am. Ceram. Soc., July 2002.
3. G. D. Quinn, "Weibull Effective Volumes and Surfaces for Cylindrical Rods Loaded in Flexure," subm. to J. Am. Ceram. Soc., May 2002.